

1-29-2009

Design fabrication and calibration of MEMS actuators for in-situ materials testing

Khawar Abbas

Follow this and additional works at: https://digitalrepository.unm.edu/me_etds

Recommended Citation

Abbas, Khawar. "Design fabrication and calibration of MEMS actuators for in-situ materials testing." (2009).
https://digitalrepository.unm.edu/me_etds/34

This Thesis is brought to you for free and open access by the Engineering ETDs at UNM Digital Repository. It has been accepted for inclusion in Mechanical Engineering ETDs by an authorized administrator of UNM Digital Repository. For more information, please contact disc@unm.edu.

Khawar Abbas

Candidate

Mechanical Engineering Department

Department

This thesis is approved, and it is acceptable in quality and form for publication on microfilm:

Approved by the Thesis Committee:

Dr. Zayd C. Leseman

Committee Chair

Dr. Yu-Lin Shen

Committee Member

Dr. Marwan Al-Haik

Committee Member

Accepted:

Dean, Graduate School

Date

**DESIGN FABRICATION AND CALIBRATION OF
MEMS ACTUATORS FOR IN-SITU MATERIALS TESTING**

BY

KHAWAR ABBAS

B.E. Mechanical, National Univ. of Sc. & Tech., Pakistan, 2000

THESIS

Submitted in Partial Fulfillment of the
Requirements for the Degree of

**Master of Science
Mechanical Engineering**

The University of New Mexico
Albuquerque, New Mexico

December, 2008

ACKNOWLEDGEMENTS

This thesis would not have been possible without the countless contributions of so many people that I came across during my MS at the University of New Mexico. I would like to thank them and let them know that I appreciate their help from the bottom of my heart.

I am thankful to Allah Subhana wa Ta'ala (God the Almighty and the Greatest) for everything that I am blessed with in life, for giving me this opportunity to learn and answering my prayers in times of frustration and desperation when nothing is going as planned.

I am grateful to my research advisor Dr. Zayd C. Leseman. He introduced me to this exciting field of MEMS and Micro-mechanics, provided technical guidance, necessary financial support and overlooked my mistakes. He has been a constant source of inspiration for me and this work would not have been possible without his support, encouragement and suggestions.

I am thankful for the support provided by UNM Manufacturing Training and Technology Center (MTTC). The cleanroom staff at MTTC was extremely helpful and insightful. Harold Madsen helped me in developing the fabrication process and at the same time keeping myself safe from chemicals in the cleanroom. Sam Kriser was very instrumental in keeping the equipment that I required in perfect working order. Without their support this work would have been impossible.

Thanks to Mark Atwater for helping me out in obtaining SEM images and measurements. I am thankful to Maheshwar R. Kashamola for letting me use his

optical components for my experimental setup. I want to express my gratitude to Dr. Lumia and his graduate student Brian Schmitt for allowing me to use their CCD camera. Brian was also very helpful to me in maintaining my sanity in the Lab. Our brain storming sessions were very insightful and the short trips to Cold Stone and Dunkin' Donuts were very helpful in boosting my morale after a failed experiment.

I would like to thank my fellow students Drew Goettler and Edidson Lima for their help, support, friendship and comradeship. They made me feel at home and welcomed at the time when everything around me was totally new in a foreign land. I wish both of them best of luck in their future endeavors.

Last, and most importantly my parents deserve much credit for my success. They raised me in an atmosphere of appreciation of science, for learning and for striving to understand the world around me. I am especially grateful to my mother for her constant encouragement, unconditional support and genuine love.

I have inevitably missed some people but I would like all of them to know that their help is no less appreciated - "Thanks a lot."

**DESIGN FABRICATION AND CALIBRATION OF
MEMS ACTUATORS FOR IN-SITU MATERIALS TESTING**

BY

KHAWAR ABBAS

ABSTRACT OF THESIS

Submitted in Partial Fulfillment of the
Requirements for the Degree of

**Master of Science
Mechanical Engineering**

The University of New Mexico
Albuquerque, New Mexico

December, 2008

DESIGN FABRICATION AND CALIBRATION OF MEMS ACTUATORS FOR IN-SITU MATERIALS TESTING

BY

KHAWAR ABBAS

B.E. Mechanical, National Univ. of Sc. & Tech., Pakistan, 2000

M.S., Mechanical Engineering, University of New Mexico, 2008

ABSTRACT

Many MEMS devices utilize thin metallic films as mechanical structures. The elastic and plastic properties of these thin films (thickness < 1 μ m) are significantly different from those of the bulk material. At these scales the volume fraction of material defects such as: grain boundaries, dislocations and interstitials become quite significant and become a chief contributor the physical and mechanical material properties of the thin films. Aluminum (Al), Copper (Cu), Nickel (Ni) and Gold (Au) are popular thin film materials used in MEMS/NEMS. Various studies have been conducted in recent years to study the mechanical properties of freestanding thin films in situ in TEM to study their failure mechanisms. Some of these studies utilize MEMS devices as actuators. These actuators are often co-fabricated with the specimen being tested therefore limiting the type of specimen that could be tested. Also these MEMS actuators are almost never traceably calibrated and their response is calculated. This thesis describes the design and fabrication process of a MEMS actuator for materials testing in-situ in TEM. The actuator is fabricated independent of the specimen. A setup was designed to calibrate these devices with a method that can be traced back to NIST standards. It has been shown that the calibrated

response of these MEMS actuators is different from its calculated response and the use of un-calibrated devices for materials testing can lead to misleading results.

Table of Contents

Chapter 1.....	1
1. INTRODUCTION.....	1
1.1. Background and Motivation	1
1.2. Scope	5
1.3. Overview / Organization.....	5
Chapter 2.....	6
2. THEORY OF MEMS COMB DRIVE ACTUATORS	6
2.1. Flexure Springs.....	6
2.1.1. Fixed-fixed flexure	7
2.1.2. Crab-Leg Flexure	11
2.1.3. Folded Flexure.....	13
2.1.4. Serpentine Flexure.....	16
2.2. Electrostatic Force	18
2.2.1. Side (Axial) Instability	20
2.2.2. Front (Lateral) Instability.....	21
Chapter 3.....	23
3. DESIGN AND FABRICATION.....	23
3.1. Design specifications	23
3.2. Fabrication.....	28
3.2.1. Mask Design and Development	28
3.2.2. Actuator Fabrication.....	28
Chapter 4.....	33
4. TESTING AND CALIBRATION.....	33
4.1. Side Instability Voltage	33
4.1.1. Setup.....	33
4.1.2. Procedure	35
4.2. Calibration	35
4.2.1. Setup.....	38
4.2.2. Procedure	41
Chapter 5.....	45
5. EXPERIMENTAL RESULTS AND DISCUSSION.....	45

5.1. Compressive Residual Forces	45
5.2. Side Instability Voltage	46
5.3. Calibration	47
5.3.1. Fixed-fixed flexure	49
5.3.2. Folded flexure	53
Chapter 6.....	56
6. CONCLUSION.....	56
6.1. Future Work.....	57
Bibliography	58
Appendix 'A'	62
A. FABRICATION PROCEDURE	62
Appendix 'B'	65
B. MATLAB CODES	65
Appendix 'C'	82
C. TEM HOLDER DESIGN DRAWINGS.....	82

List of Figures

FIGURE 1: (A) FIXED-FIXED FLEXURE DESIGN. (B) FREE BODY DIAGRAM OF A FIXED-FIXED BEAM.....	8
FIGURE 2: DEFLECTION OF FIXED-FIXED BEAM WITH DIMENSION (H X B X 2L)	10
FIGURE 3: CRAB-LEG FLEXURE DESIGN	11
FIGURE 4: DEFLECTION OF CRAB-LEG FLEXURE (IN Y- DIRECTION) WITH DIMENSIONS $L_A = 500\mu\text{M}$ $L_B = 50\mu\text{M}$ $W_A = W_B = 2\mu\text{M}$ AND $T=20\mu\text{M}$	13
FIGURE 5: FOLDED FLEXURE DESIGN	14
FIGURE 6: DEFLECTION OF FOLDED FLEXURE (IN Y-DIRECTION) WITH DIMENSIONS $L_T = 500\mu\text{M}$; $L_B 50\mu\text{M}$ $W_T = W_B = 2\mu\text{M}$ AND $T=20\mu\text{M}$	15
FIGURE 7: DESIGN OF SERPENTINE FLEXURE	16
FIGURE 8: DEFLECTION OF SERPENTINE FLEXURE (IN Y-DIRECTION) WITH DIMENSIONS $A = 20\mu\text{M}$, $B = 20\mu\text{M}$, $W = 2\mu\text{M}$, $N = 20$ AND $T = 20\mu\text{M}$	18
FIGURE 9: SCHEMATIC DETAILS OF COMB FINGERS.....	19
FIGURE 10: SCHEMATIC DESIGN OF A COMB DRIVE ACTUATOR WITH FIXED-FIXED FLEXURE .	26
FIGURE 11: SCHEMATIC OF A CUSTOM SPECIMEN HOLDER FOR JEOL 2010 AND THE PLACEMENT OF THE MEMS DEVICE	27
FIGURE 12: CUSTOM MANUFACTURED TEM HOLDER	27
FIGURE 13: A SCHEMATIC SHOWING THE FABRICATION PROCESS OF THE MEMS ACTUATOR	30
FIGURE 14: OPTICAL MICROGRAPH OF THE ACTUATOR WITH FIXED-FIXED FLEXURE, $L=800$, $N=600$	31

FIGURE 15: OPTICAL MICROGRAPH OF THE ACTUATOR WITH SERPENTINE FLEXURE AND N=600.....	31
FIGURE 16: OPTICAL MICROGRAPH OF THE ACTUATOR WITH FOLDED FLEXURE AND N=200032	
FIGURE 17: EXPERIMENTAL SETUP USED TO DETERMINE THE SIDE INSTABILITY	34
FIGURE 18: PROBE TIPS IN CONTACT WITH BONDING PADS OF A MEMS ACTUATOR	34
FIGURE 19: MEMS ACTUATOR MOUNTED ON THE GLASS SLIDE	38
FIGURE 20: GLASS SLIDE MOUNTED ON THE GONIOMETER AND INDEPENDENT LINEAR STAGE FOR MOVEMENT IN Z-DIRECTION	39
FIGURE 21: MICROSCOPE MOUNTED ON SEPARATE LINEAR STAGES FOR INDEPENDENT X-Y-Z MOVEMENT	39
FIGURE 22: THE COMPLETE CALIBRATION SETUP.....	40
FIGURE 23: OPTICAL MICROGRAPH OF 790 μM SAPPHIRE SPHERE ATTACHED TO THE ACTUATOR.....	42
FIGURE 24: ACTUATOR TIP DIPPED IN PHOTORESIST DROPLET	44
FIGURE 25: OPTICAL MICROGRAPH OF THE STRAIN GUAGE AT THE CENTRE OF THE WAFER ..	46
FIGURE 26: CALIBRATION CURVE FOR THE FIXED-FIXED FLEXURE	50
FIGURE 27: RANGE OF UNCERTAINTY IN ACTUATOR RESPONSE WITH ELASTIC MODULUS 150 – 170 GPa.....	52
FIGURE 28: COMPARISON BETWEEN THE CALIBRATED RESPONSE AND THE UNCERTAINTY DUE TO DIMENSIONAL VARIATION OF DEVICE WITH FIXED-FIXED FLEXURE	52
FIGURE 29: CALIBRATION CURVE FOR THE FOLDED FLEXURE	53

FIGURE 30: RANGE OF UNCERTAINTY IN ACTUATOR RESPONSE WITH ELASTIC MODULUS 150 –
170 GPa.....54

FIGURE 31: COMPARISON BETWEEN THE CALIBRATED RESPONSE AND THE UNCERTAINTY DUE
TO DIMENSIONAL VARIATION OF DEVICE WITH FOLDED FLEXURE.....55

Chapter 1

INTRODUCTION

1.1. Background and Motivation

Advancements in the semiconductor fabrication technology particularly the advancement in bulk and surface micromachining techniques of silicon (Si) during the 1980's and early 1990's opened doors to a new era of miniaturized electro-mechanical structures and devices that are now known as "MEMS (Micro Electro-Mechanical Systems)" [1-5]. These devices offered new capabilities, improved performance and lower cost due to batch production over traditional transducers and sensors. Perhaps the greatest advantage that MEMS had to offer was their ability to be fabricated compatibly with an integrated circuit (IC) thereby reducing the overall size and power requirements of a complete system to that of a mere IC chip. Since then, this field of science has transformed into an industry of its own which perhaps one day will be as great as its parent semiconductor industry. There are now numerous MEMS devices that are commercially available and are being used in our daily lives. They are being used in many physical, chemical and biological applications. Some of the novel applications of the MEMS devices are provided by Madou [6].

Very often these MEMS devices are micro-actuators and can be classified in one of the following classes: (i) Electrostatic, or (ii) Thermal actuators. Electrostatic actuators are further classified into linear and rotary actuators. Electrostatic

micro-actuators have broad range of applications they are used as micro-loading devices [7,8], micro-mirror and x-y stage manipulators [9,10], strain sensors [11], resonators [12,13], RF switches [14], pressure sensors and accelerometers [15]. These actuators have also been used to deform diaphragms and membranes in micro-pumps and micro-valves [16-18] and have numerous other applications. Due to their widespread use these electrostatic actuators have been subjected to extensive research over past many years and studies ranging from the design and modeling [19-25] to fabrication issues [26,27] and performance enhancement [28-30] are available. However, not much attention has been paid to characterize the static and dynamic properties of these devices or any other MEMS devices through methods that can be traced back to the National Institute of Standards and Technology (NIST). Typically, the theoretical behavior of these devices is calculated and any deviation from the theoretical response is compensated by designing enough margin in their applications.

On the other hand many of these MEMS devices also utilize metallic thin films as mechanical structures. The elastic and plastic properties of these thin films are significantly different from those of the bulk material [31-33]. At these scales the volume fraction of material defects such as: grain boundaries, dislocations and interstitials become quite significant and become a chief contributor the physical and mechanical material properties of the thin films. Aluminum (Al), Copper (Cu), Nickel (Ni) and Gold (Au) are popular thin film materials used in MEMS/NEMS. Various studies have been conducted in recent years to study the mechanical properties of freestanding thin films. Vinci et al [33] developed and

described several specialized techniques to determine the mechanical properties and stress strain states of both free standing and films bonded to substrate. He described nano-indentation as a popular and effective way of determining the elastic and plastic properties as well as hardness of free standing thin films. Landman et al [34] provides detailed theoretical and experimental research of the atomistic and molecular mechanism of adhesion, contact formation, nanoindentation, and fracture that occurs when a Ni diamond shaped nanoindenter interacts with the Au surface. Kalkman et al [32] made measurements of Young's modulus on free standing thin films and observed the relaxation of thin films at room temperature with frequency dependence. They attribute this anelastic behavior to the grain boundary sliding. Haque et al [35] studied the relaxation of freestanding nano-crystalline Au films at room temperature and used an analytical model based on a spring and a dashpot to predict an instantaneous Young's modulus. They also demonstrate the effect of size in nanoscale solids by comparing the relaxation time at room temperature with that of bulk solids. Also very few studies have been conducted so far that explain the failure mechanism of free standing thin films due to fatigue. Hadboletz et al [36] studied the crack growth in free standing Cu foils of different thicknesses when subjected to high cycle bending fatigue. Different studies indicate the fatigue behavior of thin films is dependent upon their thickness.

From the overview presented above it appears that the best method to study the failure of thin films both in tension and fatigue is to study the failure in-situ in a transmission electron microscope (TEM). The small size of the MEMS comb

drive actuators render them perfect for testing thin films in-situ in TEM. Also as oppose to the piezo-electric actuators they do not creep over time. Already some studies have started to appear [37,38]. Zhu et al [37] used a unique parallel plate actuator to study a poly silicon specimen and a carbon nano-wire. Poly silicon sample was co-fabricated with the actuator while the nano-wire was “welded” on the device using the focused ion beam (FIB) probe. Haque et al [38] also co-fabricated thinner Al samples along with the actuator and tested the thicker Au samples using a piezoelectric actuator. The problem with co-fabricating sample with the actuator is that the processing of the sample is limited by the processing of the actuator. Also it renders the actuator useless once the sample has been tested. It also makes it impossible to calibrate the individual actuator prior to the test and therefore there is no way to determine the variation in behavior of the actuator from its theoretical behavior. Piezoelectric actuators creep over time and hence it makes it very difficult to estimate the actual displacements. In this author’s opinion welding the sample to the actuator as done by Zhu et al [37] has potential to alter the material properties of the samples especially near the welds by heating. This can be very problematic in cases where the material to be tested is metallic. Hence there is a need to design a method to test the thin films in-situ in TEM such that the actuator and specimen processing are independent of each other and the measurement and results can be traced to a common standard so that the results from different research groups can be compared.

1.2. Scope

The scope of this thesis is to design and develop a MEMS actuator capable of testing thin film samples in-situ in TEM, such that the processing of the actuator and the sample are independent of each other. Also a method is devised to calibrate these devices that can be traced back to NIST standards [39].

1.3. Overview / Organization

This thesis is divided into six chapters. The second chapter presents the theory of the electrostatic MEMS comb drive actuators. It gives the basic principles behind their operation; some of the common design rules and constraints; as well as the shapes of the most commonly used spring elements used in the MEMS comb-drive actuators. Chapter three provides a detailed explanation the design fabrication process used to develop and later fabricate these devices in the lab. Chapter four describes the setup and procedure used to test and calibrate the fabricated devices. Chapter five of this thesis and presents the experimental results, their deviation from the calculated behavior and a discussion on the reasons for this deviation. Chapter six is the last chapter of this thesis and presents the conclusion and future work.

Chapter 2

THEORY OF MEMS COMB DRIVE ACTUATORS

Comb drive actuators consist of two sets of inter-digitated fingered structures; one of which is fixed while other is suspended and connected to compliant springs. The voltage difference across the comb fingers causes the movement of compliant part of the structure due to the electrostatic / electrostatics force. There are two components that govern the motion of a comb drive: stiffness of the flexure spring and the electrostatic force between the fingers. This chapter presents an overview of the theory of comb drive actuators, equations of stiffness for the most common type of flexures springs, electrostatic force as well as the common problems and design rules.

2.1. Flexure Springs

In most cases it is desirable for a MEMS actuator to move in a single plane. Therefore the structure is typically designed to be compliant in one dimension which is typically in the plane of the wafer, and relatively stiff orthogonal to the plane of the wafer. This is normally expressed as the ratio of stiffness in non-compliant direction to the stiffness in compliant direction (k_x/k_y) respectively. A very large stiffness ratio subsequently leads to the displacement in one plane only. This displacement is related to the force by:

$$F = \sum_i k_{yi} \delta^i \quad (1)$$

Where k_y and δ are the stiffness and the displacement of the structure in y -direction i can equal integer values between 1 and ∞ . The possible values of i are dictated by the assumptions made during the derivation of the representative form of Equation 1. k_{yi} are discrete values of the stiffness that are also determined this derivation. In its simplest linear form i is equal to 1 and $F = k_y \delta$ and hence called the “Linear Model” or “Linear Deflection theory”. For a fixed-fixed beam with the load ‘F’ applied at the center of the beam, Equation (1) becomes [40]:

$$F = \frac{192EI}{L^3} \delta \quad (2)$$

Where δ is the deflection at the centre of the beam.

There could be many different types of flexure springs, the most commonly used flexure springs are [41]:

- a) Fixed-fixed flexure
- b) Crab-leg flexure
- c) Folded flexure
- d) Serpentine flexure

2.1.1. Fixed-fixed flexure

Fixed-fixed flexure shown in Figure1 has a very stiff non-linear spring constants because of the extensional axial stress in the beam. They also have a very high stiffness ratio.

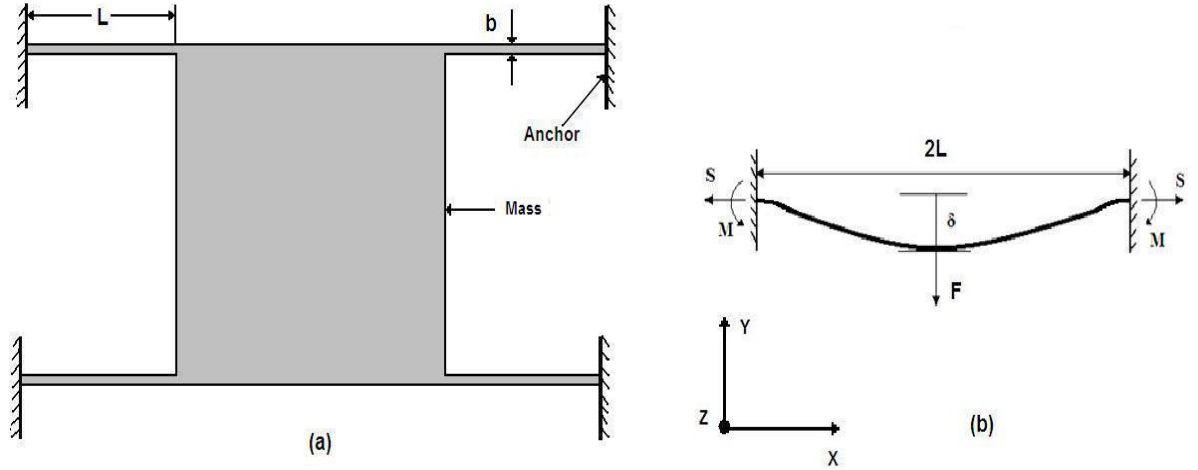


Figure 1: (a) Fixed-fixed flexure design. (b) Free body diagram of a fixed-fixed beam

The derivation of the behavior of the fixed-fixed beams is given by [42] the applied load 'F' at the center of the beam and the deflection can be found by solving the following equations simultaneously.

$$\delta = 2 \left(\frac{2I}{A} \right)^{1/2} (u - \tanh u) \left(\frac{3}{2} - \frac{1}{2} \tanh^2 u - \frac{3 \tanh u}{2u} \right)^{-1/2} \quad (3)$$

$$F = \frac{8EI}{L^3} \left(\frac{2I}{A} \right)^{1/2} u^3 \left(\frac{3}{2} - \frac{1}{2} \tanh^2 u - \frac{3 \tanh u}{2u} \right)^{-1/2} \quad (4)$$

$$u = \sqrt{\frac{S}{EI}} \frac{L}{2} \quad (5)$$

Pisano et. al. [25] approximate the expressions for the nonlinear spring constants as:

$$k_x = \frac{4AE}{L} \left\{ 1 - \left[\left(1 + \frac{x}{L} \right)^2 + \left(\frac{\delta}{L} \right)^2 \right]^{-1/2} + \left(\frac{L+x}{L} \right)^2 \left[\left(1 + \frac{x}{L} \right)^2 + \left(\frac{\delta}{L} \right)^2 \right]^{-3/2} \right\} \quad (6)$$

$$k_y = \frac{4AE}{L} \left\{ 1 - \left[\left(1 + \frac{x}{L} \right)^2 + \left(\frac{\delta}{L} \right)^2 \right]^{-1/2} + \left(\frac{\delta}{L} \right)^2 \left[\left(1 + \frac{x}{L} \right)^2 + \left(\frac{\delta}{L} \right)^2 \right]^{-3/2} \right\} \quad (7)$$

Where 'A' is the cross-sectional area, 'S' is the axial force, 'E' is the Young's modulus and 'I' is second moment of inertia of the beam. 'x' and 'δ' are the displacements in x and y directions respectively. Equations (6) and (7) are both scaled by $4AE/L$ and are coupled together. There is no way to de-couple these two equations and express k_x and k_y independently. Thus the fixed-fixed flexure has highly nonlinear characteristics.

Comparison of this non-linear behavior to the linear theory (Eqn. (2), with $L=500$) is shown in Figure 2. It can be noted that for small deflection roughly up-to the $1/4$ of the width of the beam the behavior of the fixed-fixed beams can be estimated by using the linear deflection theory [19].

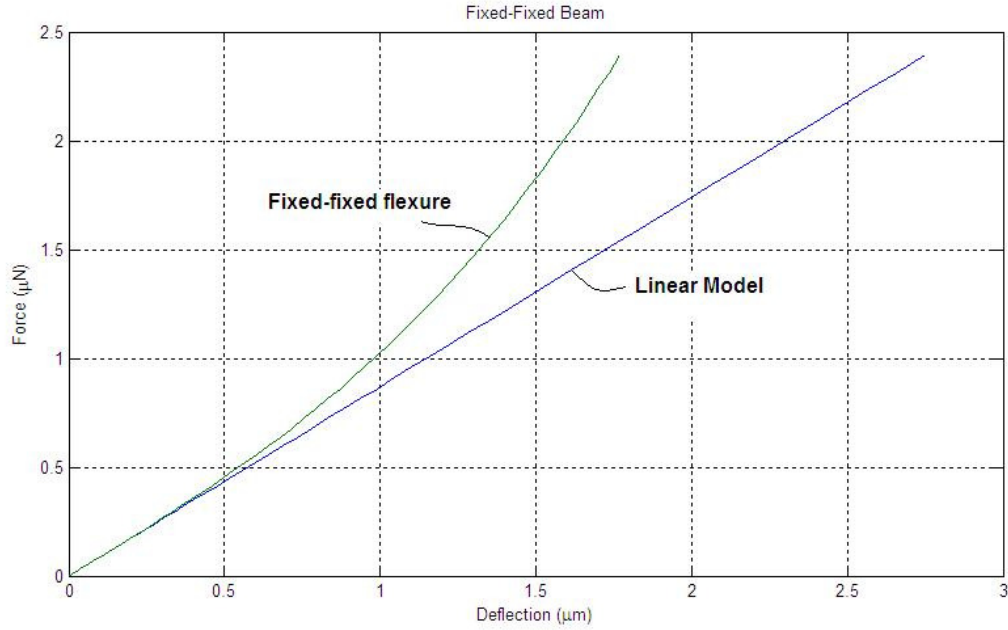


Figure 2: Deflection of Fixed-fixed beam with dimension (h X b x 2L) 20 x 2 x 1000µm under the force applied at the centre

Compressive residual stresses are often induced in the beams during the fabrication and they can cause these beams to buckle. This post buckling force was related to the δ in [43] as:

$$P = P_{Cr} \left[1 + \frac{\delta}{4L} + 3 \left(\frac{\delta}{4L} \right)^2 + \frac{25}{2} \left(\frac{\delta}{4L} \right)^3 + \dots \right] \quad (8)$$

$$P_{Cr} = \frac{\pi^2 EI}{L^2} \quad (9)$$

'P' is the compressive residual force acting in the in the x direction and adds to the normal force 'S' (5) that develops in the beam as a result of the applied force 'F'.

A ratio of force to displacement allows for the examination of this system's stiffness.

A ratio of F/δ :

$$k_y = \frac{4EIu^3}{L^3(u - \tanh u)} \quad (10)$$

Where $u \propto \sqrt{S}$ (Equation (5)), and implies that the increase in 'S' due to the addition of 'P' increases the beam stiffness. Therefore it can be concluded that the compressive residual stresses in the post buckled beam tend to increase the stiffness of the fixed-fixed flexure.

2.1.2. Crab-Leg Flexure

A novel variation of the fixed-fixed flexure is the crab-leg flexure shown in the Figure 3. The added thigh section, length 'La' minimizes the peak stresses in the flexure at the cost of minimized stiffness in the x direction which is mostly undesired. The deflection of the thigh also reduces the extensional stresses [25].

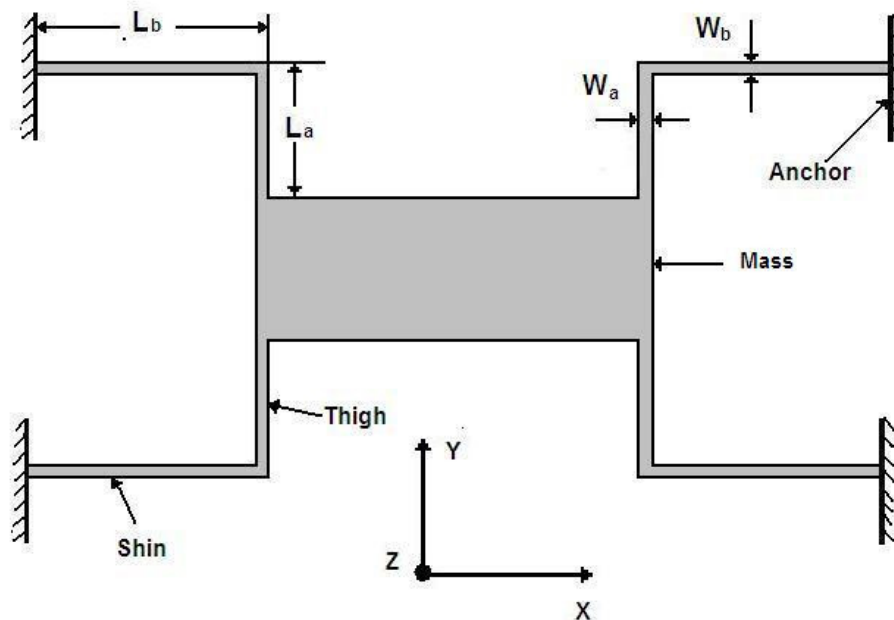


Figure 3: Crab-Leg flexure design

Fedder [41] derives and presents the stiffness of the crab-leg flexure as:

$$k_x = \frac{Et w_a^3 (L_b + 4\alpha L_a)}{L_a^3 (L_b + \alpha L_a)} \quad (11)$$

$$k_y = \frac{Et w_b^3 (4L_b + \alpha L_a)}{L_b^3 (L_b + \alpha L_a)} \quad (12)$$

Where α is defined as:

$$\alpha \equiv \frac{I_b}{I_a} \equiv \left(\frac{w_b}{w_a}\right)^3 \quad (13)$$

' I_a ' and ' I_b ' are the second moments of inertia of the thigh and shin segments respectively and 't' is the thickness of the structure.

From (11) and (12) it can be noted that the stiffness, k_x and k_y of the crab-leg flexure unlike the fixed-fixed flexure, can be varied almost independently of each other by varying the values of lengths and widths of thigh and shin segments. The crab-leg flexure has linear characteristics closely matching the linear deflection model (Eqn. (2), with $L = L_b$) for small deflections as shown in Figure 4, with a compromise of compliant behavior in undesired x-direction. Compliance in the x-direction is undesirable because the motion in the x-direction could offset application of load in y-direction.

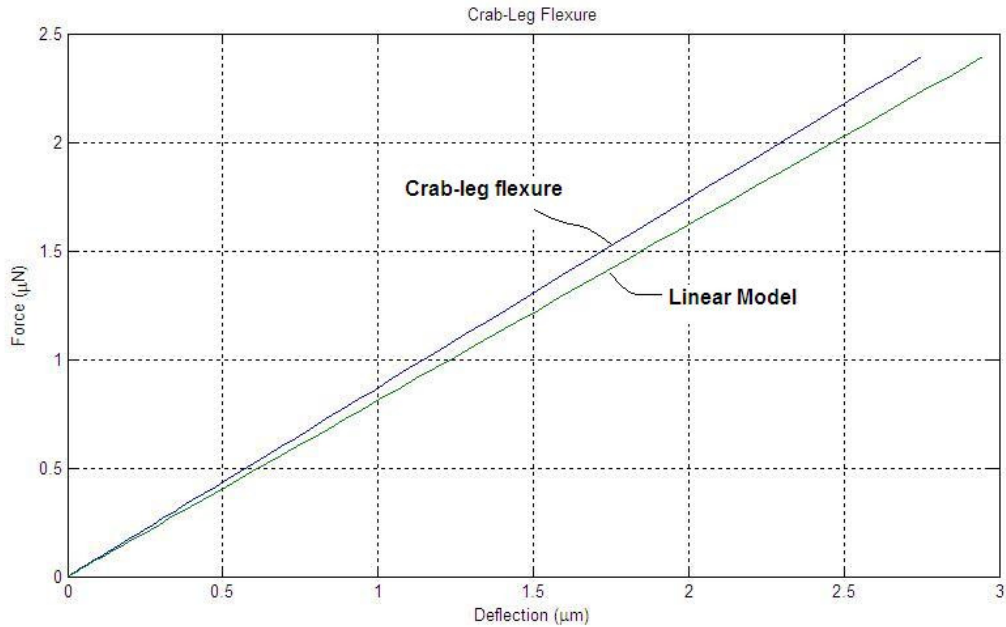


Figure 4: Deflection of crab-leg flexure (in y- direction) with dimensions $L_a = 500\mu\text{m}$ $L_b = 50\mu\text{m}$ $W_a = W_b = 2\mu\text{m}$ and $t=20\mu\text{m}$

2.1.3. Folded Flexure

Folded flexure shown in Figure 5 is another design which offers a good compromise of linear behavior to an extent in the desired y-direction and added stiffness in the undesired x-direction. The problems associated with the residual stresses are also minimized because the trusses that connect the beams together allow for the contraction and elongation while the beams are anchored at the center.

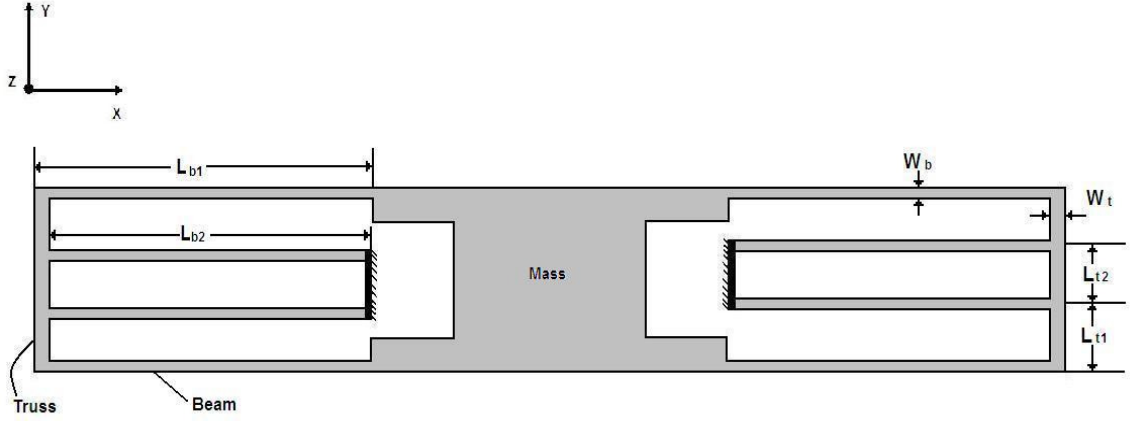


Figure 5: Folded flexure design

Detailed derivation of the stiffness is given by [41] where it is defined as:

$$k_x = \frac{24EI_{zt}}{L_t^3} \frac{(8\tilde{L}_t^2 + 8\tilde{L}_t\alpha + \alpha^2)}{(4\tilde{L}_t^2 + 10\tilde{L}_t\alpha + 5\alpha^2)} \quad (14)$$

$$k_y = \frac{24EI_{zb}}{L_b^3} \frac{(\tilde{L}_t^2 + 14\tilde{L}_t\alpha + 36\alpha^2)}{(4\tilde{L}_t^2 + 41\tilde{L}_t\alpha + 36\alpha^2)} \quad (15)$$

Where $L_t = L_{t1} = L_{t2}$; $L_b = L_{b1} = L_{b2}$; $\alpha = \frac{I_{zt}}{I_{zb}}$; $\tilde{L} = \frac{L_t}{L_b} I_{zt}$ and I_{zb} are the second moment of inertia of the beam and truss elements.

Judy [44] has also presented a review of several variations of folded flexure along with the analysis.

Comparison of the folded flexure with the linear deflection model is presented in Figure 6.

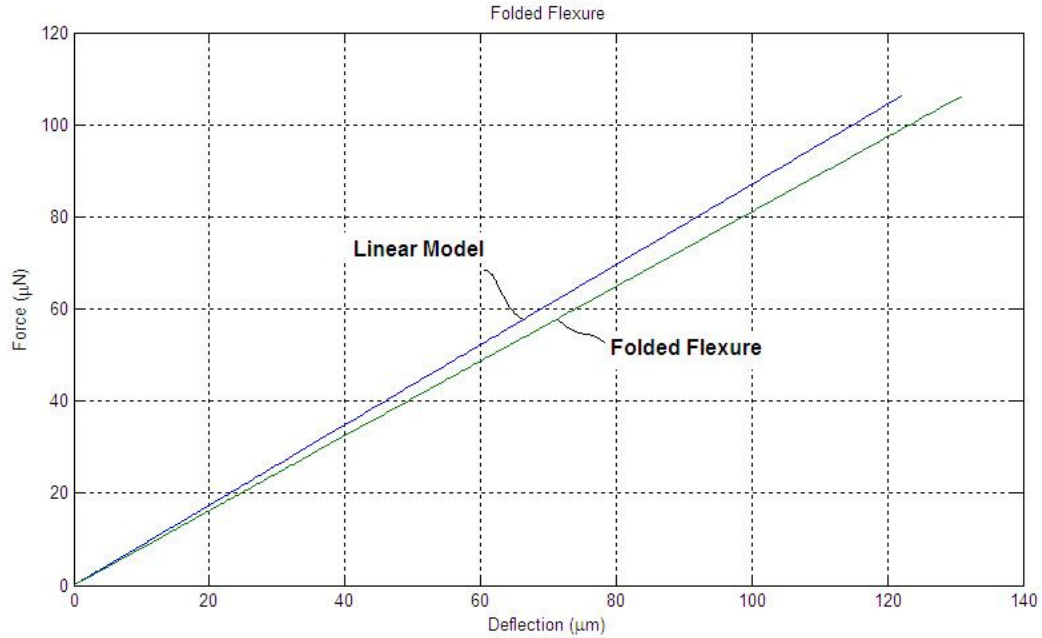


Figure 6: Deflection of Folded flexure (in y-direction) with dimensions $L_t = 500\mu\text{m}$; $L_b = 50\mu\text{m}$ $W_t = W_b = 2\mu\text{m}$ and $t = 20\mu\text{m}$

It can be noted from Figure 6 that the folded flexures displays a fairly linear behavior which can roughly be estimated with the linear displacement model (Eqn. (2), with $L = L_{b1}$) upto 10% of the beam length. This design is suitable for large deflections and therefore very widely used. Another aspect that needs consideration in the design of folded flexures is the dependence of axial stiffness of the flexure to the deflection in the y-direction. This relationship is given by [19].

$$k_x = \frac{200EI}{3L_b\delta_y^2} \quad (16)$$

It can be seen from the relationship above that axial stiffness of the folded flexure decreases with the increase in the lateral displacement.

2.1.4. Serpentine Flexure

The serpentine flexure shown in Figure 7 gets its name from the snake like pattern of the spring elements. Each meander has a length of 'a' and width of 'b'. The first and last segments of the meander can be of different length 'c' (usually $b/2$) or they can be of same length as that of the other segments. Beam segments that span the meander are called "spans" and the beams that connect the spans are called connector beams.

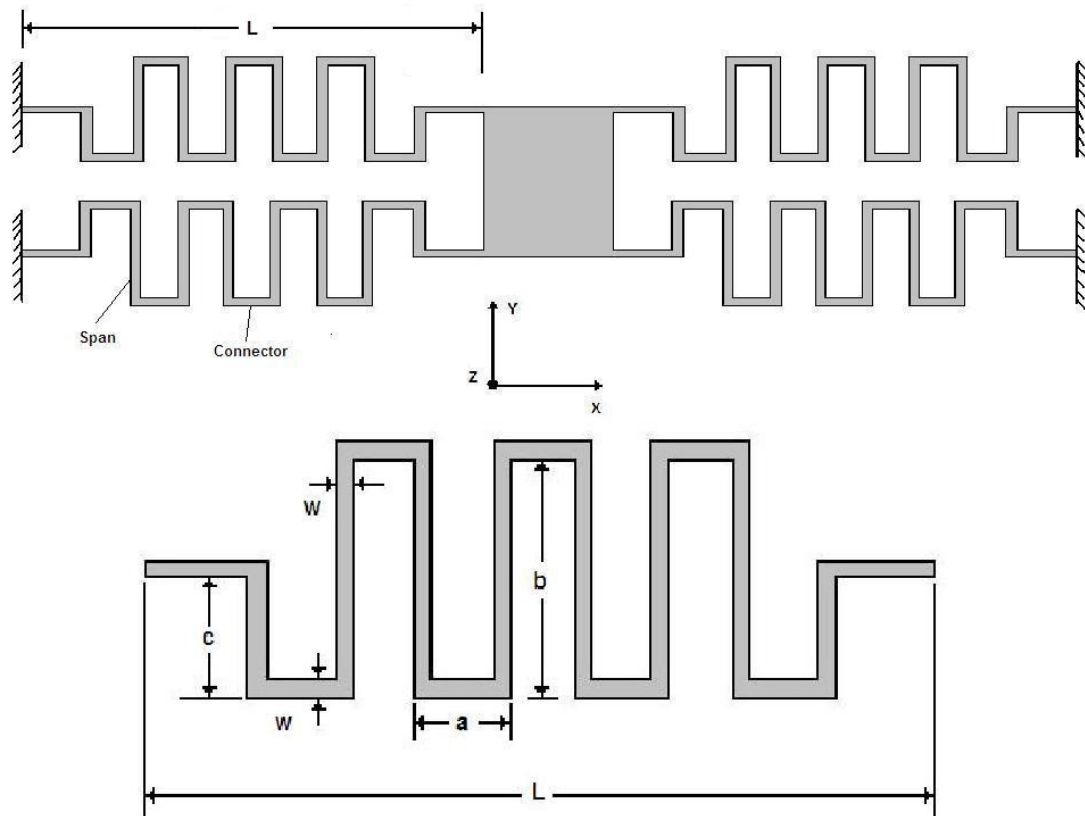


Figure 7: Design of Serpentine flexure

Serpentine flexure design offers the advantage of a compliant structure compact space. The stiffness ratio of the flexure can be adjusted by changing the width of

the meander 'a'. The meandering structure also relieves the residual and extensional stresses. The formulas for the stiffness of the serpentine flexure are presented by [41].

For an even number of 'n' meanders the stiffness are defined as:

$$k_x = \frac{48EI_{zb}[(3\bar{a}+b)n-b]}{a^2n[(3\bar{a}^2+4\bar{a}b+b^2)n^3-2b(5\bar{a}+2b)n^2+(5b^2+6\bar{a}b-9\bar{a}^2)n-2b^2]} \quad (17)$$

$$k_y = \frac{48EI_{zb}[(\bar{a}+b)n^2-3bn+2b]}{b^2[(3\bar{a}^2+4\bar{a}b+b^2)n^3-2b(5\bar{a}+2b)n^2+(5b^2+6\bar{a}b-9\bar{a}^2)n-2b^2]} \quad (18)$$

For odd number of 'n' meanders the stiffness is defined as:

$$k_x = \frac{48EI_{zb}}{a^2n[(\bar{a}+b)n^2-3bn+2b]} \quad (19)$$

$$k_y = \frac{48EI_{zb}[(\bar{a}+b)n-b]}{b^2(n-1)[(3\bar{a}^2+4\bar{a}b+b^2)n+3\bar{a}^2-b^2]} \quad (20)$$

Where

$$\alpha \equiv \frac{I_{zb}a}{I_{za}}$$

I_{za} and I_{zb} are the second moment of inertia of the connector and span elements respectively. Comparison of serpentine flexure to the linear model shown in Figure 8 below indicates that linear model (Eqn. (2), with $L = 500\mu\text{m}$) can be used to estimate the small deflections of serpentine flexure.

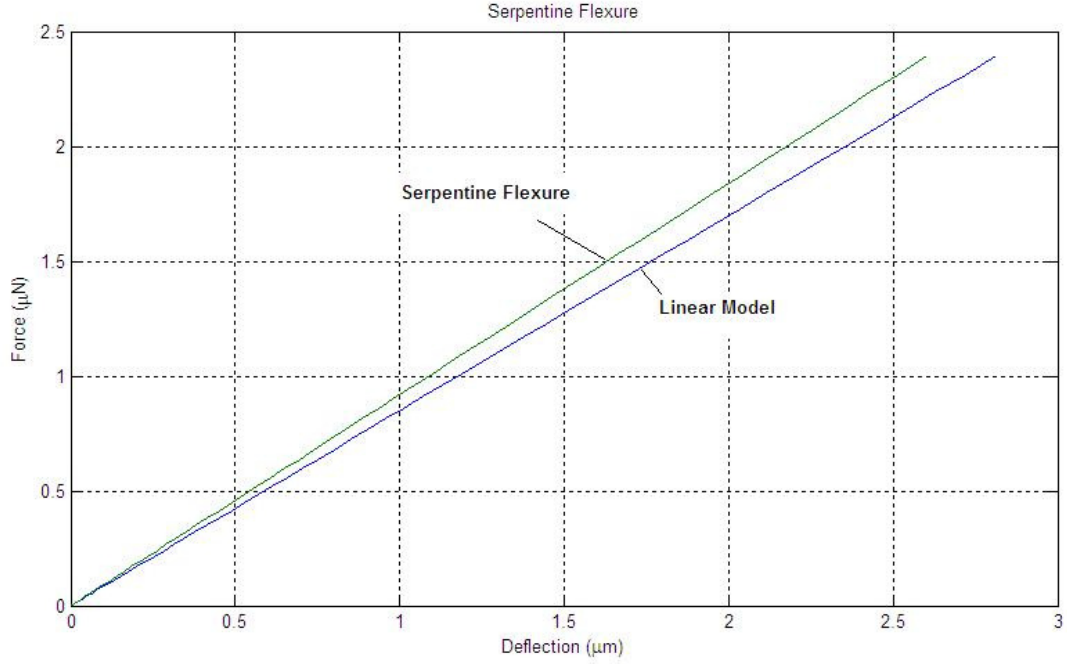


Figure 8: Deflection of serpentine flexure (in y-direction) with dimensions $a = 20\mu\text{m}$, $b = 20\mu\text{m}$, $w = 2\mu\text{m}$, $n = 20$ and $t = 20\mu\text{m}$

2.2. Electrostatic Force

To simplify the modeling, the electrostatic field between the fixed set of combs and the compliant set of combs is approximated by one dimensional parallel plate model between engaged parts of the combs. Therefore the 3D complex fringing fields, comb finger end effect, ground plane effects and levitation are neglected for simplicity [45]. This simplification results in the underestimation of lateral electrostatic force by about 5% [19]. The Capacitance between the comb fingers in configuration shown in figure 9 is:

$$C = \frac{2n\epsilon_0 t(l_0 + l)}{g} \quad (21)$$

Where ‘ n ’ is the number of combs, ‘ ϵ_0 ’ is the dielectric constant, ‘ t ’ is the height of the comb fingers, ‘ g ’ is the gap spacing between the fingers, ‘ l_0 ’ and ‘ l ’ are the initial overlap and the comb displacement as a result of the application of the voltage.

The lateral electrostatic force in the y -direction is equal to the negative derivative of the electrostatic co-energy with respect to displacement in y direction:

$$F_{el} = \frac{1}{2} \frac{\partial C}{\partial l} V^2 = \frac{n\epsilon_0 t}{g} V^2 \quad (22)$$

Note the relationship between force and voltage is nonlinear and that the other terms are constants. In the case of parallel plate capacitors (another less common method of actuation) not only is the force nonlinear with respect to the applied voltage, but also with the gap (g) between the opposing electrodes. This is the main reason for the popularity of the comb capacitor configuration.

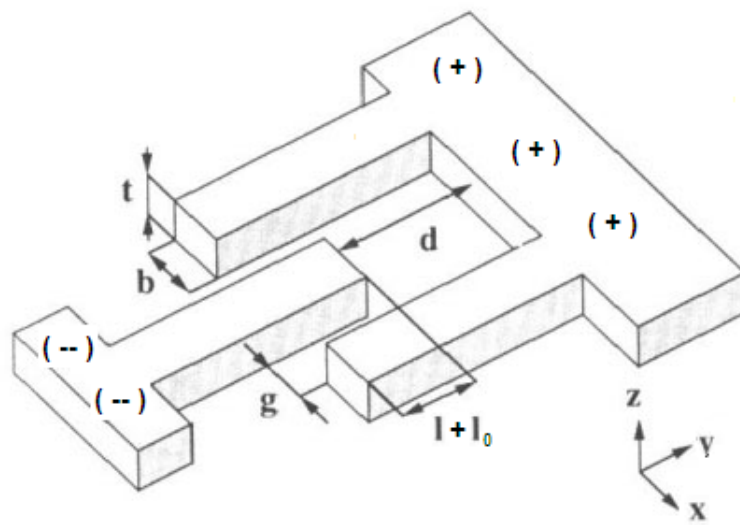


Figure 9: Schematic details of comb fingers.

This electrostatic force produced as a result of the application voltage causes the movement of the compliant set of comb structure to move in the lateral (y-direction). This deflection given by:

$$l = \frac{n\varepsilon_0 t}{k_y g} V^2 \quad (23)$$

2.2.1. Side (Axial) Instability

When the voltage is applied across the opposing comb structures, besides the electrostatic forces along y-direction electrostatic force is also produced in the x-direction. This axial electrostatic force tends pull the fingers together. The electrostatic force generated by both side of the parallel plate capacitor assuming 'x' displacement in x-direction is given as:

$$F_x = \frac{n\varepsilon_0 t(l_0+l)}{2(g-x)^2} V^2 - \frac{n\varepsilon_0 t(l_0+l)}{2(g+x)^2} V^2 \quad (24)$$

Hirano [24] showed that a critical spring constant when the side instability occurs and fingers stick together is stated as:

$$k_{x_{cr}} = \left. \frac{\partial F_x}{\partial x} \right|_{x \rightarrow 0} = \frac{2n\varepsilon_0 t(l_0+l)}{g^3} V^2 \quad (25)$$

As long as $|k_x| > |k_{x_{cr}}|$, instability would not occur. Both the terms are independently controlled. k_x is determined by the flexure design and $k_{x_{cr}}$ is

determined by the overlap length, finger gap, and the applied voltage. Therefore the maximum applied voltage bias and hence the allowable maximum deflection is limited by the side instability.

2.2.2. Front (Lateral) Instability

In addition to the side instability, sometimes the front instability causes the fingers stick at the front end. This occurs because there is also an electrostatic force at the front end of the finger. A rough estimation of this force is given by:

$$F_p = \frac{n\varepsilon_0tb}{(d-l)^2}V^2 \quad (26)$$

Where 'd' is the distance from the front end of the moving finger to the base of the stationary finger, 'b' is the finger width. 'y' is the displacement of the finger in y-direction when no actuation occurs. For an actuator to be in equilibrium the total electrostatic force produced should then be equal to the restoring force of the flexure's spring(s).

$$F_s = F_{el} + F_p \quad (27)$$

Also the change in the spring force has to be greater than the electrostatic force at the front end [21].

$$\frac{\partial F_s}{\partial l} \geq \frac{\partial F_p}{\partial l} \quad (28)$$

By eqns. (26) and (27) maximum allowable displacement x_{max} of the actuator system can be calculated. The equation of x_{max} is usually a third order

polynomial with finger width 'b', finger gap 'g' and the initial distance 'd' as the variables.

Chapter 3

DESIGN AND FABRICATION

3.1. Design specifications

To design a MEMS comb drive actuator capable of material testing in-situ in a TEM, it is important that its design specifications are identified. In order to do so we assume a specimen made of gold. Gold is very widely used in MEMS devices as its chemical inertness and resistance to oxidation makes it preferable over Aluminum. At the macro scale, the most commonly used test for the determination of the material properties is subjecting of the standard dog-boned shaped specimens to tensile test. Similar method can be utilized for the material testing at the micro scale however the cross section of the specimen is changed from being circular to square for the ease of fabrication using the standard MEMS fabrication techniques. The equipment at Manufacturing Training and Technology Center (MTTC) clean room at the University of New Mexico limits the minimum line width that could be fabricated to $1\mu\text{m}$. therefore the sample is assumed to have the width of $1\mu\text{m} - 2\mu\text{m}$. The thin film thicknesses of interest for most research groups range between 50nm to 500nm (the upper limit has been exaggerated in order to overdesign the actuator). $450\mu\text{m}$ was deemed an appropriate length for the specimen.

Once the dimensions and the material for the specimen to be tested are specified the specifications for the actuator are very easily determined. We assume the maximum displacement that the actuator would have to displace is $10\mu\text{m}$. If 0.1%

strain to the specimen is required for the study and since the Young's modulus of gold is 78GPa then strain is related to the elastic modulus as:

$$E = \frac{\sigma}{\epsilon} \quad (29)$$

Where the engineering stress ' σ ' is defined as the force (F) per unit cross sectional area (A) of the specimen

$$\sigma = \frac{F}{A} \quad (30)$$

Therefore, for a specimen of cross sectional area $2\mu\text{m} \times 500\text{nm}$, the actuator should be capable of producing approximately $78\mu\text{N}$ of force in addition to the force required to overcome the restoring force of the spring flexure.

In order to avoid arcing between the opposing comb fingers or between the comb and the substrate the required force should be generated at low voltage say ~ 40 Volts. This electrical breakdown voltage of air depends on the geometry of the electrode gap, the gas and the pressure in the gap. A generalized relationship for this breakdown voltage is given by "*Paschen's Law*". The value of 40 Volts is based on this author's prior experience with MEMS devices of similar geometry and physical dimensions.

The design of the MEMS comb drive actuator should also accommodate features that can be used for the calibration. Also the overall size of the device is such that it can fit into a TEM Holder for JEOL 2010 with the position of the specimen in the right place in order to conduct in-situ studies. There is also a need to etch

a through window in the substrate such as to allow the electron beam to pass through the specimen to be studied unhindered on to the TEM observation camera below. As mentioned earlier in Chapter 1 it is also required that the fabrication of the actuator and the specimen to be tested is to be done separately which provides more flexibility to the over-all design of in terms of the type of the specimen that can be tested by ensuring that the fabrication procedure of the specimen is not restricted by that of the actuator. Due to restriction of minimum resolvable line width by the available equipment it was concluded that the comb fingers on the actuator will be 2 μm wide and there will be 2 μm spacing between them. 10 μm overlap of the opposite fingers was considered sufficient. A vernier was also accommodated in the design so that the displacement of the compliant structure can be measured optically.

Having identified the specifications of the required MEMS comb drive actuators and theory described in Chapter 2, computer models (Appendix 'B') were generated for fixed-fixed, folded, and serpentine flexures. The number of combs required for each flexure and the flexure design parameters were determined from the model. These parameters are summarized in the table below:

Table 1: Design parameter for the MEMS com drive actuator

Flexure type	No. of Combs	Flexure dimension
Fixed-fixed beam	6000	$L = 400$
Folded beam	2000	$L_t = L_{t1} = L_{t2} = 100\mu\text{m}$ $L_b = L_{b1} = L_{b2} = 600\mu\text{m}$

Serpentine beam	600	$a = 20\mu m; b = \mu m;$ $c = \frac{a}{2}; n = 20$
-----------------	-----	--

A schematic of the proposed design with fixed- fixed flexure is shown in figure 10 and 11 below:

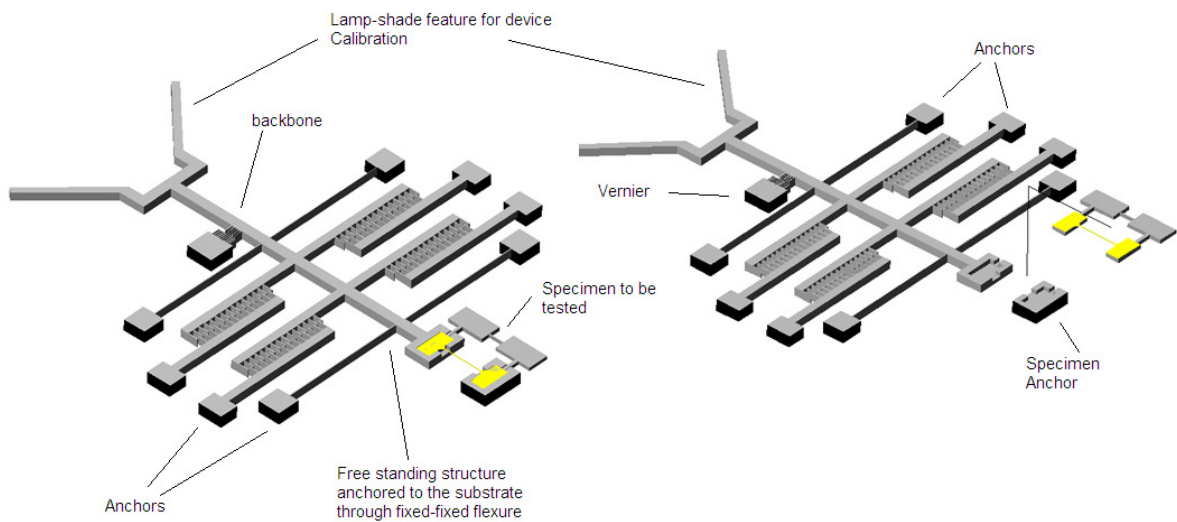


Figure 10: Schematic design of a Comb Drive Actuator with fixed-fixed flexure

As shown in figure 10 the device consists of a two sets of inter-digitated fingered structures, one set of fingers connected to the free standing backbone is anchored to the substrate via flexure (fixed in the figure above) making the complete structure compliant. Other set of the fingers is rigidly connected to the substrate.

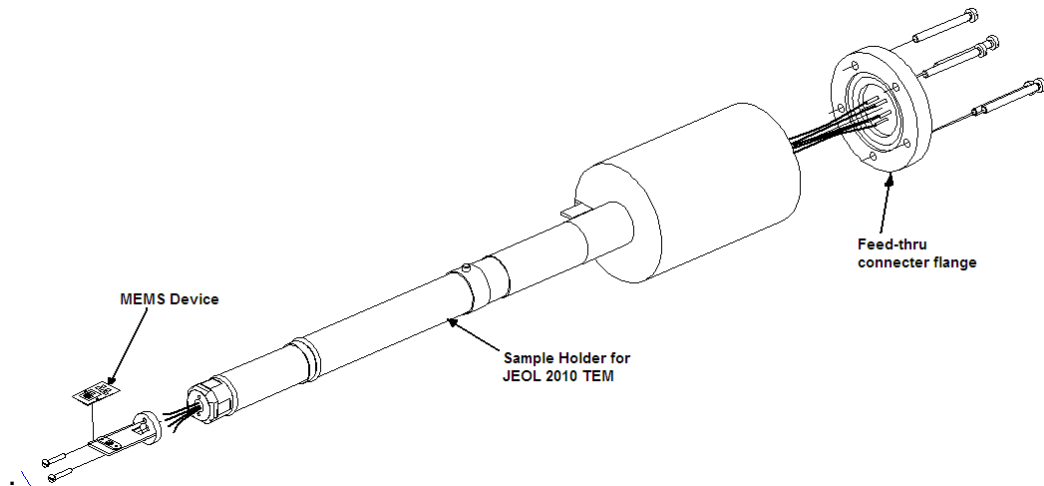


Figure 11: Schematic of a custom specimen holder for JEOL 2010 and the placement of the MEMS device

Figure 11 shows a schematic of a custom fabricated specimen holder for JEOL 2010 TEM with feed-thru wires to power and retrieve data from the MEMS device while under observation in TEM. The detailed manufacturing drawings for this custom TEM holder are included to this thesis as Appendix 'C'. Figure 12 below shows the actual TEM holder.



Figure 12: Custom manufactured TEM holder

3.2. Fabrication

3.2.1. Mask Design and Development

The first step in development and fabrication of a MEMS device is the design and development of photolithography masks. The mask is flat glass plate with the desired pattern usually of chrome. The mask is required to transfer the required pattern onto the light sensitive photoresist. The chrome pattern blocks the light exposure on the part of the wafer coated with photoresist underneath. Making parts of the photoresist soluble in the developer solution, thereby transferring pattern.

The mask was designed using the AutoCAD software and all the design considerations described above were accommodated in the design. As the MTTTC cleanroom facility is equipped for 6 inch wafers the masks designed were all 7"x7" suitable for 6" wafers. Three masks were designed 1) The basic actuator pattern, 2) Specimen cavity pattern and 3) A pattern to etch through the wafer to let the Electron beams pass through a requirement for the TEM analysis. After the completion of the design the CAD files were sent out to photomask manufacturer for fabrication.

3.2.2. Actuator Fabrication

The fabrication of the MEMS actuator was carried on Silicon on Insulator (SOI) wafer whose device layer was 20 μm , buried oxide (BOX) 1 μm and the handle layer was 600 μm thick. All crystal orientations were (100) and both device and handle layers were p-type doped with boron. The resistivity of the device layer

was 0.01 - 0.02 Ω -cm and >10 Ω -cm for the handle layer. The actuator structure was then patterned using a layer of photoresist (PR). The device layer was then etched to the BOX layer by deep reactive ion etching (DRIE) of Si, using the Bosch [46] Process. This process creates high aspect ratio structures by etching vertically down from the edge of the PR layer. Next, the PR layer is removed using acetone, isopropyl alcohol, and de-ionized water rinses respectively. Finally, an O_2 plasma is used to remove any small remaining amount of PR on the Si surface. Next, the specimen etch structure is patterned on to the wafer by using a thick photoresist and device layer is again etched 10 μ m deep to form a specimen cavity. Later, the through etch is patterned on the handle layer and the handle layer is etched all the way to the BOX layer. The photoresist is then stripped in photoresist stripper. Finally the free standing structure on the actuator is released by etching the BOX layer in HF bath. For the detailed process parameters please see Appendix 'A'. A schematic of the fabrication process is shown in Figure 13. The actual images of the fabricated devices are shown in Figure 14-16.

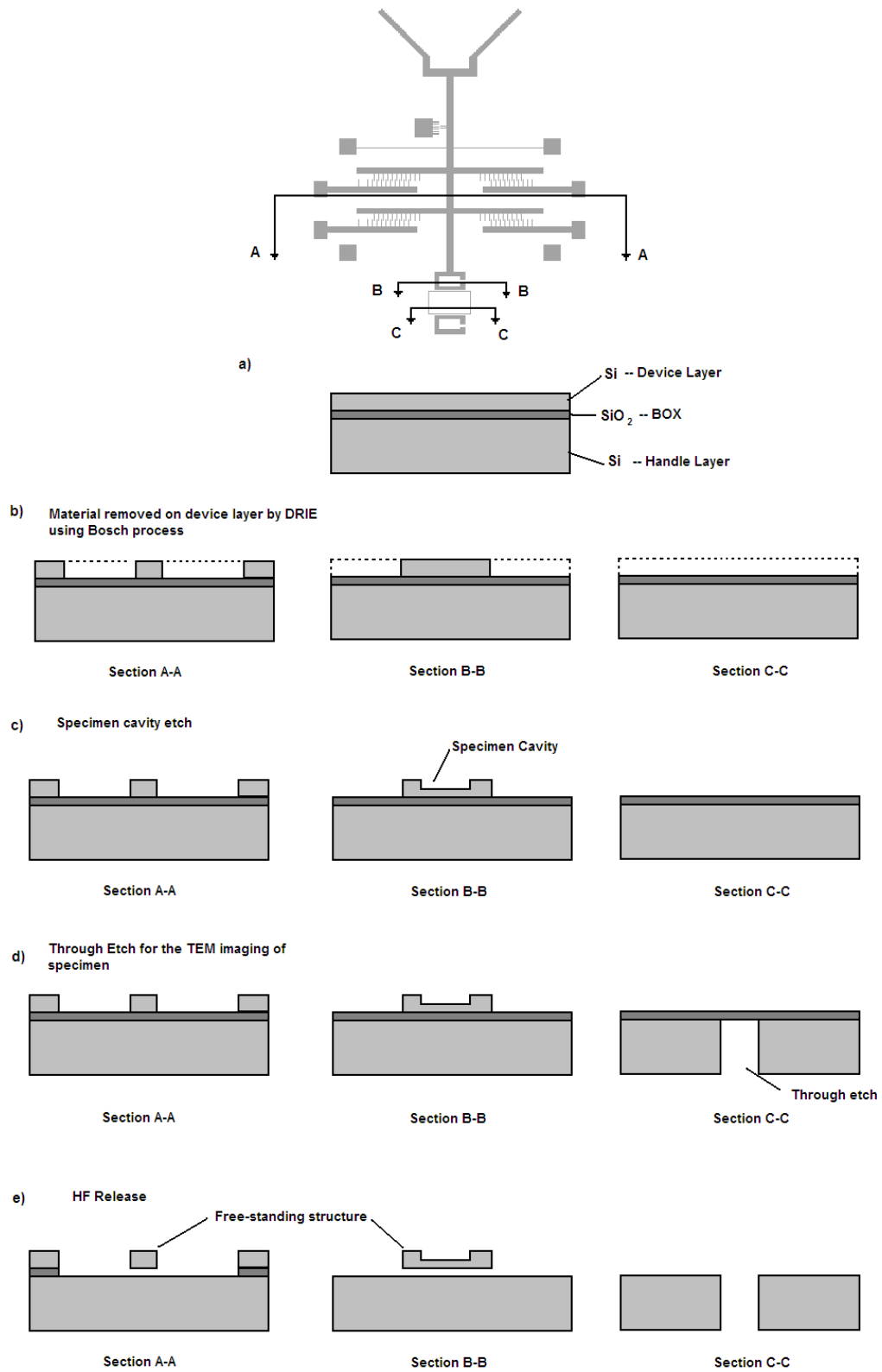


Figure 13: A schematic showing the fabrication process of the MEMS actuator

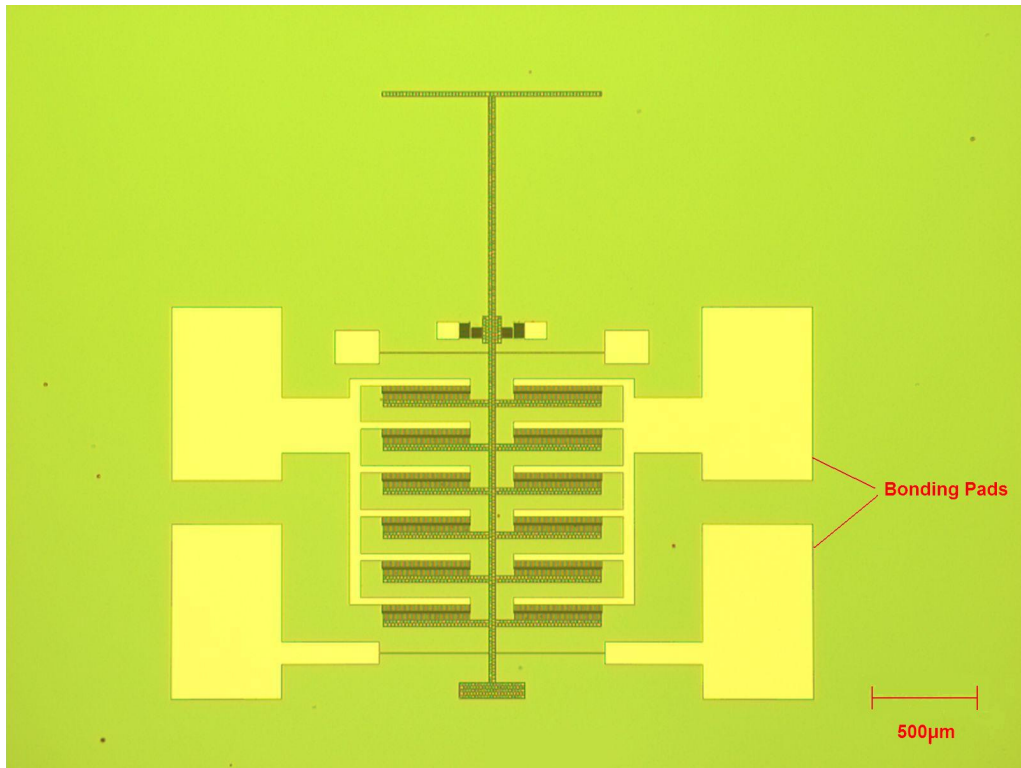


Figure 14: Optical micrograph of the actuator with fixed-fixed flexure, $L=800$, $n=600$

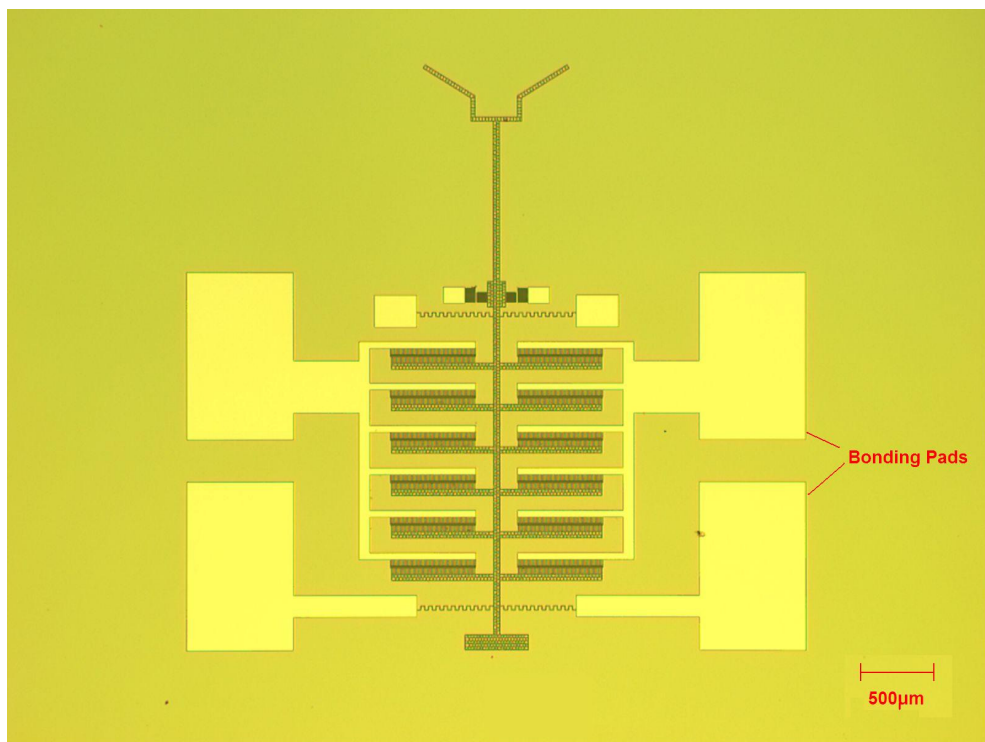


Figure 15: Optical micrograph of the actuator with serpentine flexure and $n=600$

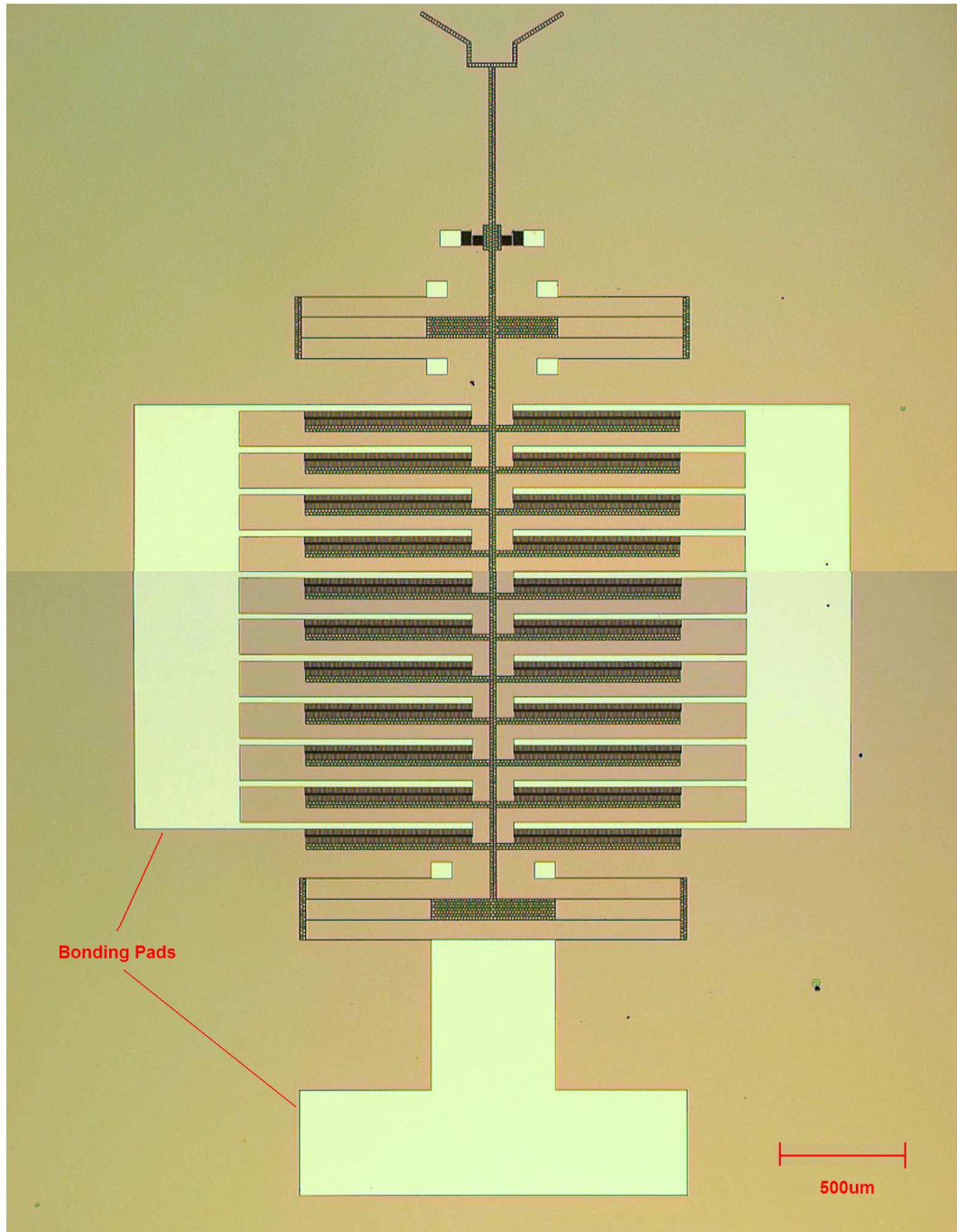


Figure 16: Optical micrograph of the actuator with Folded flexure and $n=2000$

Chapter 4

TESTING AND CALIBRATION

This chapter describes the setup and the procedure employed for testing and calibrating the fabricated MEMS actuators.

4.1. Side Instability Voltage

The determination of the side instability voltage is important because the instability voltage limits the amount of force that can be generated by the comb fingers before they stick to each other and electrically short out the device. This determination of the side instability voltage and hence the maximum force that the device can be used to apply is a major factor in determining the application for which a particular device can be used.

4.1.1. Setup

The testing for the side instability voltage of the MEMS actuator was done on a Probe-station. The wafer was placed on the probe station stage and held with the vacuum. The probe tips were brought in contact with the bonding pads on the device. The probe station tips were connected to the Agilent E3612A power supply to operate the device. The probe station microscope was used to observe the device while in operation. The complete setup is shown in the Figure 17 and 18 below:

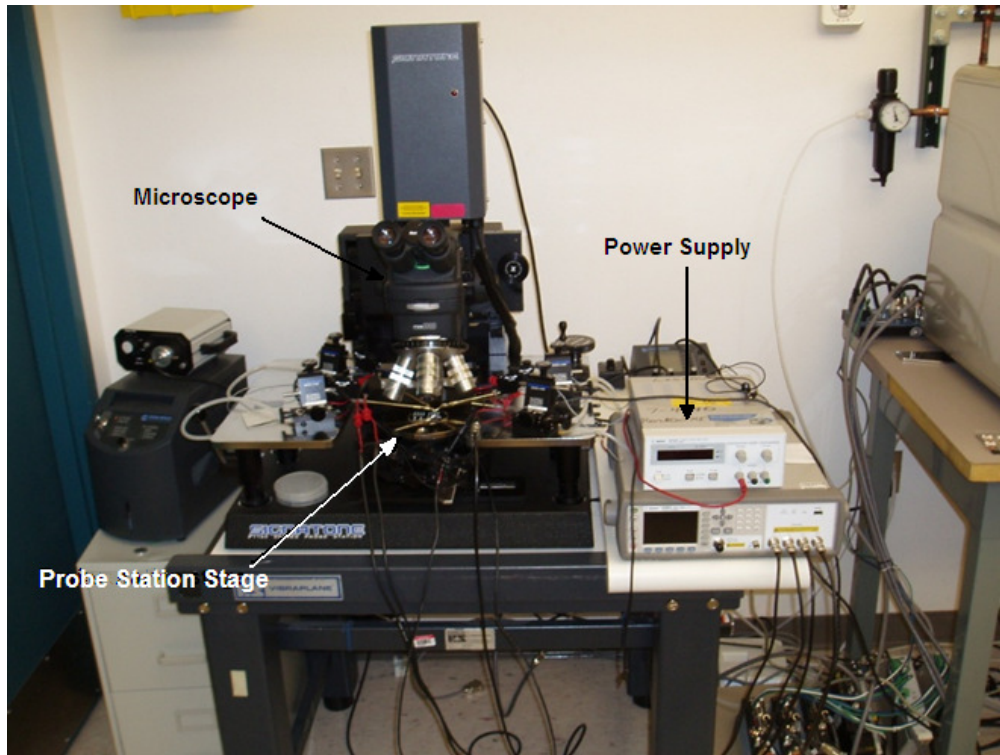


Figure 17: Experimental setup used to determine the side instability



Figure 18: Probe tips in contact with bonding pads of a MEMS actuator

4.1.2. Procedure

In order to determine the side instability voltage of the MEMS actuator positive bias was applied to the fixed structure and while compliant structure was grounded. The substrate (handle layer of the wafer) was also grounded by grounding the probe station stage. The voltage was increased in the increments of 1V and the combs on the actuator were observed through the microscope. The voltage at which the opposite comb fingers start to come closer to each other laterally is the side instability voltage. The laterally movement of the comb fingers can be observed through the microscope and corresponding voltage is noted.

4.2. Calibration

Measurement of small forces (fN to nN) are the cause of numerous scientific breakthroughs in the last few decades. The vast majority of force measurements made below a μN are for the purpose of determining material properties. Examples are: measurement of single ligand-receptor interactions ($\sim\text{fN}$ – pN) using the Surface Force Apparatus (SFA) [47,48], measurement of the mechanical properties of nanostructures (nN–mN) using Nano / Microelectromechanical Systems (NEMS/MEMS) [49,38,43], and a plethora of measurements have been made on the range of pN to nN using the Atomic Force Microscope (AFM). These measurements are becoming increasingly common, yet there is no traceable method of calibrating this full range of forces [50]

The NanoManufacturing Industry is not prepared for mass production of products utilizing nanotechnology. Scientists are constantly synthesizing and fabricating

novel nanomaterials and nanodevices (NEMS). Clearly transitioning these NanoScience discoveries into the NanoManufacturing realm would allow society to reap the reward of decades of scientific work. Yet NanoManufacturing of such products requires a nanometrology infrastructure that is lacking in many respects. Nanometrology is a term that, currently, implies measurements at the nanoscale and below. As such force metrology at sub-nN scales is considered to be a part of the nanometrology world.

Why is nanometrology important? Materials with dimensions on the nanoscale can have drastically different properties from their bulk counterparts. For example, bulk gold is a noble metal, i.e. it is inert. Yet nanoparticles (~2 nm) of gold have a high chemical reactivity and are employed as catalysts. Similarly, shrinking down to the nanoscale changes the density of electronic states of a material giving to different electrical and optical properties and it also affects the mechanical properties of the material [51].

Traceable force calibrations are necessary to allow for the measurement of the mechanical properties of materials. More specifically, it is essential that measurements of mechanical properties be made using standardized methods with International System of Units (SI) traceable equipment. Without standardized testing methods and SI traceable equipment, bridges and building would fall and pressure vessels would explode as a result of improper design. As an example of this necessity, consider the elastic modulus of steel. Using standard testing methodologies (ASTM E 111) and SI traceable equipment we know that the elastic modulus of steel is typically 200 GPa. This value is

repeatable all over the world and is of extreme importance to Mechanical and Civil Engineers alike.

Next consider the elastic modulus of gold, an element that is particularly important to the semiconductor industry. The bulk value, measured using standard methods and SI traceable equipment is 77 GPa [52], whereas samples with cross-sectional dimensions under 1 micron have values that vary considerably. For example, Wu et al. report values for elastic moduli of gold between 45 and 107 GPa [53], while Espinosa reports that E_{gold} is “consistently” between 53-55 GPa [54], and Leseman et al. found that the E_{gold} was 76 GPa [49].

Are all these researchers correct? It may be that all measurements were correct, but in order to remove all doubt use of standard testing methods and SI traceable equipment should be undertaken. Again, shrinking dimensions to the nanoscale will change the behavior of materials and systems, thus establishing standard testing methods and utilizing SI traceable equipment with proper force resolution is necessary. Because of the vast number of different methodologies of material growth, and geometries to which they conform, it will be some time before standard testing methodologies are developed for every material type and geometry. Therefore, because of the ingenuitive growth methods for materials, it can only be asked that researchers’ equipment be SI traceable and not force them to conform to standard testing methodologies. This is the more realistic and attainable short-term goal. Therefore all the MEMS devices fabricated for this

study were calibrated by employing a recently developed method traceable to NIST standards [39].

4.2.1. Setup

The calibration setup consists of two components, the MEMS actuator mount and the alignment setup. The actuator mount is prepared by cleaving the substrate just below the lamp-shade shaped feature on the actuator. The actuator is then carefully adhered to a glass microscope slide using double sided adhesive tape. In order to measure the capacitance change between the comb figures wirebonds are made from the bonding pads on the actuator to the copper tape on the glass (Figure 19). The leads from the Agilent 4980A precision LCR meter were later connected to the mounted actuator.

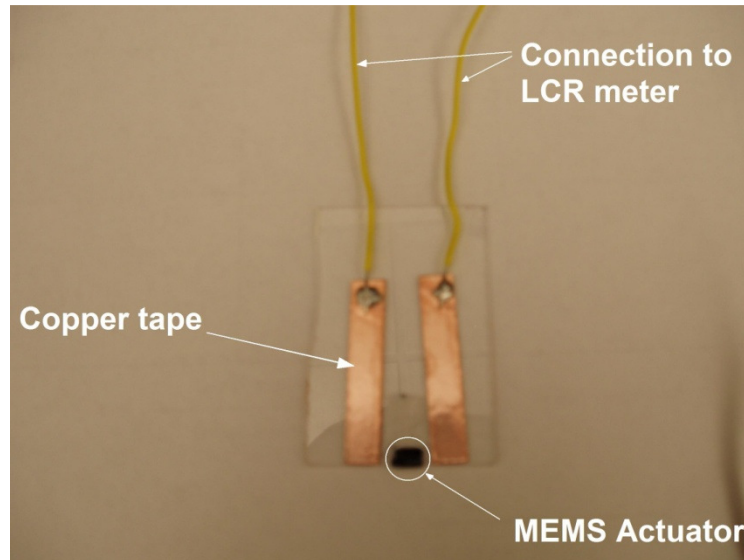


Figure 19: MEMS actuator mounted on the glass slide

The alignment setup consists of set of precision linear translation stages and a goniometer (Figure 20-22).

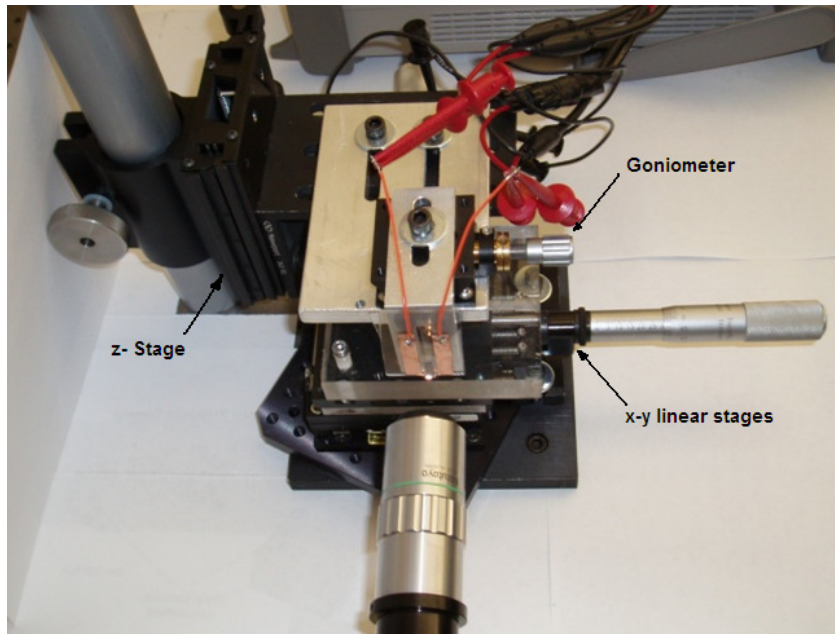


Figure 20: Glass slide mounted on the goniometer and independent linear stage for movement in z-direction

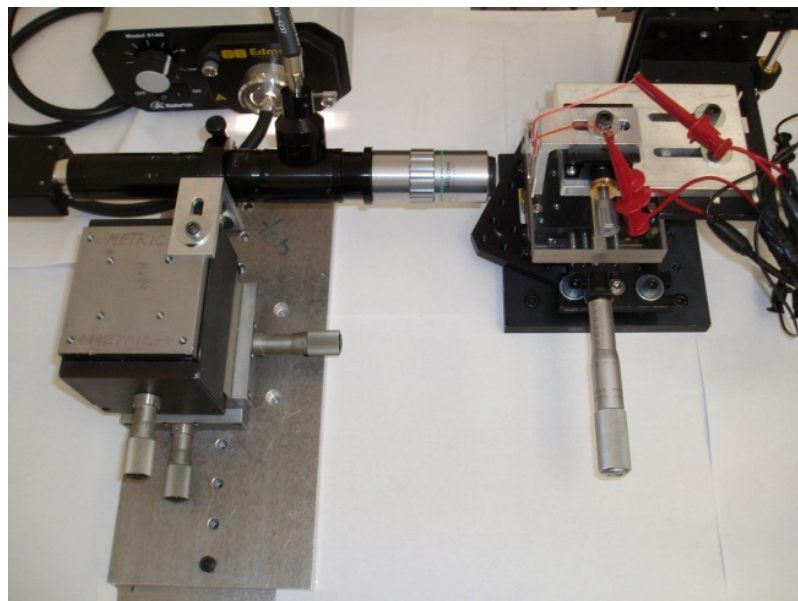


Figure 21: Microscope mounted on separate linear stages for independent x-y-z movement

The actuator was mounted onto a fixture that translates in the z-direction with a goniometer that allow for rotation around the x-axis. The alignment of ball lenses was carried out by mounting them on another set of x–y linear translation stages. A tube microscope with a CCD camera was also mounted on a separate set x-y-z linear translation stages for the ease of observation. An observation microscope with a CCD camera is mounted on separate x-y-z stages which makes it independent from the rest of the setup. The complete setup is shown in Figure 22 below:

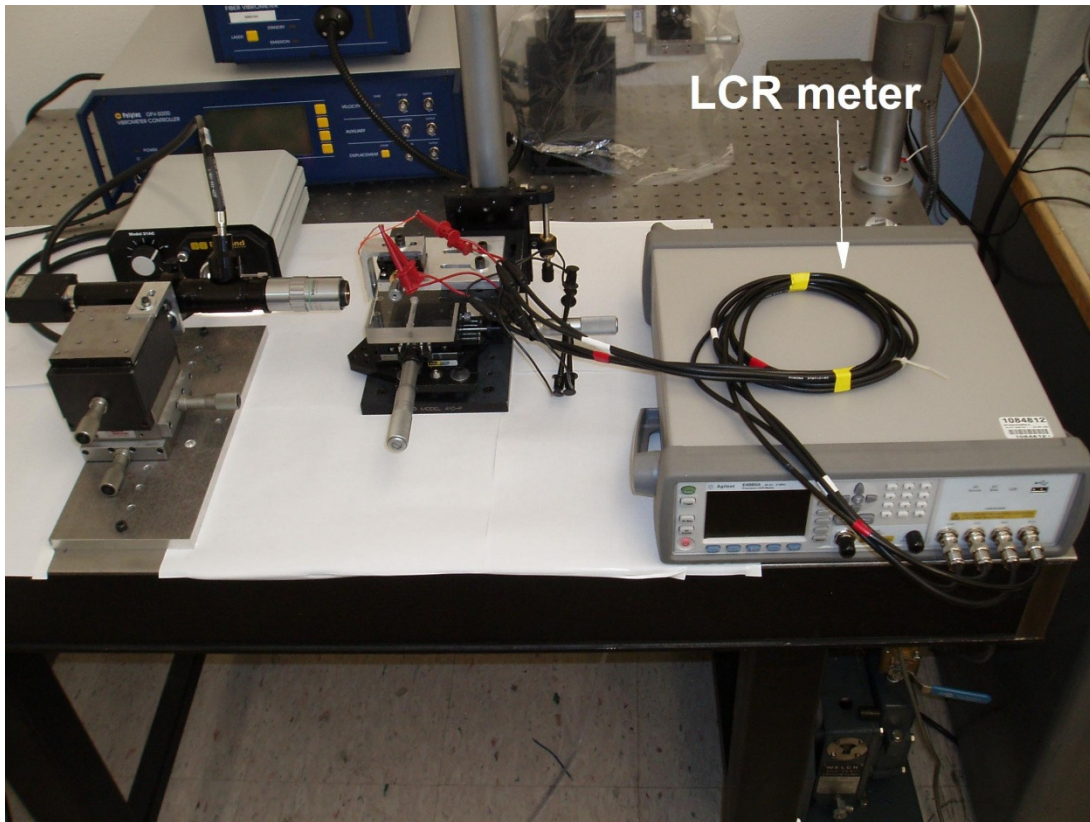


Figure 22: The complete calibration setup

4.2.2. Procedure

Calibration of the actuators is accomplished by recently developed calibration technique [55,39]. In order to calibrate known weights are hung from the portion of the actuator that extends beyond the cleave line of the wafer. After hanging the weight the change in capacitance between the comb fingers is measured with the LCR meter. Capacitance measurement provides very accurate displacement measurements with a tolerance of $\pm 100\text{nm}$. Hanging the weights, not surprisingly, requires extreme care. The weight is first properly aligned to the load cell using linear translation stages and goniometer. Weights were adhered to the load cell by using “secondary forces” and adhesives.

The calibration weights are commercially available sapphire ball lenses. These ball lenses are manufactured to tight specifications that allow great confidence in the weight of each sphere. The manufacturer’s specification for density, ρ , is $3.98 \pm 0.01 \text{ g/cm}^3$. Tolerances on all diameters was $\pm 2.54\mu\text{m}$. Independent verification was performed on several samples, through the use of a precision balance that is traceable to the National Institute of Standards and Technology (NIST), and it was found that all samples tested fall within the manufacturer’s specifications.

To attain a centrally loaded structure, proper alignment between the actuator and the ball lenses is necessary. This was accomplished through the use of three linear translation stages and a goniometer (Figure 19). The actuator was mounted onto a fixture that translates in the z-direction with goniometer that allow for rotation around the x-axis (axis perpendicular to the plane of the die). The ball

lenses were mounted onto a custom stage that allowed for the rigid temporary attachment of the ball lens to the x–y linear translation stages. Upon proper alignment of the actuator and ball lens to gravity the ball lens was adhered to the load cell.

A non-linear force–displacement response for the fixed-fixed beam structure was anticipated, thus a range of weights was hung from each load cell to capture the load cell’s non-linear response. For ball lenses measuring, 300 and 500 μm in diameter, it was possible, when the humidity was relatively low, to attach the balls using static electricity. When the humidity was relatively high, it was possible to attach the balls using water menisci formed by the condensed water from the humidity. Figure 23 shows an optical micrograph of a 790 μm sapphire ball lens attached in this manner to the load cell.

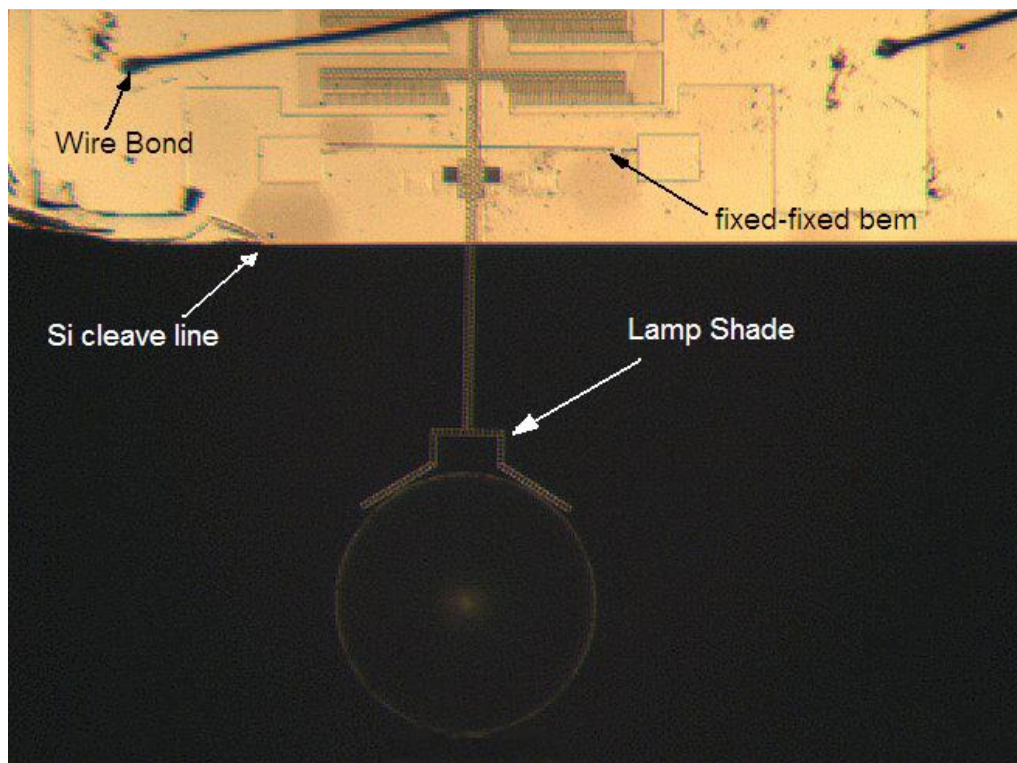


Figure 23: Optical micrograph of 790 μm sapphire sphere attached to the actuator

Images of spheres attached by static electricity are similar. Detachment of these smaller spheres was possible through the use of surface tension. A droplet of water was placed onto a substrate and the sphere was brought near. When the sphere was placed into contact with the water, the water quickly pulled the ball from the actuator without damage.

At the extreme end of our load range the large diameter spheres (1000 μm , 1500 μm) were attached using photoresist as an adhesive. These spheres were attached by dipping the load cell's tip into a droplet of photoresist (Figure 24). The photoresist wicked into the load cell's specially designed 'lamp-shade' tip, this 'wet' tip was then lowered into contact with a large diameter sapphire sphere. Solvents quickly escape the small volume of resist needed to adhere the ball lens to the load cell, especially under the intense light of the microscope. It was possible to detach the spheres by vibrating the load cell. This was done at some risk though, as some devices were damaged in this process. An alternate method of removal of the ball lens and photoresist was performed by placing a dish of acetone under the load cell and ball lens assembly. The acetone vapor quickly weakens the positive photoresist because of the large dose of light it has received from the focused light of the microscope. Submersion of the ball lens and device was not necessary for ball lens removal.

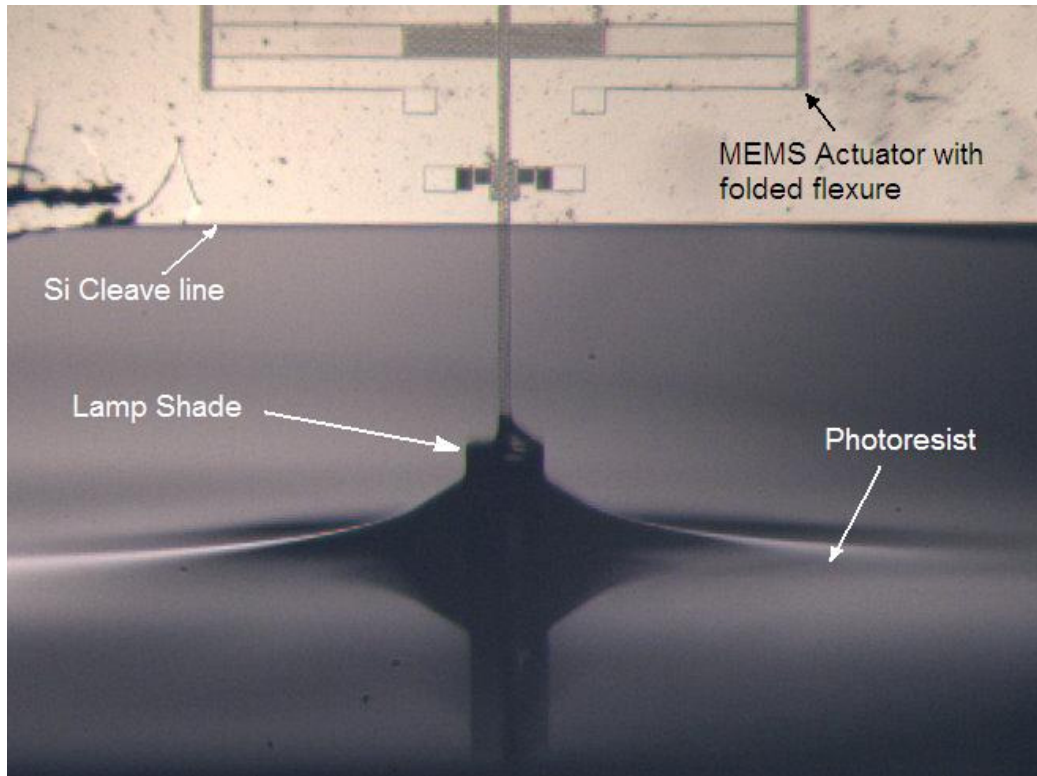


Figure 24: Actuator tip dipped in photoresist droplet

It should be noted at this point that the weight of the member from which the weights hang and the liquids used for attachment never total to greater than 0.1% of the minimum weight hung from the load cell. Therefore, this additional weight can be safely neglected.

Chapter 5

EXPERIMENTAL RESULTS AND DISCUSSION

5.1. Compressive Residual Forces

After the fabrication was completed, physical inspection of the wafer was conducted under the optical microscope. Buckling was observed on almost all of the flexure beams. It is believed that this buckling is due to the compressive residual forces. These residual forces could not have been induced during the device fabrication due to lack of high temperature processing. These forces are believed to be intrinsic to the wafer itself, induced, during its production perhaps during the oxide growth or bonding with the handle layer.

In order to quantify the buckling several strain gauges were purposefully designed on the masks. It was observed that these compressive residual forces vary from location to location on the wafer and hence buckling on the beams depended on the location of the device on the wafer. These strain gauges consisted of fixed-fixed beams of various lengths with a vernier at the center, the point that would be point of inflection after the buckling. It was observed that the deflection on 800 μm beam (the same length as that on the fixed flexure) was approx 1.5 μm near the edges of the wafer and approx 5 μm at the centre of the wafer. Figure 25 below shows the buckled strain gauges at the center of the wafer. In an unbuckled beam both the verniers would have been aligned, the fact they are not means that the residual stress in the wafer increased the critical stress value for the beams and caused buckling. The displacement at the center of the beam is related to the compression by Saif et. al. in [43].

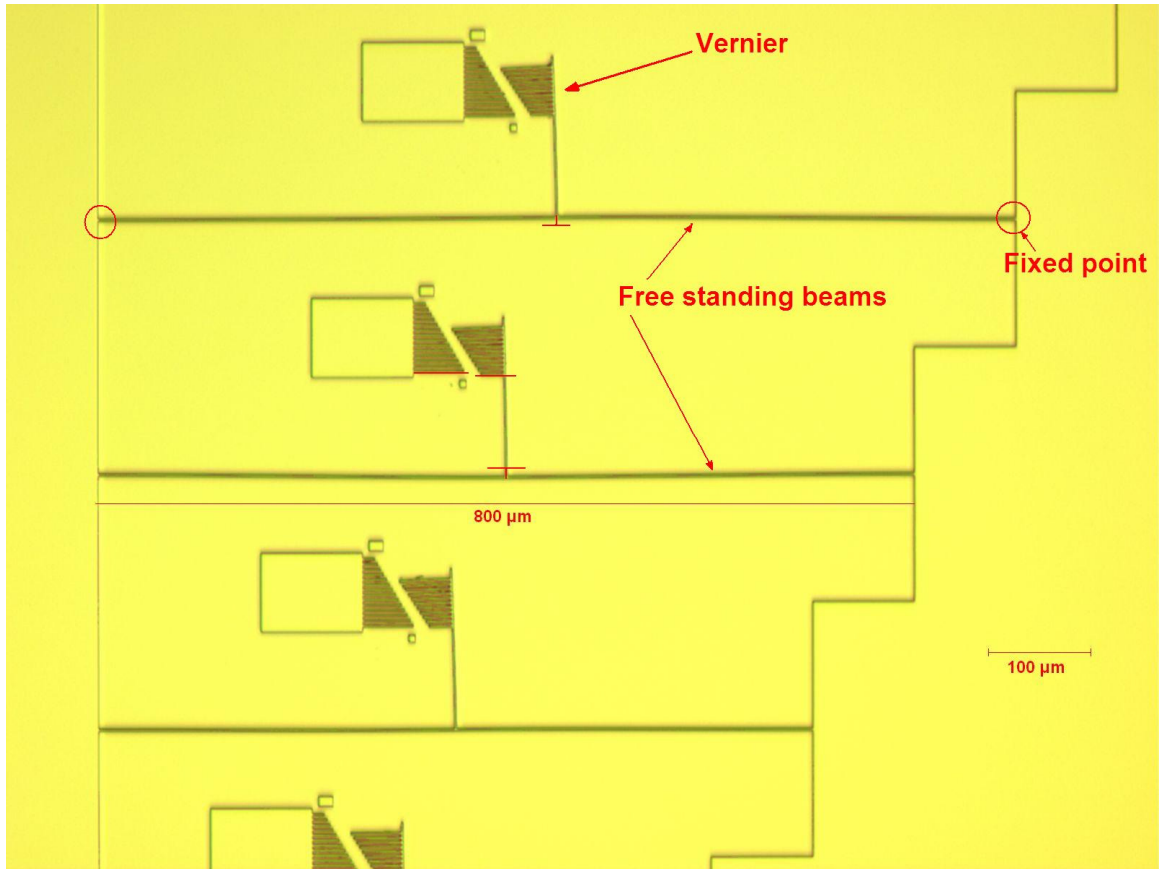


Figure 25: Optical micrograph of the strain gauge at the centre of the wafer

These residual stresses were not accounted for in any of the models and with the beams buckled the actual response is different from what is expected. It was observed that the devices with fixed-fixed flexure and folded flexure were still usable but the effect of compressive residual stresses on the devices with the serpentine flexure was so large that it had rendered the devices unusable.

5.2. Side Instability Voltage

The parameter that is most affected by the existence of the residual forces and buckling is the side instability voltage. The presence of uneven compressive residual forces and the buckled beams generates moments which brings the side

instability voltage down from hundreds of volts to on the order of 10 volts in most cases. The observed value of side instability voltage on the actuators with fixed-fixed flexures is 15-18V, while for the actuators with folded flexure is 5-7V. As the side instability voltage depends on the amount of the compressive residual stresses in the wafer it varies for each kind of actuator depending upon its location on the wafer. This low side instability voltage severely affects the maximum force that can be applied and the maximum allowable comb displacement of the MEMS actuators.

5.3. Calibration

There are number of factors that can affect the response of the actuators. The first source of uncertainty is the dimensional uncertainty. The designed values of the spring and comb finger widths and on the mask is $2 \pm 0.2 \mu\text{m}$, assuming that photolithographic process was meticulously fine tuned and dimensions transferred on the wafer are exactly the same as that on the mask (not the actual case of course!) then the width of the springs in the flexure can be anywhere between $1.8 - 2.2 \mu\text{m}$. Similarly the comb finger gap can be anything between $1.6 - 2.4 \mu\text{m}$. The wafer tolerance on the handle layer thickness was $20 \pm 0.5 \mu\text{m}$, which means that the height of the structure after it has been released could vary between $19.5 - 20.5 \mu\text{m}$.

The second source of uncertainty is the uncertainty in the material properties of the silicon. The value for the Young's Modulus for the Single Crystal Silicon (SCS) varies between $62 - 179 \text{ GPa}$ [56]. The elastic modulus depends on the crystal orientation and type and amount of doping. The moduli expected for these

devices, which correspond to {110} plane varies between 150-170 GPa [57]. These variations in dimensions and physical properties of the silicon lead to uncertainty in the actual response of the actuator.

A general method to deal with the propagation of uncertainties is given by [58]. Suppose if 'R' is function of variable x, y and z with uncertainties:

$$R = f(x, y, z) \quad (31)$$

Then the uncertainty in 'R' due to x alone would be:

$$\Delta_x R = f(x + \Delta x, y, z) - f(x, y, z) \quad (32)$$

Where Δx is the uncertainty in x , similarly the uncertainty in 'R' due to y and z will be:

$$\Delta_y R = f(x, y + \Delta y, z) - f(x, y, z) \quad (33)$$

$$\Delta_z R = f(x, y, z + \Delta z) - f(x, y, z) \quad (34)$$

Therefore the net uncertainty is calculated as a square root of the sum of squares of the individual contributions:

$$\Delta R = \sqrt{(\Delta_x R)^2 + (\Delta_y R)^2 + (\Delta_z R)^2} \quad (35)$$

The formal justification for this statement comes from the theory of statistical distributions and assumes that the distribution of successive variable values is described by the so-called Gaussian distribution. Note that this general method

applies no matter what functional relationship between R and the various variables. It is not restricted to additive and multiplicative relationship as are the usual simple rules for handling uncertainties.

The above uncertainty analysis can be used to calculate the uncertainty in the device response due to the variation in the physical dimensions and material properties of the MEMS device. But there is a third and unpredictable source of uncertainty, the residual stresses in the wafer. These residual stresses induce residual forces in the device and make the response from each device unique. Modeling these residual stresses also presents a challenge. And even if they are accurately modeled, the combined uncertainty of all the three sources of variation will be very large making the accurate prediction of the actuator response impossible.

In order to eliminate this huge uncertainty in the calculated response each MEMS device can be individually calibrated by the method described in the previous chapter. It not only gives a very accurate response (very small uncertainty) for the device but also the calibration method can be traced back to the NIST standards ensuring that the results from different experiments can be compared.

5.3.1. Fixed-fixed flexure

A MEMS actuator with fixed-fixed flexure was calibrated using the method described in the previous chapter. Force vs. Capacitance change was noted. Later, the same device was measured in a SEM. Using the measured

dimensions the capacitive measurements were transformed to the equivalent displacement using equation (21).

$$C = \frac{2n\epsilon_0 t(l_0+l)}{g} \quad (21)$$

Figure 26 gives Force versus displacement curve for the calibrated fixed-fixed flexure.

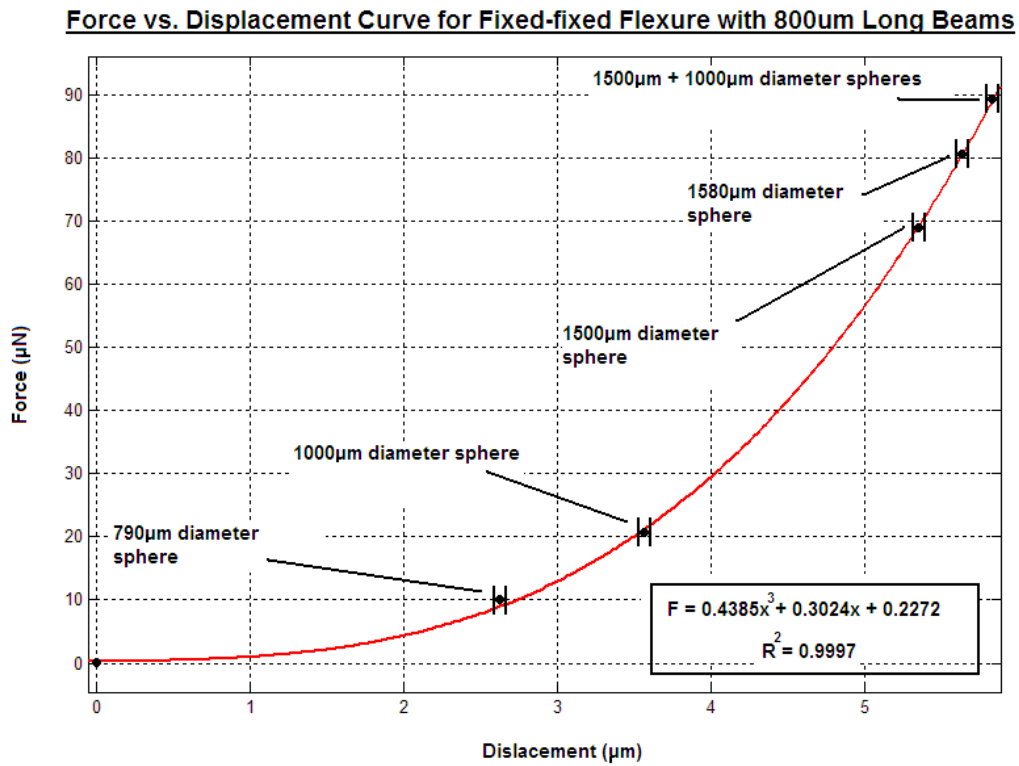


Figure 26: Calibration curve for the fixed-fixed flexure

Curve fit equation and R^2 value for the calibrated device is:

$$F = 0.4385x^3 + 0.3024x + 0.2272$$

$$R^2 = 0.9997$$

The error bars on the displacement (x-axis) are due to the measurement uncertainty and are equal to +/- 100nm. The uncertainty on the force (y-axis) is very small to display on the chart above. Table below gives the uncertainty on force for each diameter sphere. This uncertainty is due to the manufacturing tolerance of +/-2.542 μ m on the diameter of the sphere.

Sphere Diameter (μm)	Force (μN)	Force Uncertainty (μN)
790	10.07	+/- 0.09 μ N
1000	20.42	+/- 0.15 μ N
1500	6.8.92	+/- 0.35 μ N
1580	80.55	+/- 0.38 μ N

Figure 27 shows the uncertainty in the response of the actuator due to the dimensional variations for elastic modulus of 150GPa and 170GPa. The uncertainty increases with higher modulus.

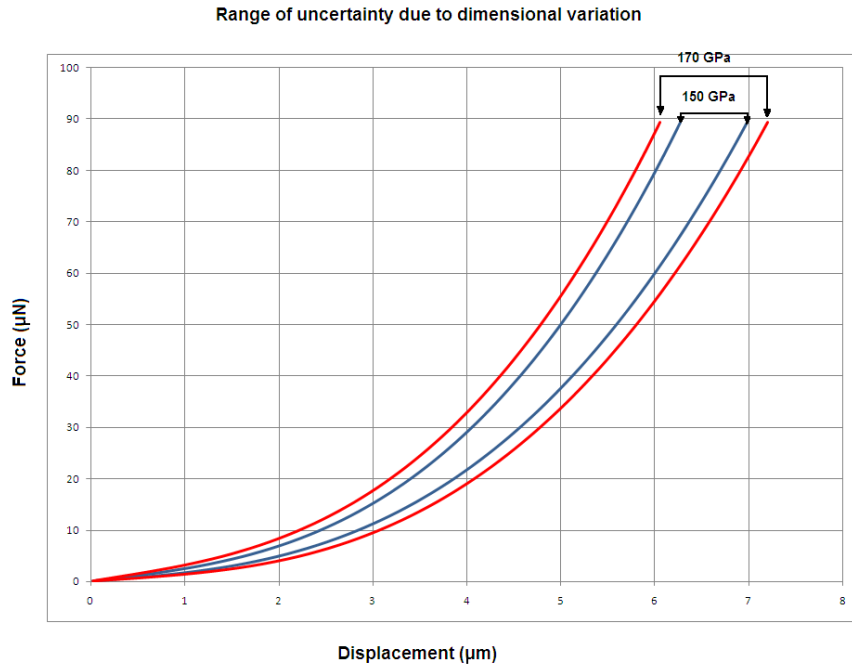


Figure 27: Range of uncertainty in actuator response with elastic modulus 150 – 170 GPa

Comparison between the calibrated response of the MEMS actuator and the modeled uncertainty is shown in Figure 28.

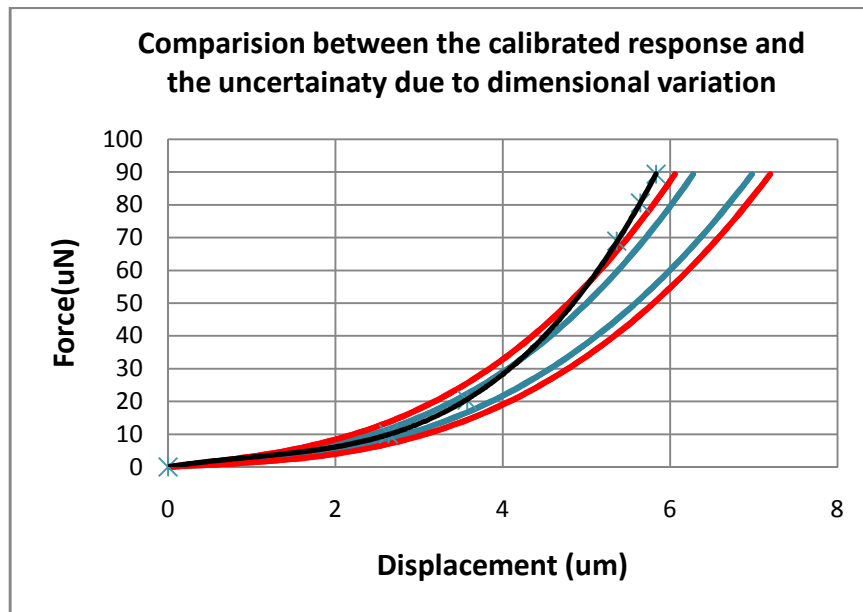


Figure 28: Comparison between the calibrated response and the uncertainty due to dimensional variation of device with fixed-fixed flexure

It can be seen on the curves above that there exist an uncertainty of 1-2 μm at large deflections. Also despite the residual stresses on the wafer the response of the MEMS actuator closely follows the predicted curves for very small deflections. Making this type of the actuator ideal for testing metals where maximum required elongation is less than 0.5 μm .

5.3.2. Folded flexure

A MEMS actuator with folded flexure was also calibrated and the analysis similar to the one described in the section above was performed. Figure 29 gives Force versus displacement curve for the calibrated folded flexure.

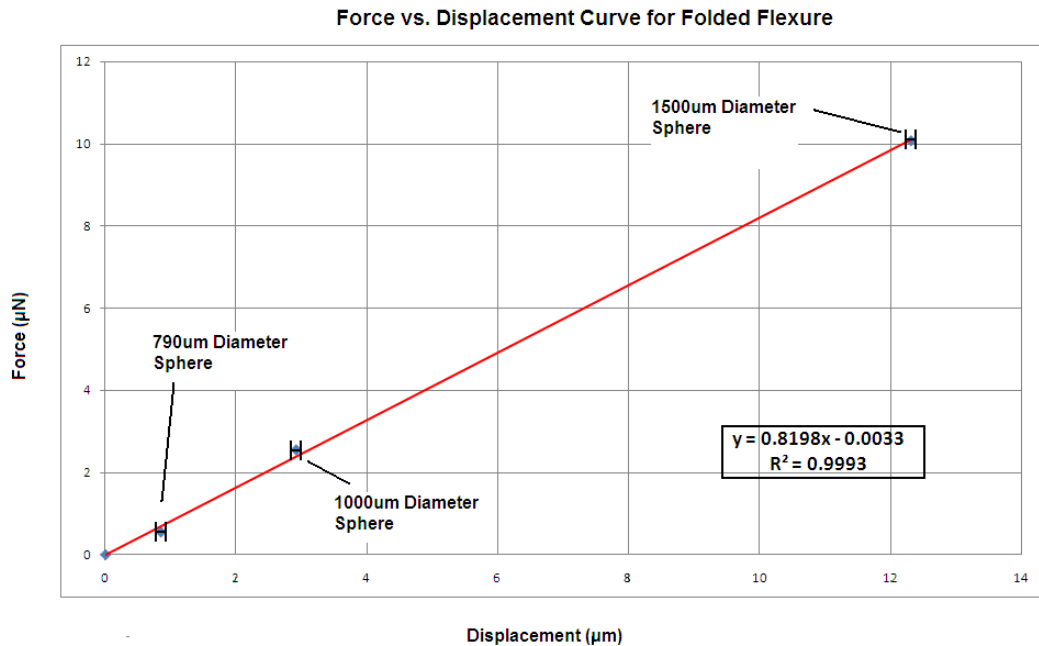


Figure 29: Calibration curve for the folded flexure

Curve fit equation and R^2 value for the calibrated device is:

$$F = 0.8198 x + 0.0033$$

$$R^2 = 0.9993$$

The error bars on the displacement (x-axis) are due to the measurement uncertainty and are equal to +/- 100nm. The uncertainty on the force (y-axis) is very small to display on the chart above. Table below gives the uncertainty on force for each diameter sphere. This uncertainty is due to the manufacturing tolerance of +/-2.542µm on the diameter of the sphere.

Sphere Diameter (µm)	Force (µN)	Force Uncertainty (µN)
300	0.55	+/- 0.01uN
500	2.55	+/- 0.04uN
790	10.07	+/- 0.09uN



Figure 30: Range of uncertainty in actuator response with elastic modulus 150 – 170 GPa

Comparison between the calibrated response of the MEMS actuator and the modeled uncertainty is shown in Figure 31.

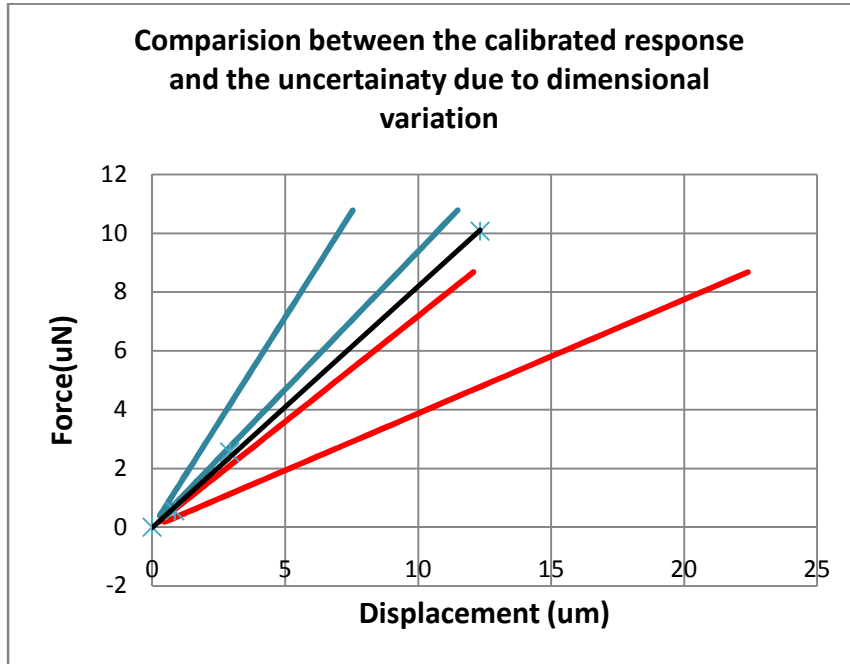


Figure 31: Comparison between the calibrated response and the uncertainty due to dimensional variation of device with folded flexure

It can be seen on the curves above that there exist a huge uncertainty at all deflections. Therefore use of this type of flexure for any kind of testing would give misleading results unless the actuator is calibrated and its response is noted and accounted for prior to testing. This kind of flexure can be used for applications with very large deflections thus making it a good candidate for testing polymers or biological materials.

Chapter 6

CONCLUSION

This thesis gives the detailed account of the design process employed to design, fabricate and calibrate MEMS comb drive actuators that could be used for in-situ materials testing. Since this actuator is processed separately from the test specimen therefore, the processing of the specimen is not dependent on the actuator itself. The reasons have been discussed which make the actual response of the MEMS devices deviate from the modeled response. The presence of residual stresses on the wafer makes the behavior of each device unique. The unique behavior of these devices necessitates their calibration before they could be used for material testing. Three different flexure designs the fixed-fixed, folded and serpentine flexure were fabricated for the purpose of this study. Of the three, the compressive residual stresses on the wafer rendered the devices with the serpentine flexure unusable. A recently developed method of calibration that can be traced back to the NIST standards was employed to calibrate the devices with fixed-fixed and folded flexures [39]. Their actual behavior was compared to their modeled behavior. It has been shown devices with the fixed-fixed flexure can be used for testing materials that do not require large elongation like metals even without calibration. The devices with folded flexure can be used to test the materials that require large elongation like polymers and biological cells. But these devices must be calibrated and their force versus displacement curves must be determined before using them as actuators for materials testing.

6.1. Future Work

The devices have very low side instability voltage. Further study is required to investigate methods through which the devices could be made to operate on voltages up to 40 Volts. Further investigations are also required on methods to measure the capacitance change across the comb finger while a DC bias is applied across them to actuate the device.

Bibliography

- [1] K. E. Petersen, "Silicon as a mechanical material," in *Proceedings of the IEEE*, vol. 70, May 1982, pp. 420-457.
- [2] R. S. Muller, "From IC's to microstructure: materials and technologies," in *IEEE Micro Robots and Teleoperators Workshop*, Hyannis, Mass., Nov. 9-11, 1987.
- [3] M. Mehregany, K. J. Gabriel, and W. S. N. Trimmer, "Integrated fabrication of polysilicon fabrication," *IEEE Trans. Electron Devices*, vol. ED-35, pp. 719-723, 1988.
- [4] T. A. Lober and R. T. Howe, "Surface micromachining processes for electrostatic microactuator fabrication," in *Technical digest, IEEE Solid-State sensors and Actuators Workshop*, Hilton Head Island, SC., June 1988, pp. 59-62.
- [5] J. A. Schweitz, K. Hijrot, and B. Hok, "Bulk and surface micromachining of GaAs structures," in *Technical Digest, IEEE Micro Elctro Mechanical Systems Workshop*, Napa Valley, CA, Feb. 1990, pp. 73-76.
- [6] M. J. Madou, *Fundamentals of Microfabrication: the science of miniturization*, 2nd ed.. Washington, D.C., US: CRC Press LLC, 2002.
- [7] M. T. A. Saif and N. C. MacDonald, "A millinewton microloading device," *Sensors and Actuators A*, vol. 53, pp. 65-75, 1996.
- [8] A. Jazairy and N. C. MacDolnald, "Planar Very High Aspect Ratio Microstructuresfor Large Loading Forces," *Microelectronic Engineering*, vol. 30, pp. 527-530, 1996.
- [9] D. Hah, P. R. Patterson, H. D. Nguyen, H. Toshiyoshi, and M. C. Wu, "Theory and Experiments of Angular Verticle Comb Drive Actuators for Scanning Micrmirrors," *Journal of selected topics in Quantum Electronics*, vol. 10, no. 3, pp. 505-513, May 2004.
- [10] C. S. B. Lee, S. Han, and N. C. MacDonald, "Single Crystal Silicon (SCS) XY-Stage Fabricated by DRIE and IR Allignment," in *The 13th Annual International Conference on Micro Electro Mechanical Systems*, Miyazaki, Japan, Jan 2000, pp. 28-33.
- [11] M. Suster, J. Guo, N. Chaimanonart, W. H. Ko, and D. J. Young, "High Performance MEMS Capacitive Strain sensing System," *Journal of Microelectromechanical Systems*, vol. 15, no. 5, pp. 1069-1077, Oct. 2006.
- [12] W. C. Tang, T. H. Nguyen, and R. T. Howe, "Laterally Driven Polysilicon Resonant Micrstructures," *Sensors and Actuators*, vol. 20, pp. 25-32, 1989.
- [13] W. C. Tang, "Electrostatic Comb Drive for Resonant Sensor and Actuator Applications," PhD Dissertation, Faculty of Electrical Engineering and Computer Sciences, University of California, Berkeley, CA, 1990.
- [14] S. P. Pacheco, L. P. B. Katehi, and C. T. Nguyen, "Design of Low Actuation Voltage RF MEMS Switch," in *IEEE MTT-S International Microwave Symposium*,

- Boston, MA, 2000 , pp. 165-168.
- [15] S. Renard, C. Pisella, J. Collet, V. Gaff, and J. -L. Lauront, "Capacitive pressure and Inertial Sensor by Epi-SOI Surface," in *Proceedings of IEEE Sensors*, 2002, pp. 1385-1388.
- [16] M. Esashi, S. Shoji, and A. Nakano, "Normally Close Microvalve and Micropump fabricated on Silicon Wafer," in *Technical Digest, IEEE Microelectromechanical Systems Workshop*, Salt Lake City, UT, Feb 1989, pp. 29-34.
- [17] H. Jerman, "Electrically Activated Micromachined diaphragm valves," in *Technical Digest, IEEE Solid State Sensors and Actuators Workshop*, Hilton Head Island, SC., Jun 1990, pp. 65-69.
- [18] M. A. Huff, M. S. Mettner, T. A. Lober, and M. A. Schmidt, "A Pressure Balanced Electrostatically Actuated Microvalve," in *Technical Digest, IEEE Solid State Sensors and Actuators Workshop*, Hilton Head Island, SC., Jun 1990, pp. 123-127.
- [19] R. Legtenberg, A. W. Groeneveld, and M. Elwenspoek, "Comb Drive Actuators for Large Displacements," *J. Micromech. Microeng.*, vol. 6, p. 320-329, Jun. 1996.
- [20] Y. H. Cho and P. A. Pisano, "Optimum Structural Design of Micromechanical Crab-Leg Flexures with microfabrication constraints," in *Proceedings of ASME Winter Annual Meeting, DSC 19*, 1990, pp. 31-49.
- [21] V. P. Jaecklin, C. Linder, N. F. de Rooij, and J. M. Moret, "Micromechanical comb actuators with low driving voltage," *J. Micromech. Microeng.*, vol. 2, pp. 250-255, 1992.
- [22] W. Ye, S. Mukherjee, and N. C. MacDonald, "Optimal Shape Design of an Electric Comb Drive in Microelectromechanical Systems," *Journal of Microelectromechanical Systems*, vol. 7, no. 1, pp. 16-26, Mar. 1998.
- [23] J. D. Grade, H. Jerman, and T. W. Kenny, "Design of Large Deflection Electrostatic Actuators," *Journal of Microelectromechanical Systems*, vol. 12, no. 3, pp. 335-343, Jun. 2003.
- [24] T. Hirano, T. Furuhashi, and K. J. Gabriel, "Design, fabrication and operation of submicron gap comb-drive microactuators," *J. Microelectromech. Syst.*, vol. 1, no. 1, pp. 52-59, 1992.
- [25] A. P. Pisano and Y. H. Cho, "Mechanical design issues in laterally driven microstructures," *Sensors and Actuators A: Physical*, vol. 23, no. 1-3, pp. 1060-1064, Apr. 1990.
- [26] M. T. A. Saif and N. C. MacDonald, "Design Considerations for Large MEMS," in *Proceedings of SPIE, Vol 2448*, San Deigo, CA, 1995, pp. 93-104.
- [27] M. T. A. Saif and N. C. MacDonald, "Planarity of Large MEMS," *Journal of Microelectromechanical Systems*, vol. 5, no. 2, pp. 79-97, Jun. 1996.
- [28] J. J. Sniegowski and C. Smith, "An Application of Mechanical Leverage to Microactuation," in *Proceedings of TRANSDUCERS'95 EUROSENSORS IX*, Stockholm, Sweden, June 1995, pp. 364-367.
- [29] W. A. Moussa, H. Ahmad, W. Badawy, and M. Moussa, "Investigating the Reliability of Electrostatic Comb-Drive Actuators Utilized in Microfluidic and Space systems Using Finite Element Analysis," *Canadian Journal of Electrical and*

- Computer Engineering*, vol. 27, no. 4, pp. 195-200, Oct. 2002.
- [30] S. Krylov, N. Moussay, and Y. Bernstein, "Sensitivity Study of Comb-drive Actuator with Folded Suspension," in *Proceedings of 11th International Conference on Fracture*, Turin, Italy, Mar 2005.
- [31] H. Huang and F. Spaepen, "Tensile testing of free standing Cu, Ag and Al thin films and Ag/Cu multilayers," *Acta Materialia*, pp. 3261-3269, 2000.
- [32] A. J. Kalkman, A. H. Verbruggen, and C. A. M. Janssen, "Young's modulus measurement and grain boundary sliding in free standing thin metal films," *Applied Physics Letters*, vol. 78, pp. 2673-2675, 2001.
- [33] R. J. Vinci and J. J. Vlassak, "Mechanical behaviour of thin films," *Annual Review of Material Science*, pp. 431-462, 1996.
- [34] U. Landman, W. D. Luedtke, N. A. Burnham, and R. J. Colton, "Atomistic mechanism and dynamic adhesion, nanoindentation and fracture," *Science, New series*, vol. 248, pp. 454-461, 1990.
- [35] M. A. Haque and B. A. Samuel, "Room temperature relaxation of free standing nanocrystalline gold film," *Journal of micromechanics and microengineering*, vol. 16, pp. 929-934, 2006.
- [36] A. Hadrboletz, B. Weiss, and G. Khatibi, "Fatigue and fracture properties of thin metallic foil," *International Journal of Fatigue*, vol. 109, no. 1, pp. 68-89, 2001.
- [37] Y. Zhu and H. D. Espinosa, "An electro-mechanical material testing system for in situ electron microscopy and applications," *Proceedings of National Academy of Sciences*, vol. 102, no. 41, pp. 14503-14508, Oct. 2005.
- [38] M. A. Haque and M. T. A. Saif, "Microscale materials testing using MEMS actuator," *Journal of Microelectromechanical Systems*, vol. 10, no. 1, pp. 146-152, 2001.
- [39] K. Abbas, Z. C. Leseman, and T. J. Mackin, "A novel method for the calibration of MEMS load cells," *International Journal of Mechanics and Materials in Design*, vol. 4, pp. 383-389, Mar. 2008.
- [40] W. C. Young, *Roark's Formulas for Stress and Strain*, 6th ed.. McGraw Hill, 1989.
- [41] G. K. Fedder, "Simulation of microelectromechanical systems," PhD. Dissertation, Faculty of Electrical Engineering and Computer Sciences, University of California, Berkeley, CA, 1994.
- [42] R. Frisch-Fay, *Flexible Bars*. Ryde, New South wales, Australia: Butterworths & Co. Limited, 1962.
- [43] M. T. A. Saif and N. C. MacDonald, "Measurement of forces and spring constants of microinstruments," *Review of Scientific Instruments*, vol. 60, no. 3, pp. 1410-1422, Mar. 1998.
- [44] M. W. Judy, "Micromechanisms using sidewall beams," PhD Dissertation, Faculty of Electrical and Computer Sciences, University of California, Berkeley, CA, 1994.
- [45] W. C. Tang, M. G. Lim, and R. T. Howe, "Electrostatic comb drive levitation and control method," *J. Microelectromech. Syst.*, vol. 1, pp. 170-178, 1992.
- [46] F. Larmer and A. Schilp, "Method for anisotropically etching silicon," Patent DE4241045, US 5501893, and EP 625285, 1992.

- [47] J. N. Israelachvili and G. E. Adams, "Direct measurement of long range forces between two mica surfaces in aqueous KNO₃ solutions," *Nature (London)*, vol. 262, pp. 774-776, 1976.
- [48] C. A. Helm, W. Knoll, and J. N. Israelachvili, "Measurement of Ligand-Receptor Interactions," in *Proceedings of the National Academy of Sciences of the United States of America*, vol. 88, 1991, pp. 8169-8173.
- [49] Z. C. Leseman and T. J. Mackin, "Determination of the mechanical properties of freestanding nano-thickness gold membranes using a novel MEMS based load cell," *Sensors & Actuators A*, vol. 134, pp. 264-270, 2007.
- [50] J. R. Pratt, D. B. Newell, J. A. Kramar, and E. Whitenon, "Calibration of piezoresistive cantilever force sensors using the NIST electrostatic force balance," in *Proceedings of the IMECE 2003 ASME International Mechanical Engineering Congress, Washing D. C.*, 2003, pp. 289-292.
- [51] J. Rajagopalan, J. Han, and M. T. A. Saif, "Plastic Deformation Recovery in Freestanding Nanocrystalline Aluminum and Gold Thin Films," *Science*, vol. 315, pp. 1831-34, 2007.
- [52] J. R. Davis, *Metals Handbook*, 2nd ed.. ASM International, 1998.
- [53] B. Wu, A. Heidelberg, and J. J. Boland, "Mechanical properties of ultrahigh-strength gold nanowires," *Nature Materials*, 2005.
- [54] H. D. Espinosa, B. C. Prorok, and B. Peng, "Plasticity size effects in free-standing submicron polycrystalline FCC films subjected to pure tension," *Journal of the Mechanics and Physics of Solids*, vol. 52, pp. 667-689, 2004.
- [55] Z. C. Leseman and T. J. Mackin, "Indentation testing of axisymmetric freestanding nanofilms using a MEMS load cell," *Sensors and Actuators A: Physical*, vol. 134, no. 1, pp. 264-270, Feb. 2007.
- [56] B. Bhushan and X. Li, "Micromechanical and tribological characterization of doped single crystal silicon and polysilicon films for microelectromechanical systems," *Journal of Material Research*, vol. 12, no. 1, pp. 54-63, Jan. 1997.
- [57] J. J. Wortman and R. A. Evans, "Young's modulus, Shear modulus and Poisson's Ratio in Silicon and Germanium," *Journal of Applied Physics*, vol. 36, no. 1, pp. 153-156, Jun. 1964.
- [58] J. Taylor, *An Introduction to Uncertainty Analysis*, 2nd ed. Boulder, Colorado: Univ Science Books, 1996.

Appendix 'A'

FABRICATION PROCEDURE

HF Cleaning

<i>Process Step</i>	<i>Tool</i>	<i>Program</i>	<i>Parameters</i>		<i>Comments</i>
<i>BHF Cleaning</i>	Acid Bench		6:1 BOE	60 sec	6 Pts 40% NH ₄ F; 1 Pt 49% HF Acid
<i>QDR</i>	Caustic Bench		5 cycles		
<i>Spin Rinse Dryer</i>	Verteq	Program 1	Resistivity DI water: 15 - 18 mega ohm		
Dehydration Bake	Hot Plate		200° C, 5 min		

Actuator Pattern

<i>Process Step</i>	<i>Tool</i>	<i>Program</i>	<i>Parameters</i>		<i>Comments</i>
<i>HMDS Spin</i>	CEE Coater	Program 4	500 rpm, 5 sec	5000 rpm, 20 s	HMDS single Dispense with repeater setting 3ml
<i>PR Spin</i>	CEE Coater	Program 4	500 rpm, 5 sec	5000 rpm, 20 s	AZ5214 Double Dispense with repeater setting 10ml
<i>Soft Bake</i>	Hot Plate		105° C, 90 s		
<i>Expose</i>	Karl Suss	Hard Contact	Mask: Actuator, Exp: 6 sec		Intensity: @365nm = 5.8mW/cm ² ; @405nm = 11.3mW/cm ²
<i>Develop</i>	Caustic Bench		2min AZ400K; 4:1		with slight agitation
<i>QDR</i>	Caustic Bench		5 cycles		
<i>Spin Rinse Dryer</i>	Verteq	Program 1	Resistivity DI water: 15 - 18 mega ohm		

<i>Inspection</i>	Nikon Microscope			
-------------------	---------------------	--	--	--

DRIE Etch (Device) & Cleaning

Process Step	Tool	Program	Parameters		Comments
<i>DRIE Etch</i>	Adixen DRIE	Std 15 Min Si	1800W, C4F6, SF6	2-3u/min	
<i>Remove PR</i>	Solvent Bench		Acetone, Methano, IPA, N2		
<i>PR Stripping</i>	Acid Bench	15 min	H ₂ SO ₄ +H ₂ O ₂		
<i>QDR</i>	Caustic Bench		5 cycles		
<i>Spin Rinse Dryer</i>	Verteq	Program 1	Resistivity DI water: 15 - 18 mega ohm		
<i>Descumming</i>	March RIE Etcher	Program 1	152 watt; 60 sec	83% O ₂ (Gas 4)	

Backside Photo Lithography

Process Step	Tool	Program	Parameters		Comments
<i>HMDS Spin</i>	CEE Coater	Program 2	500 rpm, 5 s	1000 rpm, 60 s	HMDS single Dispense with repeater setting 3ml
<i>PR Spin</i>	CEE Coater	Program 2	500 rpm, 5 s	1000 rpm, 60 s	AZ9260 Triple Dispense with repeater setting 8ml
<i>Soft Bake</i>	Hot Plate		120° C, 2min		
<i>Expose</i>	Karl Suss	Vacuum Contact	Mask: Backside Etch, Exp: 300 sec		Intensity: @365nm = 5.8mW/cm ² ; @405nm = 11.3mW/cm ²
<i>Develop</i>	Caustic Bench		5 min AZ400K; 3:1		With agitation
<i>QDR</i>	Caustic Bench		5 cycles		

<i>Spin Rinse Dryer</i>	Verteq	Program 1	Resistivity DI water: 15 - 18 mega ohm	
<i>Inspection</i>	Nikon Microscope			

DRIE Etch (Backside)

Process Step	Tool	Program	Parameters		Comments
<i>DRIE Etch</i>	Adixen DRIE	Std 90 Min Si	1800W, C ₄ F ₆ (150 sccm, 3 sec), SF ₆ (300 sccm 7sec)		Pbias (~70W), Valve/pressure (48%/3.8 Pa), He (10mbar), Temp (20oC)
<i>DRIE Etch</i>	Adixen DRIE	Std 30 Min Si	1500W, C ₄ F ₆ (320 sccm, 2 sec), SF ₆ (400 sccm 5sec)		Pbias (90W, 10%-10ms), Valve/pressure (100% / 4 Pa), He (10mBar), Temp (20oC)
<i>Remove PR</i>	Solvent Bench		Acetone, Methanol, IPA, N2		
<i>PR Stripping</i>	Solvent Bench		80° C, 15min	EKC 830	
<i>QDR</i>	Caustic Bench		5 cycles		without sprinklers
<i>Hand Drying</i>					
<i>Dehydration Bake</i>	Hot Plate		180° C, 5 min		
<i>Cool</i>			20 sec		

HF Release

Process Step	Tool	Program	Parameters		Comments
<i>BHF release</i>	Acid Bench		6:1 BOE	20 mins	6 Pts 40% NH ₄ F; 1 Pt 49% HF Acid
<i>QDR</i>	Caustic Bench		5 cycles		without sprinklers
<i>Hand Drying</i>					

Appendix 'B'

MATLAB CODES

```
%{  
  
//-----  
---  
  
          Mathematical model for Comb Drive Actuators  
          with Fixed-Fixed beams of rectangular  
          cross sections  
  
-----  
--//  
  
%}  
  
Close all  
clear all  
clc  
  
% //-----Variable Definitions-----//  
  
n = 600;           %No. of teeth  
OL = 10e-6;       %Intial teeth overlap  
k = 2;           %No. of springs  
L = 400e-6;      %Half Length of Spring  
w = 2e-6;        %Spring Width  
b = 2e-6;        %Tooth width  
d = 2e-6;        %Teeth Spacing  
h = 20e-6;       %Height of structure  
eo = 1.00059 * 8.8541878176e-12; %Dielectric constant  
E = 170e9;       %Young's Modulus  
I = (h*w^3)/12;  %Second Moment of Inertia  
A = w*h;         %Area of Beam  
In_Disp = 0e-006; %Initial Disp due to wafer  
compressive forces  
  
V = 1:0.5:41;    %Generating Voltages  
V = V';  
  
F1 = n*eo*h*(V.^2)/d; %Electrostatic Force  
F = F1/(2*k);      %Force on single spring
```

```

% //-----Linear Deflection Model-----//

Def_Lin = In_Disp + (F)*(L^3)/(12*E*I);

% //-----Non Linear Deflection Model-----//

Const1 = 8*E*I/(L^3); %Equations from "Flexible bars" by R.
Frisch Fay, 1962
Const2 = sqrt((2*I)/A);
for i=1:length(V)
    f = @(u)Const1*Const2*(u.^3).*(1.5-0.5*(tanh(u).^2)-
1.5*(tanh(u)./u).^(-0.5)-(F(i)));
    z(i) = fzero(f,0.3);
end

z = z';

N = E*I*(2*z/L).^2 ;

Def_NLin = In_Disp + 2*Const2*(z-tanh(z)).*(1.5-0.5*(tanh(z).^2)-
1.5*(tanh(z)./z).^(-0.5));

C = (2*n*eo*h*(OL+Def_NLin))/d;

Data(:,1) = V; %Voltage
Data(:,2) = F1/1e-6; %Force
Data(:,3) = Def_Lin/1e-6; %Linear Deflection
Data(:,4) = Def_NLin/1e-6; %Non-linear Deflection
Data(:,5) = C/1e-12; %Capacitance

% //-----Axial Stiffness for Side Instability --
-----//

Pcr = E*I*(pi())^2/(4*(2*L)^2); %Critical Load for Buckling
Roark's Stress Strain Formulas

%Nc = (Pcr*(1 + (Def_NLin/(2*L)))+ 3*(Def_NLin/(2*L)).^2
+(25/2)*(Def_NLin/(2*L)).^3)); %Saif Buckling Paper
Nc = N;

%Delta = (3*(Def_NLin-In_Disp).^2/(5*L).*(1./(1-Nc./Pcr).^2-1));
% Legtenberg Paper
Delta = (3*(Def_NLin).^2/(5*L))*2.* Nc./Pcr;

```

```

%Delta = (pi()* Def_NLin).^2/(4*L) ; %Saif
Buckling Paper
kx = ( k*Nc./Delta ); %Hook's
Law multiplied by k to calculate the total stiffness

% //-----Side Instability due to Voltage
Instability-----//

ky = F1./Def_NLin;

kcr = ((2*n*eo*h/d^3)*(OL + Def_NLin).*(V.^2));

%kx = 200*E*I./(3*L*(Def_NLin).^2);

ysi = -(OL/2)+ d*sqrt(0.5*kx./ky);

Vsi = sqrt((kx.*d^3)./(2*n*eo*h.*(OL + Def_NLin)));

%Data(:,6) = ysi/1e-6; %Side Instability displacement

% //-----Plots-----//

figure
plot(Data(:,1), Data(:,3),Data(:,1), Data(:,4))
legend('Linear Deflection Model','Non-Linear Deflection Model')
title('Fixed-Fixed Beam')
xlabel('Voltage (V)'), ylabel('Deflection (\mum)'),
grid, shg

figure
plot(Data(:,3), Data(:,2),Data(:,4), Data(:,2))
legend('Linear Deflection Model','Non-Linear Deflection Model')
title('Fixed-Fixed Beam')
xlabel('Deflection (\mum)'), ylabel('Force (\muN)')
grid, shg

figure
plot(Data(:,1), Data(:,5))
legend('Non-Linear Deflection Model')
title('Beam Deflection Model')
xlabel('Voltage (V)'), ylabel('Capacitance (pF)'),
grid, shg

figure
plot(Data(:,4), Vsi, Data(:,4), Data(:,1))
legend('Vsi','Non Linear Deflection')
title('Beam Deflection Model')
xlabel('Deflection (\mum)'), ylabel('Voltage (V)'),

```



```

grid, shg

figure
plot(Data(:,1), Data(:,2))
title('Beam Deflection Model')
xlabel('Voltage (\mum)'), ylabel('Force Generated (\muN)')
grid, shg

% //-----Normalized Plot(Legtenberg Paper)-----//

% F2 = (F*L^3)/(E*I*h);
% DN2 = Def_NLin/h;
% D2 = Def_Lin/h;
% figure
% plot(2*F2, DN2, 2*F2 ,D2)
% legend('Non-Linear Deflection Model','Linear Deflection Model')
% title('Beam Deflection Model')
% xlabel('PL^3/EIh'), ylabel('\delta/h'),
% grid, shg

```

```

%{
//-----
---

      Mathematical model for Comb Drive Actuators
      with Fixed-Fixed flexure of rectangular
      cross sections with the sample

-----

--//

%}

Close all
clear all
clc

% //-----Actuator Parameters-----//

n = 6000;           %No. of teeth
OL = 10e-6;        %Intial teeth overlap
kn = 2;            %No. of springs
w = 2e-6;          %Spring Width
b = 2e-6;          %Tooth width
d = 2e-6;          %Teeth Spacing
eo = 8.9062386e-12; %Dielectric constant
L = 400e-6;        %Length of Spring
h = 20e-6;         %Height of structure
E = 170e9;         %Young's Modulus
I = (h*w^3)/12;    %Second Moment of Inertia
A = w*h;           %Area of Beam

% //-----Sample Parameters-----//

ws = 2e-6;         %Sample width
hs = 500e-9;       %Sample thickness
Ls = 450e-6;       %Sample length
As = ws*hs;        %X sec area of sample
Es = 78e9;         %Young's Modulus of sample
Strain_elas = 0.10 ; %required Elastic strain in percentage

D_elas_max = Strain_elas*Ls/100; %Max Elastic Deflection for sample

% //-----Generationg Deflection-----//

j=0;
for i=0.1e-9:.05e-9:D_elas_max
    j=j+1;
    Data(j,1) = i; %Deflection

```

```

end
[m,g] = size(Data);

% //-----Sample Calculations-----//

F_Sam = Es*As*Data(:,1)/Ls;           %Elastic Force on sample

% //-----Actuator Calculations-----//

Const1 = 8*E*I/(L^3);                 %Equations from "Flexible bars" by R.
Frisch Fay, 1962
Const2 = sqrt((2*I)/A);
for k=1:1:m

    f = @(z) (2*Const2*(z-tanh(z)).*(1.5-0.5*(tanh(z).^2)-
1.5*(tanh(z)./z)).^(-0.5))-Data(k,1);
    u(k) = fzero(f,1);

end

u = u';

F_Act = Const1*Const2*(u.^3).*(1.5-0.5*(tanh(u).^2)-
1.5*(tanh(u)./u)).^(-0.5);

N = E*I*(2*u/L).^2;

% //-----Total Force-----//

Data(:,2) = 2*kn*F_Act + F_Sam;       %Total Force required

Data(:,3) = sqrt(Data(:,2)*d/(n*eo*b)); %Voltage required to
generate the force

Data(:,4) = 2*n*eo*b*(OL+Data(:,1))/d; %Capacitance

Def_NLin = Data(:,1);

Stress_sam = F_Sam/As;

Strain_sam = Data(:,1)./Ls;

% //-----Axial Stiffness for Side Instability --
-----//

Pcr = E*I*(pi())^2/(4*(2*L)^2);      %Critical Load for Buckling
Roark's Stress Strain Formulas

```

```

Nc = N;    %Legtenberg Paper

Delta = (3*(Def_NLin).^2/(5*L))*2.* Nc./Pcr;           %Derivation
similar to Legtenberg Paper

kx = ( k*Nc./Delta );                                %Hook's
Law multiplied by k to calculate the total stiffness
                                                %Hook's Law multiplied by k to calculate
the total stiffness

% //-----Side Instability due to Voltage
Instability-----//

ky = Data(:,2)./Def_NLin;

kcr = ((2*n*eo*h/d^3)*(OL + Def_NLin).*(Data(:,3).^2));

ysi = -(OL/2)+ d*sqrt(0.5*kx./ky);

Vsi = sqrt((kx.*d^3)./(2*n*eo*h.*(OL + Def_NLin)));

% //-----Plots-----//

figure
plot(Data(:,3), Data(:,1)/1e-6)
title('Beam Deflection Model')
xlabel('Voltage (V)'), ylabel('Deflection (\mum)'),
grid, shg

figure
plot(Data(:,1)/1e-6, Data(:,2)/1e-6)
legend('Linear Deflection Model')
title('Beam Deflection Model')
xlabel('Deflection (\mum)'), ylabel('Force (\muN)')
grid, shg

figure
plot(Data(:,3), Data(:,4)/1e-12)
legend('Non-Linear Deflection Model')
title('Beam Deflection Model')
xlabel('Voltage (V)'), ylabel('Capacitance (pF)'),
grid, shg

figure
plot(Data(:,1)/1e-6, Vsi, Data(:,1)/1e-6, Data(:,3))
legend('Vsi', 'Non Linear Deflection')
title('Beam Deflection Model')
xlabel('Deflection (\mum)'), ylabel('Voltage (V)'),
grid, shg

figure

```

```

plot(Data(:,1), Data(:,2)/1e-6)
title('Beam Deflection Model')
xlabel('Displacement (\mum)'), ylabel('Force Required (\muN)'),
grid, shg

figure
plot(Data(:,3), Stress_sam/1e6)
title('Gold Stress Strain Curve')
xlabel('Voltage (V)'), ylabel('Stress (MPa)'),
grid, shg

% //-----Normalized Plot(Legtenberg Paper)-----//

% F2 = (F*L^3)/(E*I*h);
% DN2 = Def_NLin/h;
% D2 = Def_Lin/h;
% figure
% plot(2*F2, DN2, 2*F2 ,D2)
% legend('Non-Linear Deflection Model','Linear Deflection Model')
% title('Beam Deflection Model')
% xlabel('PL^3/EIh'), ylabel('\delta/h'),
% grid, shg

```

```

%{
//-----
---

                Mathematical model for Comb Drive Actuators
                with Folded Flexure of rectangular
                cross sections

-----

--//

%}

Close all
clear all
clc

% //-----Variable Definitions-----//

n = 2000;                %No. of teeth
OL = 10e-6;             %Intial teeth overlap
kn = 2;                 %No. of flexures
Lb = 600e-6;            %Length of Beam
Lt = 100e-6;           %Length of Truss
w = 2e-6;               %Spring Width
b = 2e-6;               %Tooth width
d = 2e-6;               %Teeth Spacing
h = 20e-6;              %Height of structure
eo = 1.00059 * 8.8541878176e-12; %Dielectric constant
E = 170e9;               %Young's Modulus
Izb = (h*w^3)/12;       %Second Moment of Inertia beam
around z- axis
Izt = (h*Lt^3)/12;     %Second Moment of Inertia truss
around z- axis
A = w*h;                %Area of Beam
In_Disp = 0e-006;      % Initial Disp due to wafer
compressive forces

V = 1:.1:20;           %Generating Voltages
V = V';

F1 = n*eo*h*(V.^2)/d;  %Electrostatic Force
F = F1/(kn);           %Force on single Flexure

% //-----Linear Deflection Model-----//

Def_Lin = (F1)*(Lb^3)/(kn*4*12*E*Izb);

```

```

%-----Calculated Variables-----

L = Lt/Lb;

a = Izt/Izb;

ky = kn* ((24*E*Izb/Lb^3)*((L^2+14*L*a+36*a^2)/(4*L^2+41*L*a+36*a^2)));

kx_max = kn* (24*E*Izt/Lt^3)*((8*L^2+8*L*a+a^2)/(4*L^2+10*L*a+5*a^2));

Disp_y = F1./ky;

C = 2*n*eo*h*(OL+Disp_y)/d;

kx = kn*200*E*Izb./(3*Lb*Disp_y.^2);

ysi = -(OL/2)+ d*sqrt(0.5*kx./ky);

Vsi = sqrt((kx.*d^3)./(2*n*eo*h.*(OL + Disp_y)));

% //-----Plots-----//

Data(:,1) = V; %Voltage
Data(:,2) = F1/1e-6; %Force
Data(:,3) = Disp_y/1e-6; %Deflection in y direction
Data(:,4) = C/1e-12; %Capacitance
Data(:,5) = Vsi; %Side Instability voltage

figure
plot(Data(:,1), Data(:,3))
title('Beam Deflection Model')
xlabel('Voltage (V)'), ylabel('Deflection (\mum)'),
grid, shg

figure
plot(Data(:,1), Data(:,4))
legend('Non-Linear Deflection Model')
title('Beam Deflection Model')
xlabel('Voltage (V)'), ylabel('Capacitance (pF)'),
grid, shg

figure
plot(Data(:,3), Vsi , Data(:,3), Data(:,1))
legend('Vsi', 'Non Linear Deflection')
title('Beam Deflection Model')
xlabel('Deflection (\mum)'), ylabel('Voltage (V)'),
grid, shg

figure
plot(Data(:,1), Data(:,2))

```

```
title('Beam Deflection Model')
xlabel('Voltage (V)'), ylabel('Force (\muN)'),
grid, shg

figure
plot(Def_Lin/1e-6, F1/1e-6,Disp_y/1e-6, F1/1e-6)
legend('Linear Deflection Model','Folded flexure Deflection Model')
title('Folded Flexure')
xlabel('Deflection (\mu m)'), ylabel('Force (\mu N)')
grid, shg
```



```

%{
//-----
---

                Mathematical model for Comb Drive Actuators
                with Folded Flexure of rectangular
                cross sections with Gold Specimen

-----

--//

%}

Close all
clear all
clc

% //-----Variable Definitions-----//

n = 2000;                %No. of teeth
OL = 10e-6;             %Intial teeth overlap
kn = 2;                 %No. of flexures
Lb = 600e-6;            %Length of Beam
Lt = 100e-6;            %Length of Truss
w = 2e-6;               %Spring Width
b = 2e-6;               %Tooth width
d = 2e-6;               %Teeth Spacing
h = 20e-6;              %Height of structure
eo = 1.00059 * 8.8541878176e-12; %Dielectric constant
E = 170e9;              %Young's Modulus
Izb = (h*w^3)/12;       %Second Moment of Inertia beam
around z- axis
Izt = (h*Lt^3)/12;      %Second Moment of Inertia truss
around z- axis
A = w*h;                %Area of Beam
In_Disp = 0e-006;       % Initial Disp due to wafer
compressive forces

% //-----Sample Parameters-----//

ws = 2e-6;              %Sample width6
hs = 500e-9;            %Sample thickness
Ls = 450e-6;            %Sample length
As = ws*hs;             %X sec area of sample
Es = 78e9;              %Young's Modulus of sample
ks = As*Es/Ls;         %Stiffness of the Sample

V = 1:.5:25;           %Generating Voltages
V = V';

```

```

F1 = n*eo*h*(V.^2)/d;           %Electrostatic Force
F = F1/(kn);                   %Force on single spring

%-----Calculated Variables-----

L = Lt/Lb;

a = Izt/Izb;

ky = kn* (24*E*Izb/Lb^3)*((L^2+14*L*a+36*a^2)/(4*L^2+41*L*a+36*a^2)) +
ks;

kx_max = kn* (24*E*Izt/Lt^3)*((8*L^2+8*L*a+a^2)/(4*L^2+10*L*a+5*a^2));

Disp_y = F1./ky;

F_Sam = ks*Disp_y;

C = 2*n*eo*h*(OL+Disp_y)/d;

kx = kn*200*E*Izb./(3*Lb*Disp_y.^2);

ysi = -(OL/2)+ d*sqrt(0.5*kx./ky);

Vsi = sqrt((kx.*d^3)./(2*n*eo*h.*(OL + Disp_y)));

Stress_sam = F_Sam/As;         %Stress on Sample

% //-----Plots-----//

Data(:,1) = V;                 %Voltage
Data(:,2) = F1/1e-6;           %Force
Data(:,3) = Disp_y/1e-6;       %Linear Deflection in y direction
Data(:,4) = C/1e-12;           %Capacitance
Data(:,5) = Vsi;               %Side Instability voltage

figure
plot(Data(:,1), Data(:,3))
title('Beam Deflection Model')
xlabel('Voltage (V)'), ylabel('Deflection (\mum)'),
grid, shg

figure
plot(Data(:,1), Data(:,4))
legend('Non-Linear Deflection Model')
title('Beam Deflection Model')
xlabel('Voltage (V)'), ylabel('Capacitance (pF)'),
grid, shg

```

```
figure
plot(Data(:,3),Vsi , Data(:,3),Data(:,1))
legend('Vsi','Non Linear Deflection')
title('Beam Deflection Model')
xlabel('Deflection (\mum)'), ylabel('Voltage (V)'),
grid, shg
```

```
figure
plot(V, Stress_sam/1e6)
title('Gold Stress Strain Curve')
xlabel('Voltage (V)'), ylabel('Stress (MPa)'),
grid, shg
```

```

%{
//-----
---

                Mathematical model for Comb Drive Actuators
                with Serpentine flexure of rectangular
                cross sections

-----

--//

%}

Close all
clear all
clc

% //-----Variable Definitions-----//

n = 600;                %No. of teeth
OL = 10e-6;            %Intial teeth overlap
kn = 1;                %No. of flexure consiting of 4
springs
a = 20e-6;             %Length of Connector Beam
s = 20e-6;             %Length of Span Beam
j = 20;                %No. of Connector Beams on each
side of the backbone
w = 2e-6;              %Spring Width
b = 2e-6;              %Tooth width
d = 2e-6;              %Teeth Spacing
h = 20e-6;             %Height of structure
eo = 1.00059 * 8.8541878176e-12; %Dielectric constant
E = 170e9;             %Young's Modulus
Izs = (h*w^3)/12;     %Second Moment of Inertia beam
around z- axis
Iza = (h*w^3)/12;     %Second Moment of Inertia beam
around z- axis
A = w*h;              %Area of Beam
In_Disp = 0e-006;     % Initial Disp due to wafer
compressive forces
L= a*j;

V = 1:.5:25;          %Generating Voltages
V = V';

F1 = n*eo*h*(V.^2)/d; %Electrostatic Force
F = F1/(kn);          %Force on single spring

% //-----Linear Deflection Model-----//

Def_Lin = In_Disp + (F)*(L^3)/(2*12*E*Iza);

```

```

%-----Calculated Variables-----

%Stiffness calculations are based on the equations from G. K. Fedder's
PhD
%Dissertaion, UC Berkley 1994

a1 = a* Izs/Iza;

ky = (48*E*Izs*(j*(3*a1+s)-s))/(a^2*j*((3*a1^2+4*a*s+s^2)*j^3-
2*s*(5*a1+2*s)*j^2+(5*s^2+6*a*s-9*a1^2)*j-2*s^2));

kx = (48*E*Izs*((a1+s)*j^2-3*s*j+2*s))/(s^2*((3*a1^2+4*a1*s+s^2)*j^3-
2*s*(5*a1+2*s)*j^2+(5*s^2+6*a1*s-9*a1^2)*j-2*s^2));

Disp_y = F1./ky;          %Hook's Law

C = 2*n*eo*h*(OL+Disp_y)/d;

ysi = -(OL/2)+ d*sqrt(0.5*kx./ky);

Vsi = sqrt((kx.*d^3)./(2*n*eo*h.*(OL + Disp_y)));

% //-----Plots-----//

Data(:,1) = V;           %Voltage
Data(:,2) = F1/1e-6;     %Force
Data(:,3) = Disp_y/1e-6; %Linear Deflection in y direction
Data(:,4) = C/1e-12;    %Capacitance
Data(:,5) = Vsi;        %Side Instability voltage

figure
plot(Data(:,1), Data(:,3))
title('Beam Deflection Model')
xlabel('Voltage (V)'), ylabel('Deflection (\mum)'),
grid, shg

figure
plot(Data(:,1), Data(:,4))
legend('Non-Linear Deflection Model')
title('Beam Deflection Model')
xlabel('Voltage (V)'), ylabel('Capacitance (pF)'),
grid, shg

figure
plot(Data(:,3), Vsi , Data(:,3), Data(:,1))
legend('Vsi', 'Non Linear Deflection')
title('Beam Deflection Model')
xlabel('Deflection (\mum)'), ylabel('Voltage (V)'),

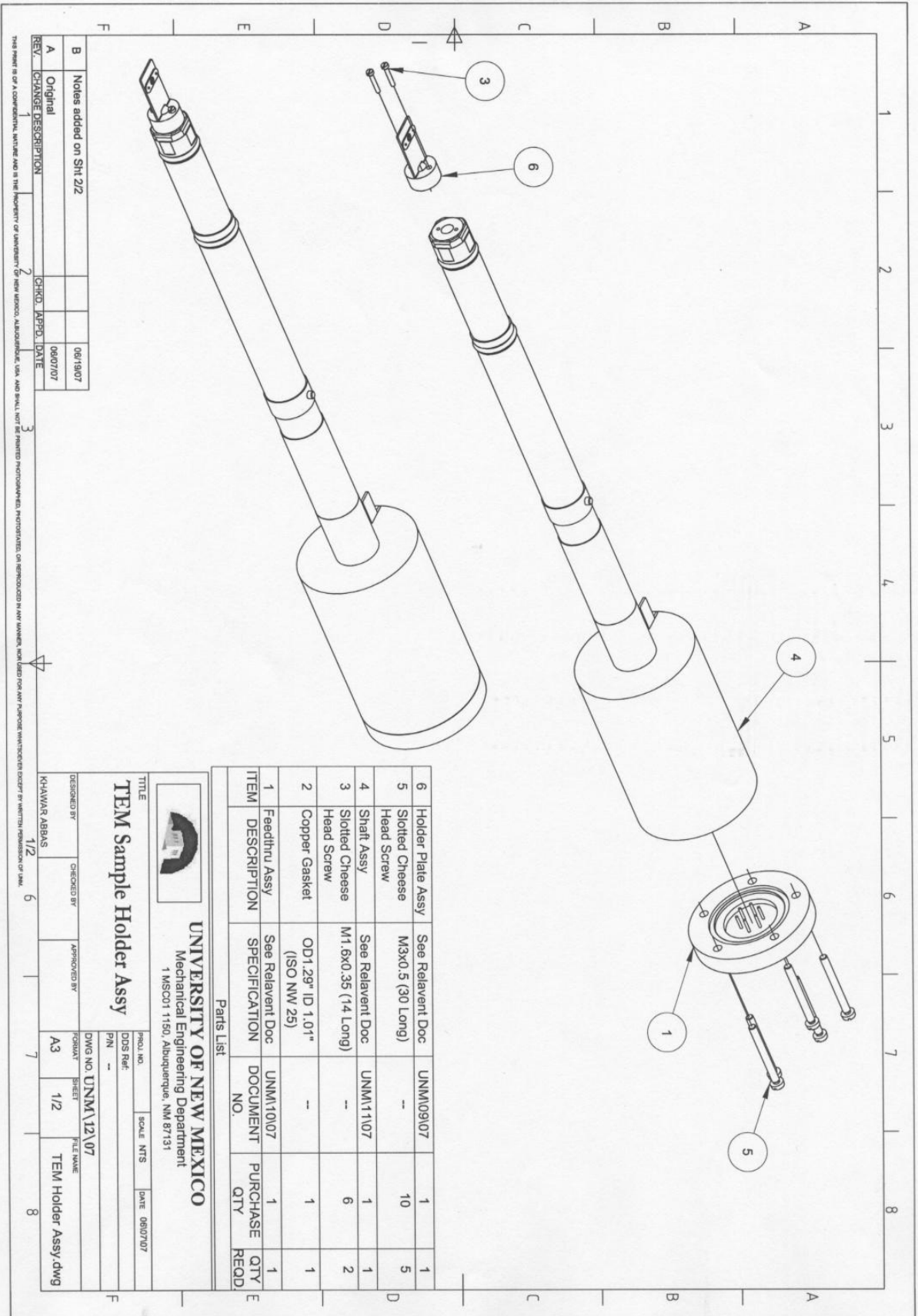
```

```
grid, shg

figure
plot(Def_Lin/1e-6, F1/1e-6, Disp_y/1e-6, F1/1e-6)
legend('Linear Deflection Model', 'Serpentine flexure Deflection Model')
title('Serpentine Flexure')
xlabel('Deflection (\mum)'), ylabel('Force (\muN)')
grid, shg
```

Appendix 'C'

TEM HOLDER DESIGN DRAWINGS



REV.	CHANGE DESCRIPTION	CHKD.	APPR.	DATE
A	Original			06/19/07
B	Notes added on Sht 2/2			06/07/07

THIS PRINT IS A CONFIDENTIAL, UNLAWFUL AND IN THE PROPERTY OF UNIVERSITY OF NEW MEXICO, ALBUQUERQUE, USA, AND SHALL NOT BE REPRODUCED, PHOTOGRAPHED, OR REPRODUCED IN ANY MANNER, WITH OR WITHOUT PERMISSION OF THE UNIVERSITY OF NEW MEXICO.

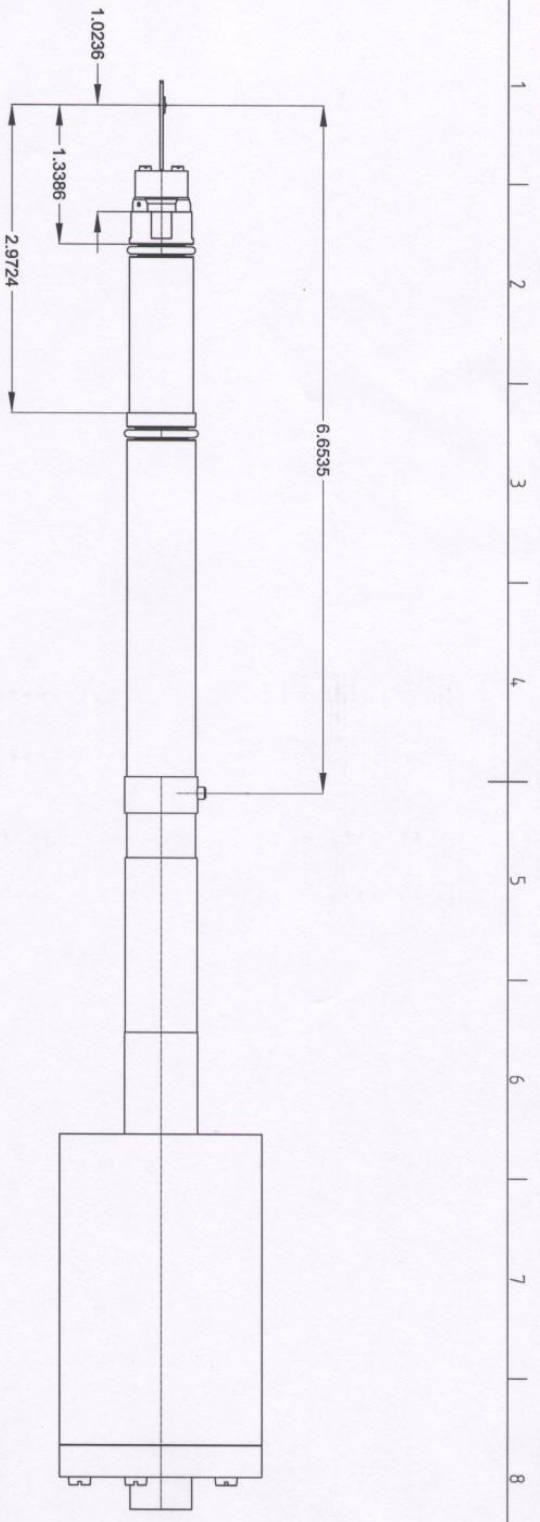
ITEM NO.	DESCRIPTION	SPECIFICATION	DOCUMENT NO.	PURCHASE QTY	QTY RECD.
1	Feedthru Assy	See Relevant Doc	UNM110107	1	1
2	Copper Gasket	OD1.29" ID 1.01" (ISO NW 25)	--	1	1
3	Slotted Cheese Head Screw	M1.6x0.35 (14 Long)	UNM11107	6	2
4	Holder Plate Assy	See Relevant Doc	UNM110107	1	1
5	Slotted Cheese Head Screw	M3x0.5 (30 Long)	--	10	5
6	Shaft Assy	See Relevant Doc	UNM11107	1	1



UNIVERSITY OF NEW MEXICO
 Mechanical Engineering Department
 1 MSC01 1150, Albuquerque, NM 87131

TEM Sample Holder Assy

DESIGNED BY	CHKD BY	APPROVED BY	DWG NO.	UNM\12\07
KHANWAR, ABBAS	1/2	6	FORMAT	SHEET
			A3	1/2
				FILE NAME
				TEM Holder Assy.dwg
				8



- NOTES:**
1. GENERAL LINEAR TOLERANCE ± 0.01 INCH UNLESS STATED OTHERWISE.
 2. ALL DIMENSIONS IN INCHES UNLESS STATED OTHERWISE.

REV.	CHANGE DESCRIPTION	CHNG.	APPD.	DATE
B	Notes added on Sht 2/2			06/19/07
A	Original			06/07/07

UNIVERSITY OF NEW MEXICO
 Mechanical Engineering Department
 1 MSCOT 1150, Albuquerque, NM 87131

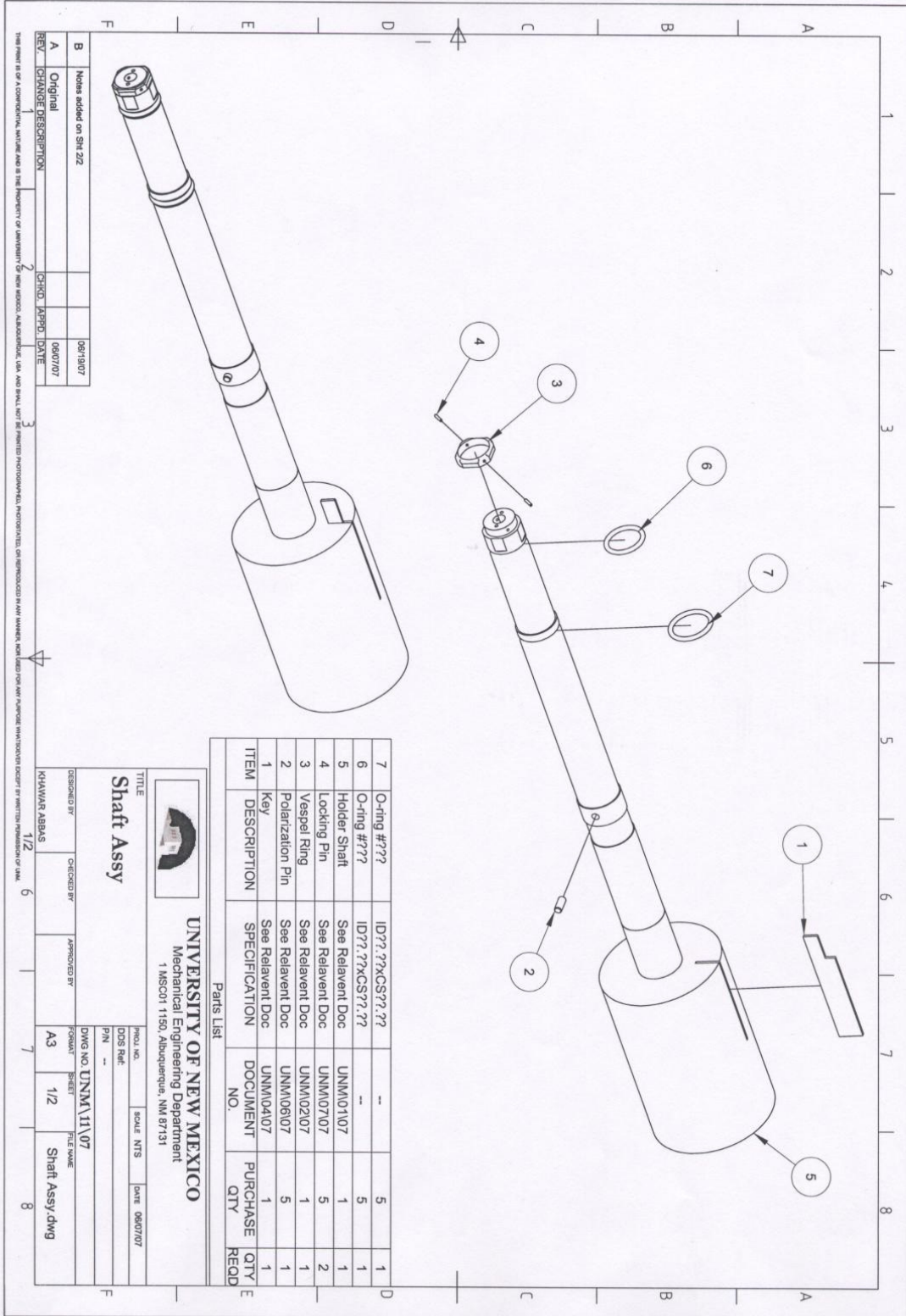
TEM Sample Holder Assy

DESIGNED BY: KHAWAR ABBAS
 CHECKED BY: _____
 APPROVED BY: _____

PROJ. NO. _____ SCALE: NTS
 DCS Ref: _____ DATE: 06/07/07
 PIN: _____

DWG. NO. UNM\12\07
 FORMAT: SHEET
 SHEET: 2/2 FILE NAME: TEM Holder.dwg

THIS PRINT IS A CONFIDENTIAL INSTRUMENT AND IS THE PROPERTY OF UNIVERSITY OF NEW MEXICO. ALBUQUERQUE, N.M. AND SHALL NOT BE REPRODUCED, PHOTOGRAPHED, REPRODUCED IN ANY MANNER, NOR LOANED FOR ANY PURPOSE WITHOUT THE WRITTEN PERMISSION OF UAM.



ITEM	DESCRIPTION	SPECIFICATION	DOCUMENT NO.	PURCHASE QTY	QTY RECD
7	O-ring #???	ID??,??XCS??,??	--	5	1
6	O-ring #???	ID??,??XCS??,??	--	5	1
5	Holder Shaft	See Relavent Doc	UNNM01107	1	1
4	Locking Pin	See Relavent Doc	UNNM0707	5	2
3	Vespel Ring	See Relavent Doc	UNNM02107	1	1
2	Polarization Pin	See Relavent Doc	UNNM06107	5	1
1	Key	See Relavent Doc	UNNM04107	1	1



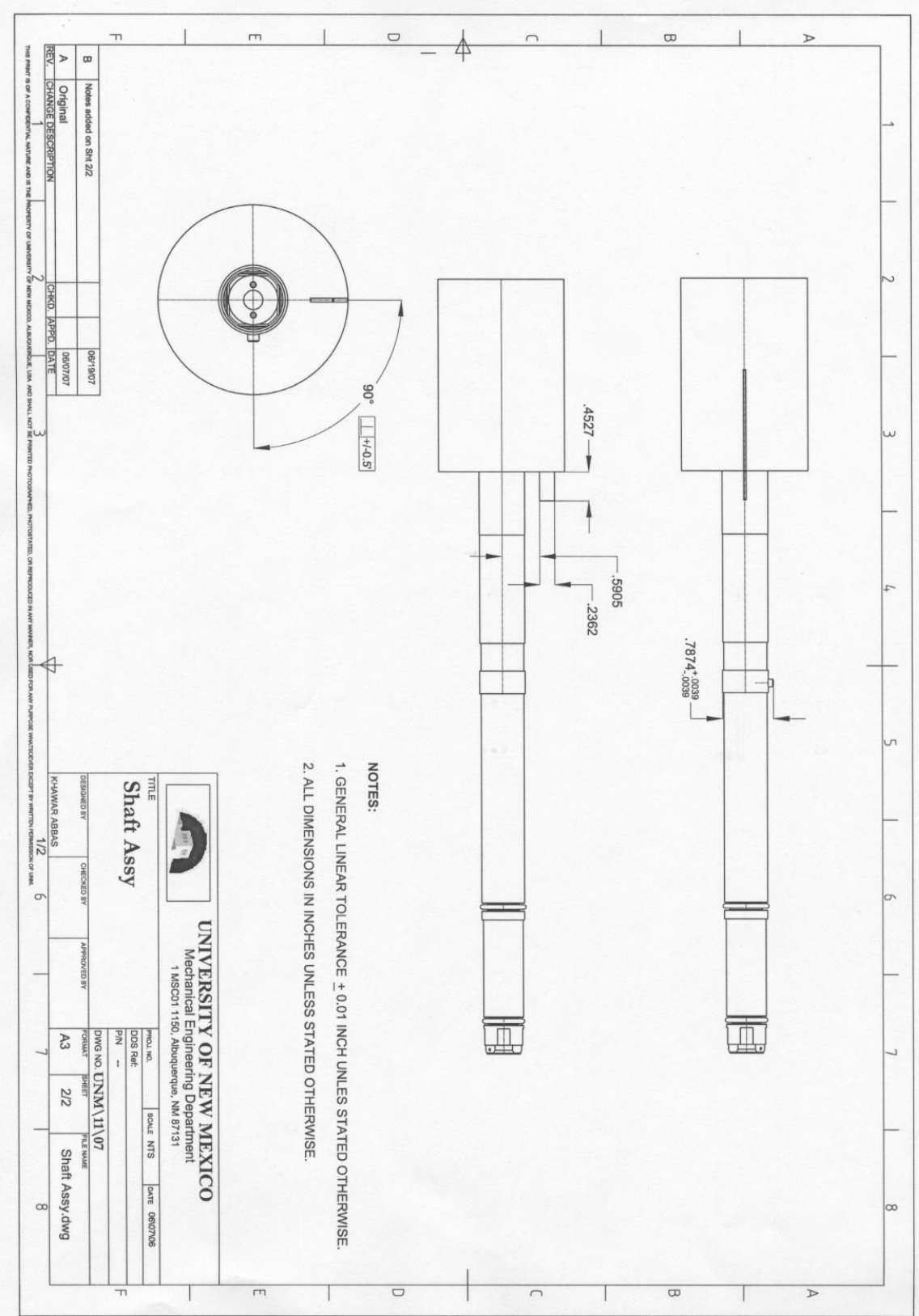
UNIVERSITY OF NEW MEXICO
 Mechanical Engineering Department
 1 MSC01 1150, Albuquerque, NM 87131

Shaft Assy

DESIGNED BY: KHAWAR ABBAS
 CHECKED BY: 1/2
 APPROVED BY: 6
 DWG NO: UNNM\11\07
 P/N: --
 SCALE: NTS
 DATE: 06/07/07
 SHEET: 1/2
 FILE NAME: Shaft Assy.dwg
 7 8

REV.	CHANGE DESCRIPTION	CHD.	APPR.	DATE
B	Notes added on Sh 22			06/19/07
A	Original			06/07/07

THIS DRAWING IS A CONFIDENTIAL ARTICLE AND IS THE PROPERTY OF UNIVERSITY OF NEW MEXICO. ALL RIGHTS RESERVED. USA AND SHALL NOT BE REPRODUCED, REPRODUCED, OR REPRODUCED IN ANY MANNER AND USED FOR ANY PURPOSE WITHOUT THE WRITTEN PERMISSION OF U.M.



REV.	CHANGE DESCRIPTION	CHKD.	APPD.	DATE
B	Notes added on SH-212			06/19/07
A	Original			06/07/07

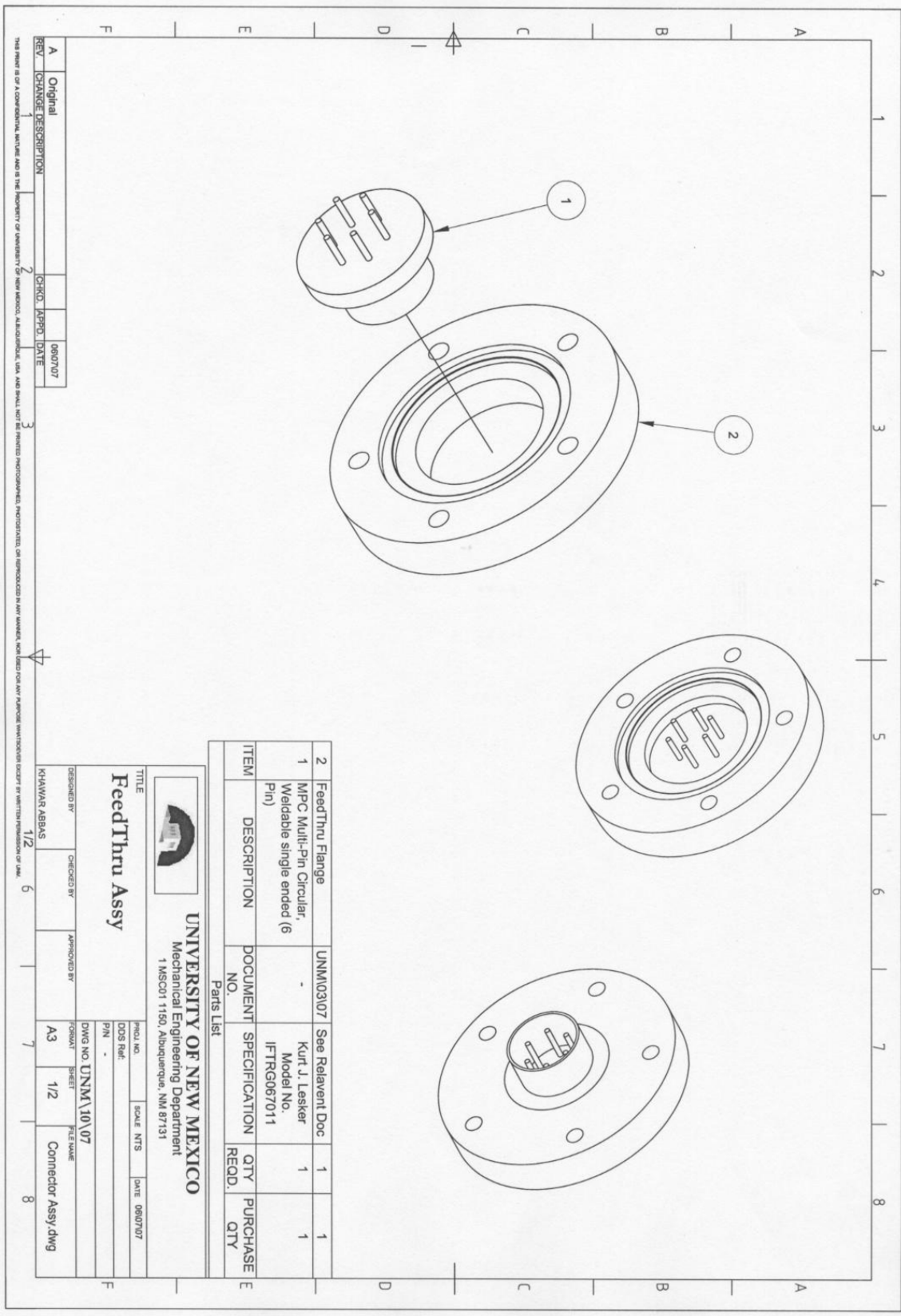
UNIVERSITY OF NEW MEXICO
 Mechanical Engineering Department
 1 MSC01 1150, Albuquerque, NM 87131

Shaft Assy

DESIGNED BY: KRIVAKAR ABBAS
 CHECKED BY: 1/2
 APPROVED BY: 6

PROJ. NO. SCALE: NTS DATE: 06/07/06
 DCS REF. P/N --
 DWG NO. UNM \1\07
 FORMAT: A3 SHEET: 2/2 FILE NAME: Shaft Assy.dwg

THIS PRINT IS OF A CONFIDENTIAL NATURE AND IS THE PROPERTY OF UNIVERSITY OF NEW MEXICO. REPRODUCTION, DISTRIBUTION, OR REMOVAL FROM ANY MANNER, FOR USE FOR ANY PURPOSE WHATSOEVER WITHOUT WRITTEN PERMISSION OF UNM.



REV.	CHANGE DESCRIPTION	CHNO.	APPD.	DATE
A	Original			08/07/07
2				

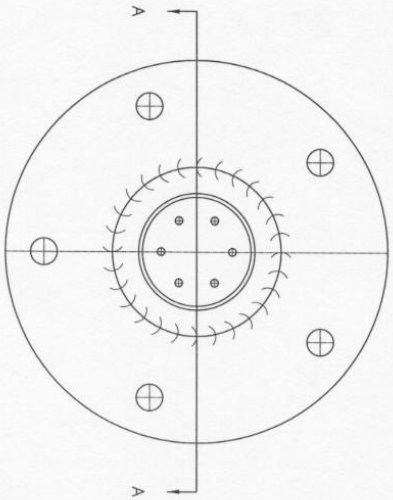
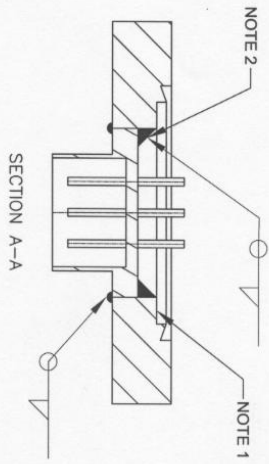
DESIGNED BY	CHECKED BY	APPROVED BY	FORMAN	SHEET	FILE NAME
KHAWAR ABBAS			A3	1/2	Connector Assy.dwg

UNIVERSITY OF NEW MEXICO
 Mechanical Engineering Department
 1 MSC01 1150, Albuquerque, NM 87131

ITEM NO.	DESCRIPTION	DOCUMENT NO.	SPECIFICATION	QTY RECD.	PURCHASE QTY
2	FeedThru Flange	UNMM103/07	See Relevant Doc	1	1
1	MPC Multi-Pin Circular, Weldable single ended (6 Pin)	-	Kurt J. Lesker Model No. IFTRG067011	1	1


Parts List

THIS DRAWING IS OF A CONFIDENTIAL NATURE AND IS THE PROPERTY OF UNIVERSITY OF NEW MEXICO. REPRODUCTION, DISTRIBUTION, OR DISSEMINATION IN ANY MANNER, NOW OR IN THE FUTURE, FOR ANY PURPOSE INVOLVING DISSEMINATION IS STRICTLY PROHIBITED WITHOUT PERMISSION OF U.N.M.

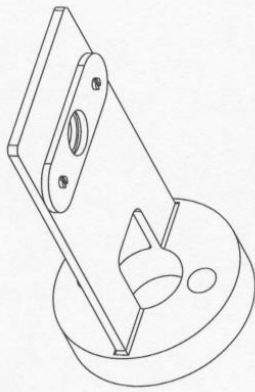
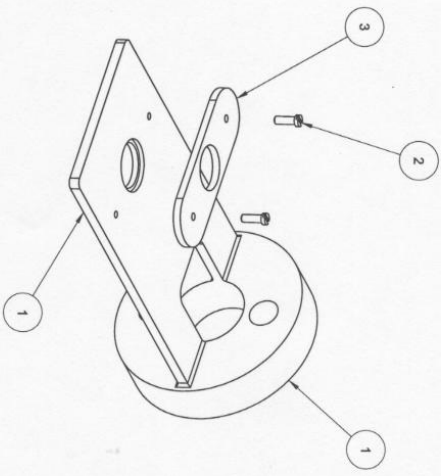


- NOTE:
1. WELDING BEAD SHOULD NOT PROTRUDE BEYOND THIS SURFACE.
 2. APPLY ULTRA HIGH VACUUM EPOXY (LOCTITE ????) AFTER WELDING.

REV.	CHANGE DESCRIPTION	CHKD.	APPD.	DATE
A	Original			06/07/07

		UNIVERSITY OF NEW MEXICO Mechanical Engineering Department 1 MSC01 1150, Albuquerque, NM 87131	
TITLE FeedThru Assy			
DESIGNED BY	CHKD BY	APPROVED BY	DATE
KHAWAR ABBAS			06/07/07
1/2	6	7	8
FORMA	SHEET	FILE NAME	
A3	2/2	Connector Assy.dwg	

THIS PRINT IS OF A CONFIDENTIAL NATURE AND IS THE PROPERTY OF UNIVERSITY OF NEW MEXICO. REPRODUCTION, IN WHOLE OR IN PART, IS PROHIBITED WITHOUT THE WRITTEN PERMISSION OF U.N.M.



ITEM	NAME	SPECIFICATION	DOCUMENT NO.	QTY	RECD	PURCHASE QTY
3	POSITIONING PLATE	See Relevant Doc	UNM109107	1		1
2	WATCH SCREW	TBD		2		10
1	HOLDER PLATE	See Relevant Doc	UNM109107	1		1

Parts List

UNIVERSITY OF NEW MEXICO
 Mechanical Engineering Department
 1 MSC01 1150, Albuquerque, NM 87131

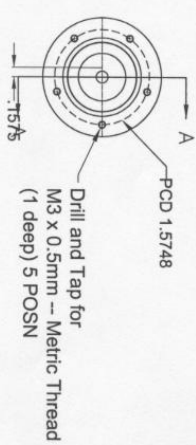
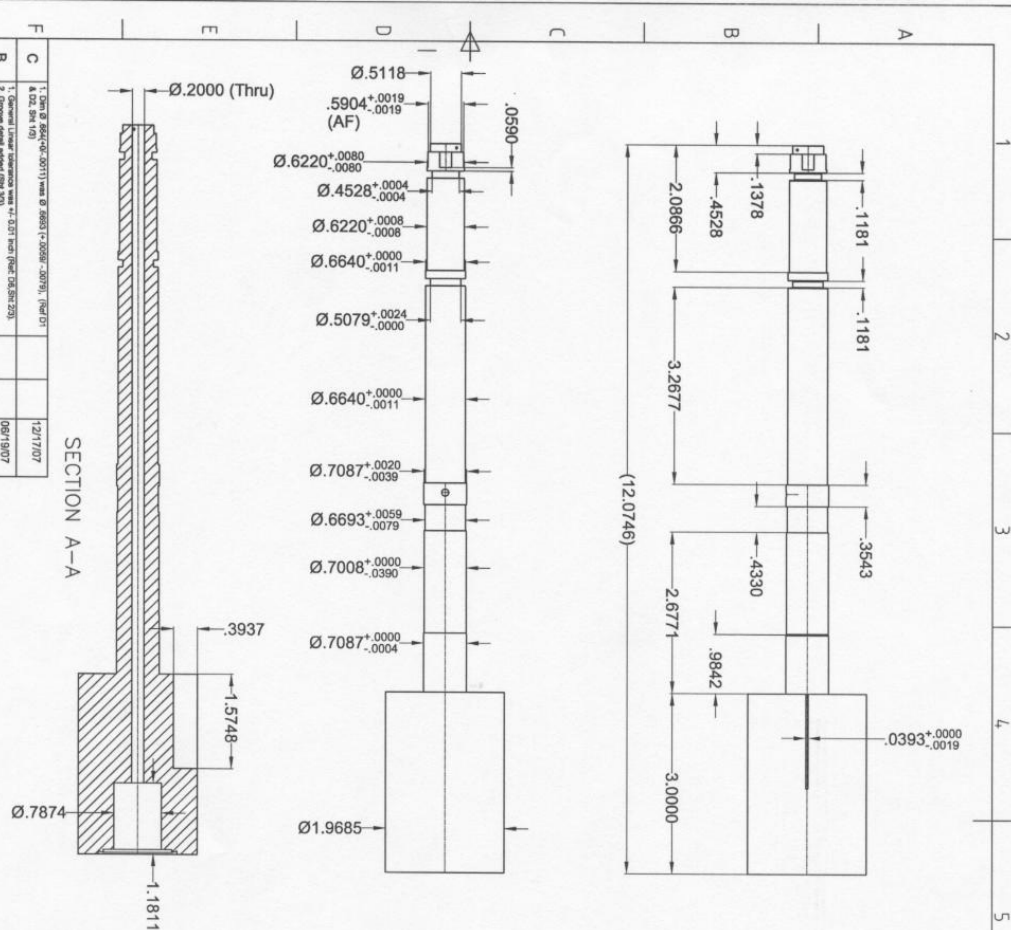
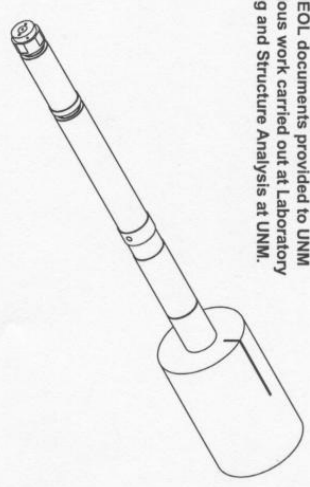
TITLE
Holder Plate Assy

DESIGNED BY KHAWAR ABBAS
 CHECKED BY
 APPROVED BY
 DWG NO. UNM\09\07
 SHEET 1/1
 FILE NAME Holder Assy.dwg

REV	CHANGE DESCRIPTION	CHG. APPD.	DATE
1	Original		06/07/07
2			
3			

THIS PRINT IS OF A COMPUTATIONAL NATURE AND IS THE PROPERTY OF UNIVERSITY OF NEW MEXICO. REPRODUCTION, TRANSMISSION, OR DISTRIBUTION IN ANY MANNER NOT PERMITTED BY UNIVERSITY OF NEW MEXICO. REPRODUCTION OF THIS PRINT IS PROHIBITED WITHOUT THE WRITTEN PERMISSION OF U.N.M.

This design has been adapted from the original JEOL documents provided to UNM and previous work carried out at Laboratory of Imaging and Structure Analysis at UNM.



REV.	CHANGE DESCRIPTION	CHKD.	APPD.	DATE
A	Original			06/07/07
B	1. General Linear dimension was 4.5277 inch (Rev. 106.SR.208)			12/17/07
C	4.02 inch (1/2)			06/19/07
D	2. Drive end added (Rev. 107)			
E	3. Changes added to Dim. 4.5277 (Rev. 107, Rev. 108)			

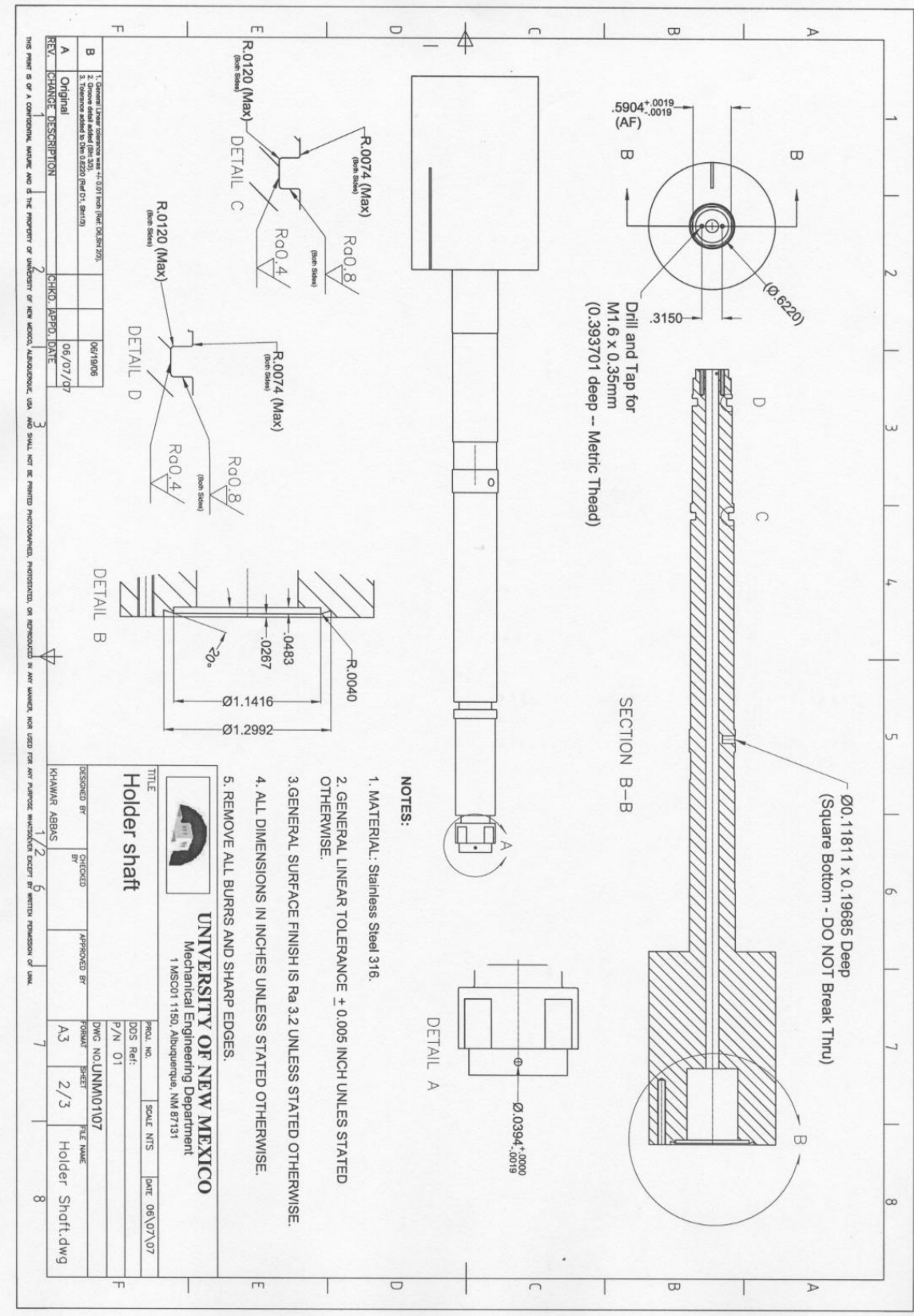
UNIVERSITY OF NEW MEXICO
 Mechanical Engineering Department
 1 MSCOT 1150, Albuquerque, NM 87131

Holder Shaft

DESIGNED BY: KHAWAR ABBAS
 CHECKED BY: []
 APPROVED BY: []

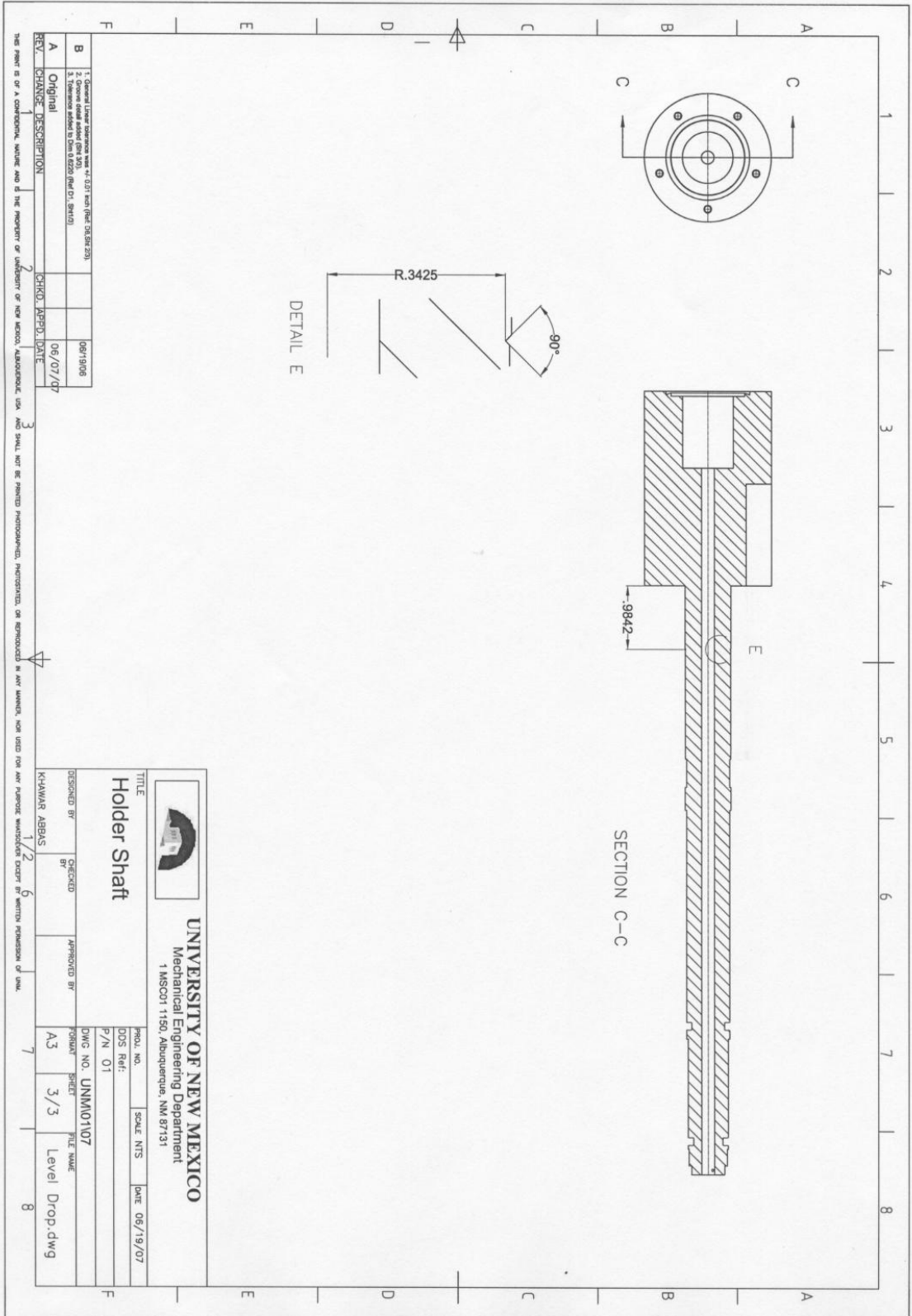
PROJ. NO.: DWG. NO. UNM0107
 DWS Ref: P/N 01
 SCALE: NTS
 DATE: 06/07/07
 SHEET: 1/3
 FILE NAME: Holder Shaft.dwg

THIS DRAWING IS THE PROPERTY OF UNIVERSITY OF NEW MEXICO, ALBUQUERQUE, USA AND SHALL NOT BE REPRODUCED, PHOTOGRAPHED, REPRODUCED, OR REPRODUCED IN ANY MANNER, FOR USE FOR ANY PURPOSE WITHOUT THE EXPRESS WRITTEN PERMISSION OF UNM.




REV.	CHANGE DESCRIPTION	CHKD.	APPR.	DATE
A	Original			06/19/06
B	1. General Linear Tolerance was ±.001 inch (not .005 inch). 2. General surface finish was Ra 3.2. 3. Dimension added to Dia. 0.6220 (not 0.6217).			06/07/07

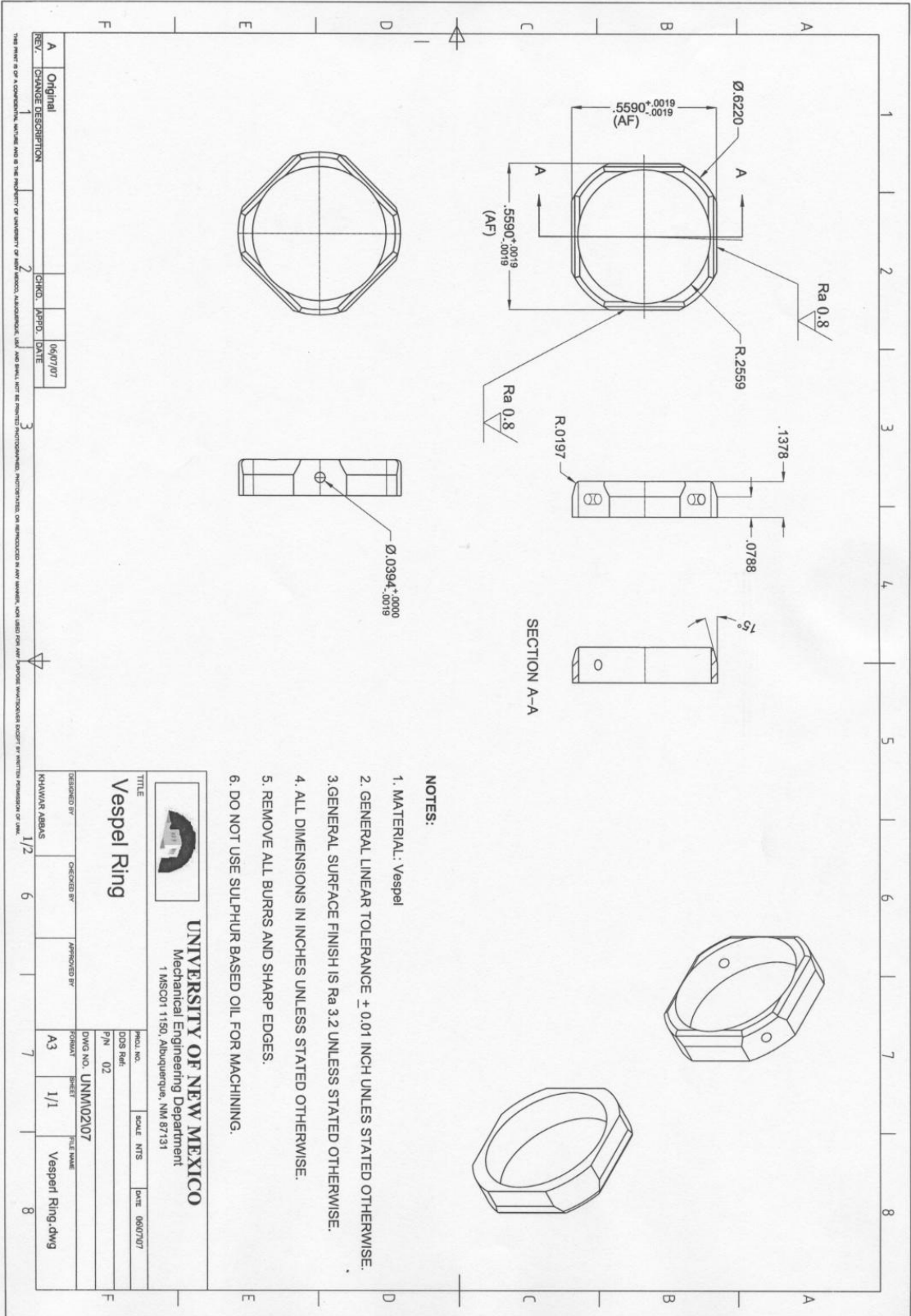
DESIGNED BY KHANUAR ABBAS	CHECKED BY	APPROVED BY	DWG NO. UNNM0107	FILE NAME Holder Shaft.dwg
TITLE Holder shaft	SCALE NTS	DATE 06/07/07	UNIVERSITY OF NEW MEXICO Mechanical Engineering Department 1 MSCOT 1150, Albuquerque, NM 87131	



REV.	CHANGE DESCRIPTION	CHKD.	APPD.	DATE
A	Original			06/19/06
B	General Linear Dimension was 4.007 from (Part Dwg 88223)			
C	General Linear Dimension was 1.9842 from (Part Dwg 88223)			
D	Tolerance added to Dim 1.9842 (Part Dwg 88223)			

THIS DRAWING IS THE PROPERTY OF UNIVERSITY OF NEW MEXICO. UNAUTHORIZED USE AND SHALL NOT BE REPRODUCED, PHOTOGRAPHED, REPRODUCED, OR REPRODUCED IN ANY MANNER, FOR USE FOR ANY PURPOSE WHATSOEVER EXCEPT BY WRITTEN PERMISSION OF UNM.

		UNIVERSITY OF NEW MEXICO Mechanical Engineering Department 1 MSC01 1150, Albuquerque, NM 87131	
TITLE Holder Shaft			
DESIGNED BY	CHECKED BY	APPROVED BY	
KHAWAR ABBAS			
PROJ. NO.	SCALE	NTS	DATE
01			06/19/07
P/N			
01			
DWG NO.	UNM01107	TITLE NAME	
FORMA	SHEET		
A3	3/3	Level Drop.dwg	



NOTES:

1. MATERIAL: Vespel
2. GENERAL LINEAR TOLERANCE ± 0.01 INCH UNLESS STATED OTHERWISE.
3. GENERAL SURFACE FINISH IS Ra 3.2 UNLESS STATED OTHERWISE.
4. ALL DIMENSIONS IN INCHES UNLESS STATED OTHERWISE.
5. REMOVE ALL BURRS AND SHARP EDGES.
6. DO NOT USE SULPHUR BASED OIL FOR MACHINING.



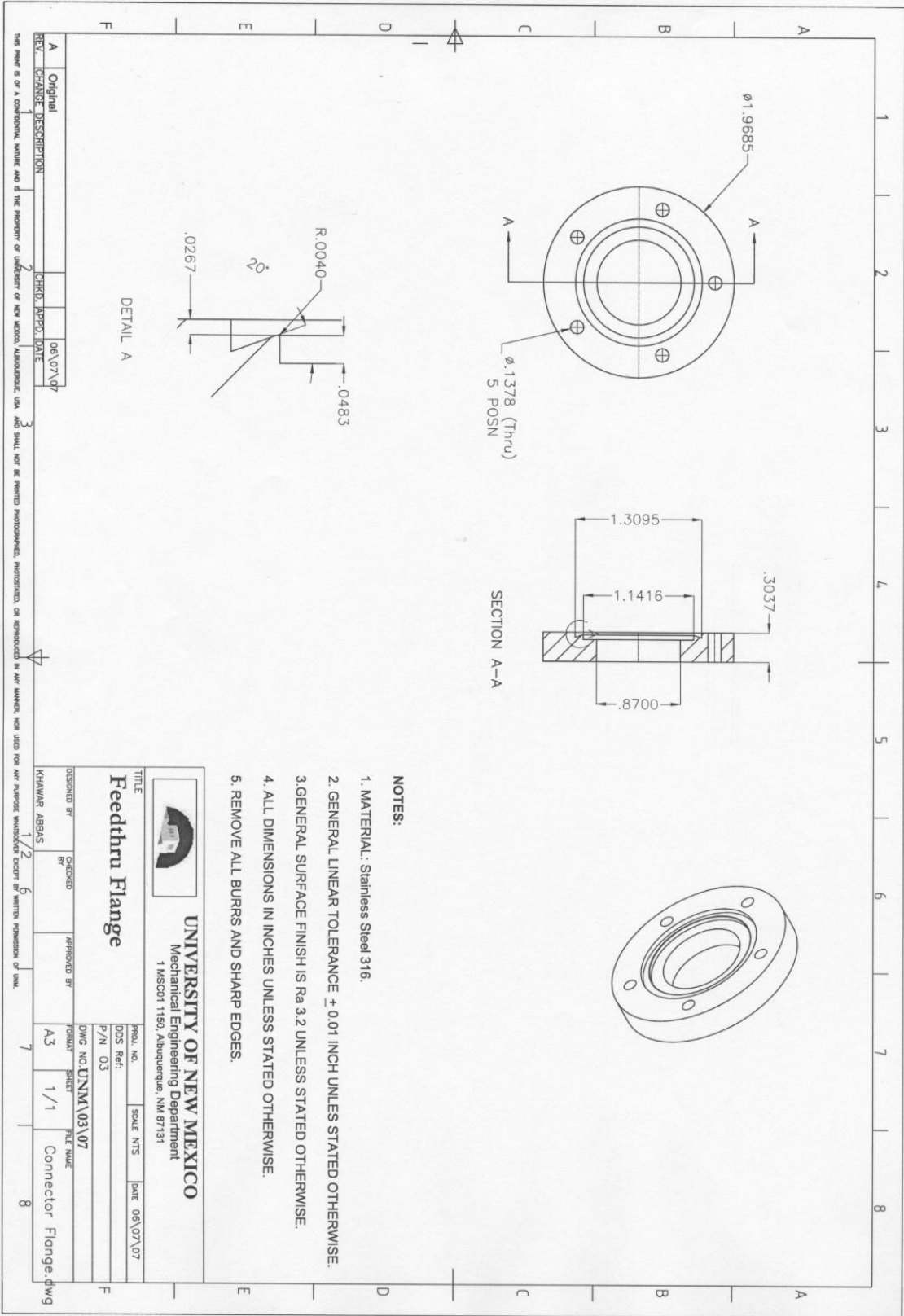
UNIVERSITY OF NEW MEXICO
 Mechanical Engineering Department
 1 MSC01 1150, Albuquerque, NM 87131

TITLE
Vespel Ring

DESIGNED BY KHAJUR ABRAIS	CHECKED BY	APPROVED BY	PERIOD NO. D08 Fall	SCALE NTS	DATE 06/07/07
1/2	6	7	P/N 02		
			DWG NO. UNMM02107		
			DESIGN A3	SHEET 1/1	FILE NAME Vespel Ring.dwg
					8


REV. A	CHANGE DESCRIPTION	CHG. DATE
		06/07/07

THIS DRAWING IS THE PROPERTY OF UNIVERSITY OF NEW MEXICO. UNAUTHORIZED USE AND REPRODUCTION IS PROHIBITED. ANY REPRODUCTION WITHOUT WRITTEN PERMISSION IS PROHIBITED.



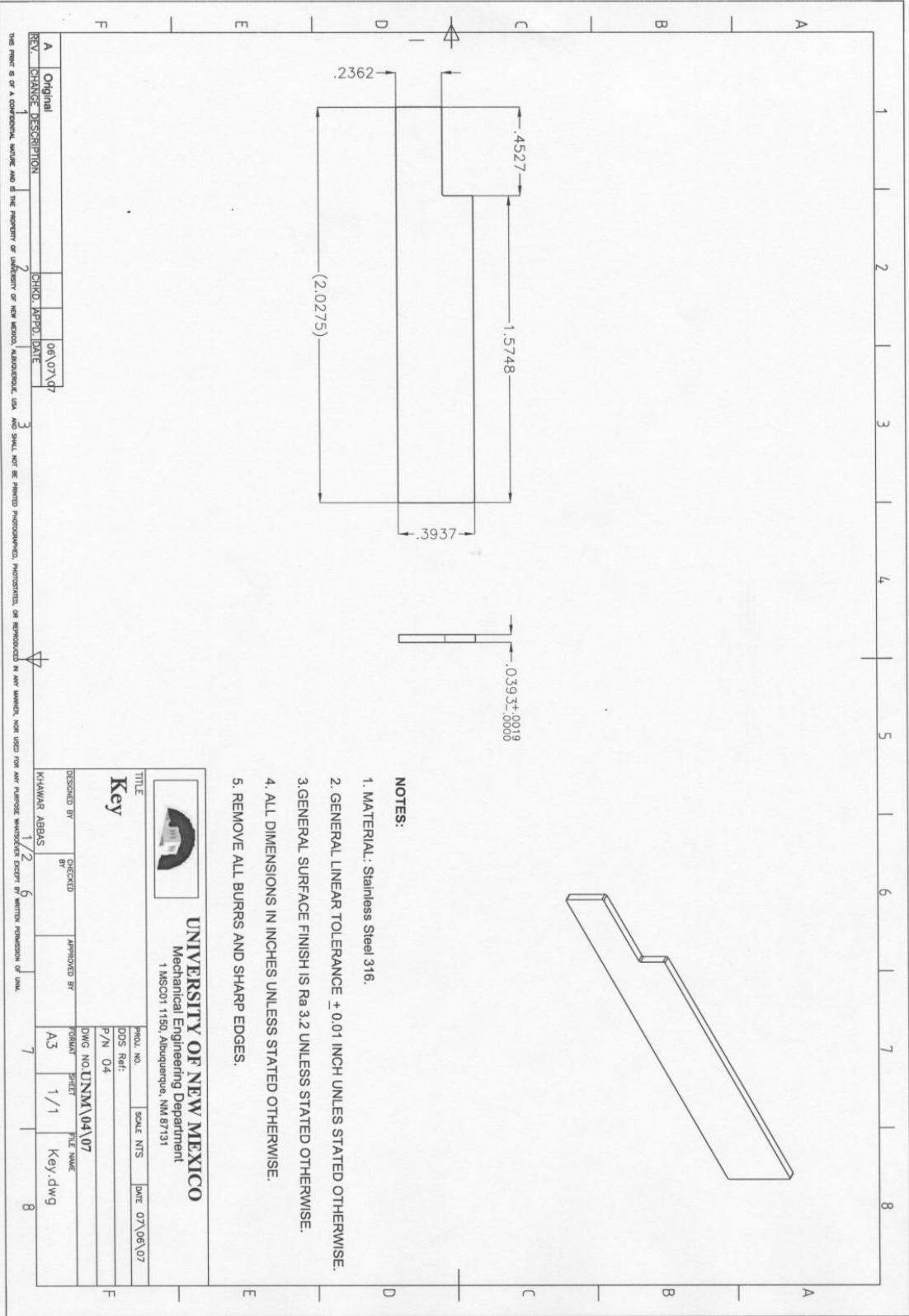
NOTES:

1. MATERIAL: Stainless Steel 316.
2. GENERAL LINEAR TOLERANCE ± 0.01 INCH UNLESS STATED OTHERWISE.
3. GENERAL SURFACE FINISH IS Ra 3.2 UNLESS STATED OTHERWISE.
4. ALL DIMENSIONS IN INCHES UNLESS STATED OTHERWISE.
5. REMOVE ALL BURRS AND SHARP EDGES.

 <p>UNIVERSITY OF NEW MEXICO Mechanical Engineering Department 1 MSC01 1150, Albuquerque, NM 87131</p>		<p>TITLE</p> <p>Feedthru Flange</p>
DESIGNED BY	CHECKED BY	APPROVED BY
KHAMAR ABBAS		
PROJ. NO.	SCALE	DATE
005 Ref:	NTS	06/07/07
P/N 03		
DWG NO. UNM\03\07		
FORMAT	SHEET	FILE NAME
A3	1/1	Connector Flange.dwg


REV.	CHANGE DESCRIPTION	CHECKED	APPROVED	DATE
A	Original			06/07/07

THIS DRAWING IS THE PROPERTY OF UNIVERSITY OF NEW MEXICO, ALBUQUERQUE, USA AND SHALL NOT BE REPRODUCED, PHOTOGRAPHED, REPRODUCED, OR REPRODUCED IN ANY MANNER, NOR USED FOR ANY PURPOSE WITHOUT THE WRITTEN PERMISSION OF UNM.



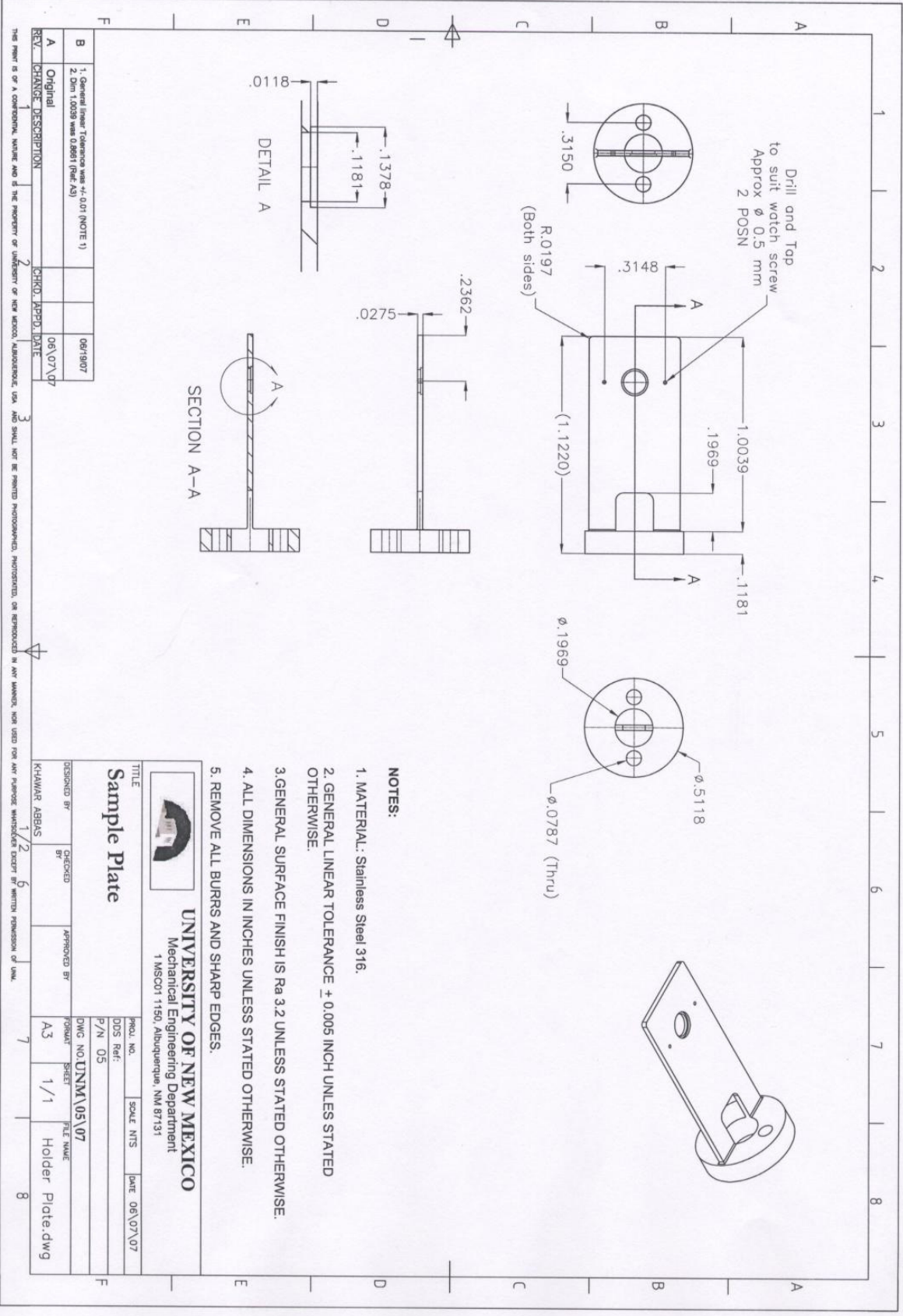
NOTES:

1. MATERIAL: Stainless Steel 316.
2. GENERAL LINEAR TOLERANCE ± 0.01 INCH UNLESS STATED OTHERWISE.
3. GENERAL SURFACE FINISH IS Ra 3.2 UNLESS STATED OTHERWISE.
4. ALL DIMENSIONS IN INCHES UNLESS STATED OTHERWISE.
5. REMOVE ALL BURRS AND SHARP EDGES.

 <p>UNIVERSITY OF NEW MEXICO Mechanical Engineering Department 1 MSC04 1150, Albuquerque, NM 87131</p>		
TITLE	Key	
DESIGNED BY	KHAWAR ABYAS	
CHECKED BY		
APPROVED BY		
PROJ. NO.	SCALE NTS	DATE 07/06/07
DDS Ref:	P/N 04	
DWG NO. UNM\04\07	FORMA SHEET	FILE NAME
A3	1/1	Key.dwg


REV.	DESCRIPTION	CHKD.	APPR.	DATE
A	Original			06/07/07
1				
2				
3				
4				
5				
6				
7				
8				

THIS DRAWING IS OF A CONCEPTUAL NATURE AND IS THE PROPERTY OF UNIVERSITY OF NEW MEXICO. REPRODUCTION, IN WHOLE OR IN PART, FOR ANY PURPOSE WITHOUT THE WRITTEN PERMISSION OF UNM.



NOTES:

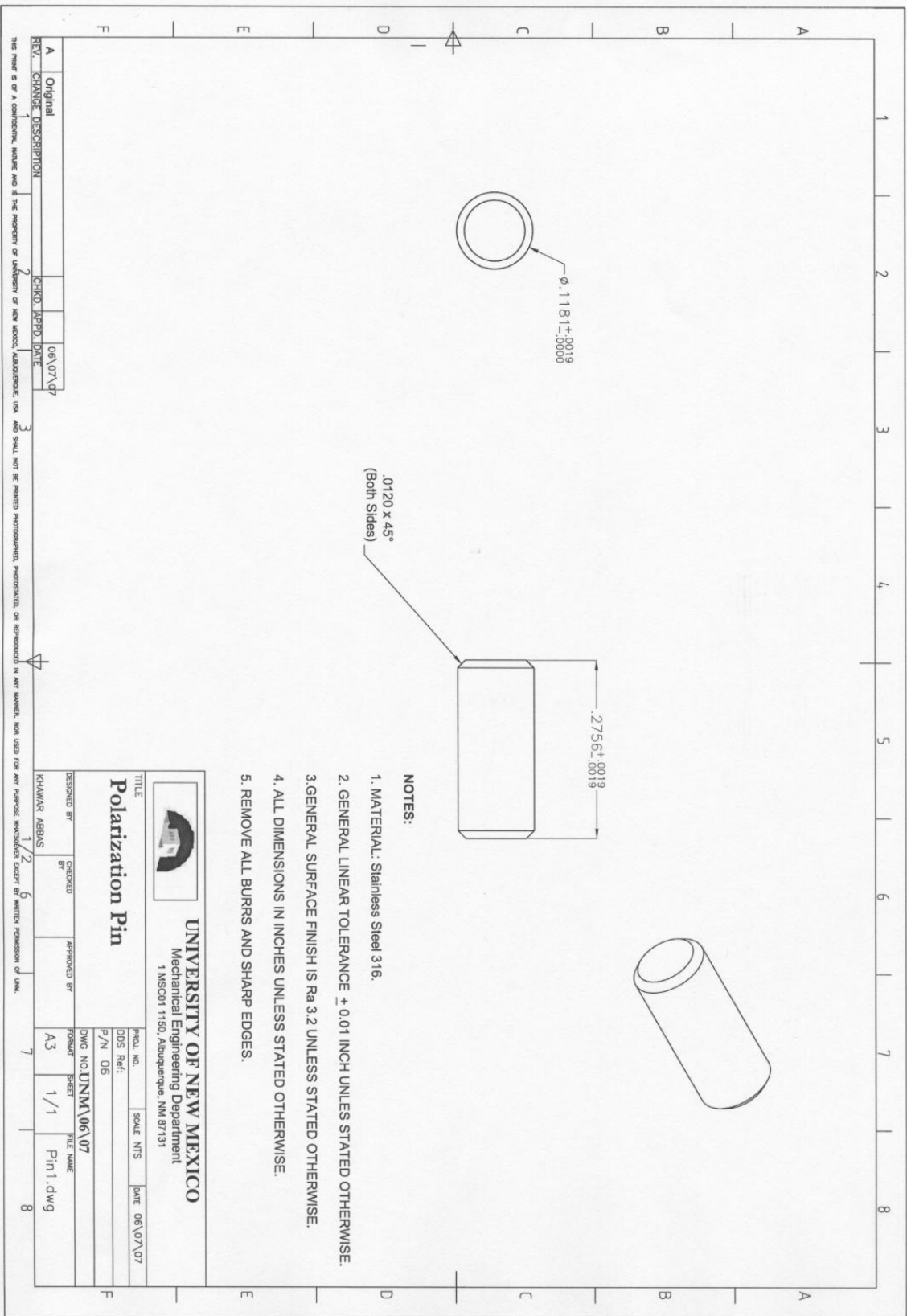
1. MATERIAL: Stainless Steel 316.
2. GENERAL LINEAR TOLERANCE \pm 0.005 INCH UNLESS STATED OTHERWISE.
3. GENERAL SURFACE FINISH IS Ra 3.2 UNLESS STATED OTHERWISE.
4. ALL DIMENSIONS IN INCHES UNLESS STATED OTHERWISE.
5. REMOVE ALL BURRS AND SHARP EDGES.


UNIVERSITY OF NEW MEXICO
 Mechanical Engineering Department
 1 MSC01 1150, Albuquerque, NM 87131

TITLE		PROJ. NO.		SCALE		DATE	
Sample Plate		DOS Ref:				06/07/07	
DESIGNED BY		P/N		DWG NO.		SHEET	
KHAMAR ABBAS		05		UNNM\05\07		1/1	
CHECKED BY		APPROVED BY		DATE		FILE NAME	
				06/07/07		Holder Plate.dwg	
1/2		6		7		8	

REV.	CHANGE DESCRIPTION	CHKD.	APPR.	DATE
A	Original			06/19/07
B	1. General linear Tolerance was \pm 0.01 (NOTE 1) 2. Dim 1.0039 was 0.8981 (Ref. A3)			06/19/07

THIS PRINT IS BY THE PROPERTY OF UNIVERSITY OF NEW MEXICO. REPRODUCTION, PHOTOCOPIED, OR REPRODUCED IN ANY MANNER, MAY BE USED FOR ANY PURPOSE WITHOUT PERMISSION OF UMW.




.0120 x 45°
(Both Sides)

$\phi.1181^{+0.0019}$

$.2756^{+0.0019}$

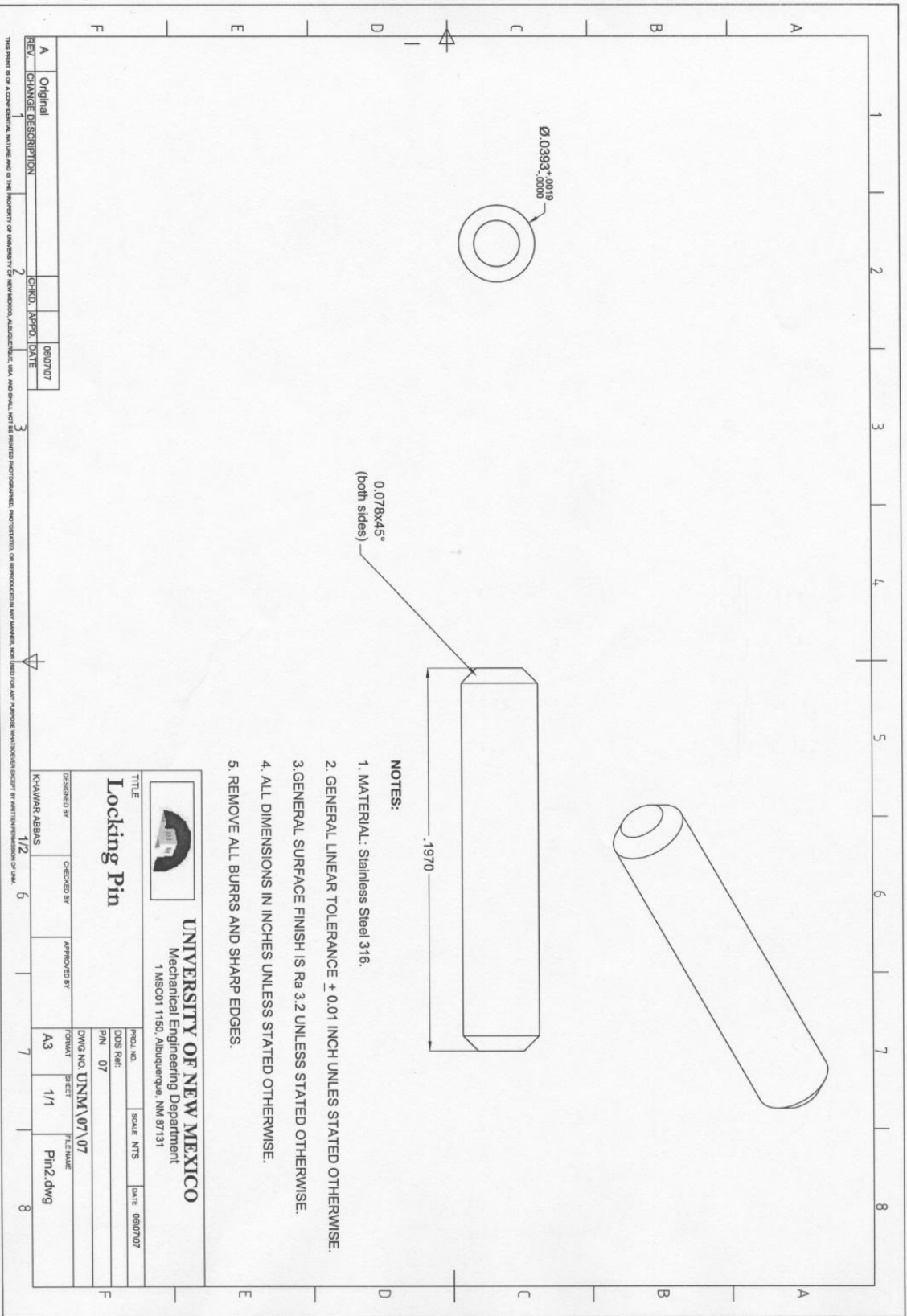
NOTES:

1. MATERIAL: Stainless Steel 316.
2. GENERAL LINEAR TOLERANCE ± 0.01 INCH UNLESS STATED OTHERWISE.
3. GENERAL SURFACE FINISH IS Ra 3.2 UNLESS STATED OTHERWISE.
4. ALL DIMENSIONS IN INCHES UNLESS STATED OTHERWISE.
5. REMOVE ALL BURRS AND SHARP EDGES.

 <p>UNIVERSITY OF NEW MEXICO Mechanical Engineering Department 1 MSC01 1150, Albuquerque, NM 87131</p>		DESIGNED BY	CHECKED BY	APPROVED BY	PROJ. NO.	SCALE	NTS	DATE
		KHAMAR ABBAS				06\07\07		
<p>TITLE</p> <p>Polarization Pin</p>		DWG. NO.	SHEET	FILE NAME				
		UNM\06\07	1/1	Pin1.dwg				
		P/N	06					
		FORMAT						

REV.	CHANGE DESCRIPTION	CHKD.	APPD.	DATE
1	Original			06\07\07
2				
3				

THIS DRAWING IS THE PROPERTY OF UNIVERSITY OF NEW MEXICO. MANUFACTURE IN USA AND SHALL NOT BE REPRODUCED, PHOTOGRAPHED, REPRODUCED, OR REPRODUCED IN ANY MANNER, NOR USED FOR ANY PURPOSE WHATSOEVER EXCEPT BY WRITTEN PERMISSION OF UNM.



0.076x45°
(both sides)

0.1970

Ø.0393 ± .0019
.0000

NOTES:

1. MATERIAL: Stainless Steel 316.
2. GENERAL LINEAR TOLERANCE ± 0.01 INCH UNLESS STATED OTHERWISE.
3. GENERAL SURFACE FINISH IS Ra 3.2 UNLESS STATED OTHERWISE.
4. ALL DIMENSIONS IN INCHES UNLESS STATED OTHERWISE.
5. REMOVE ALL BURRS AND SHARP EDGES.



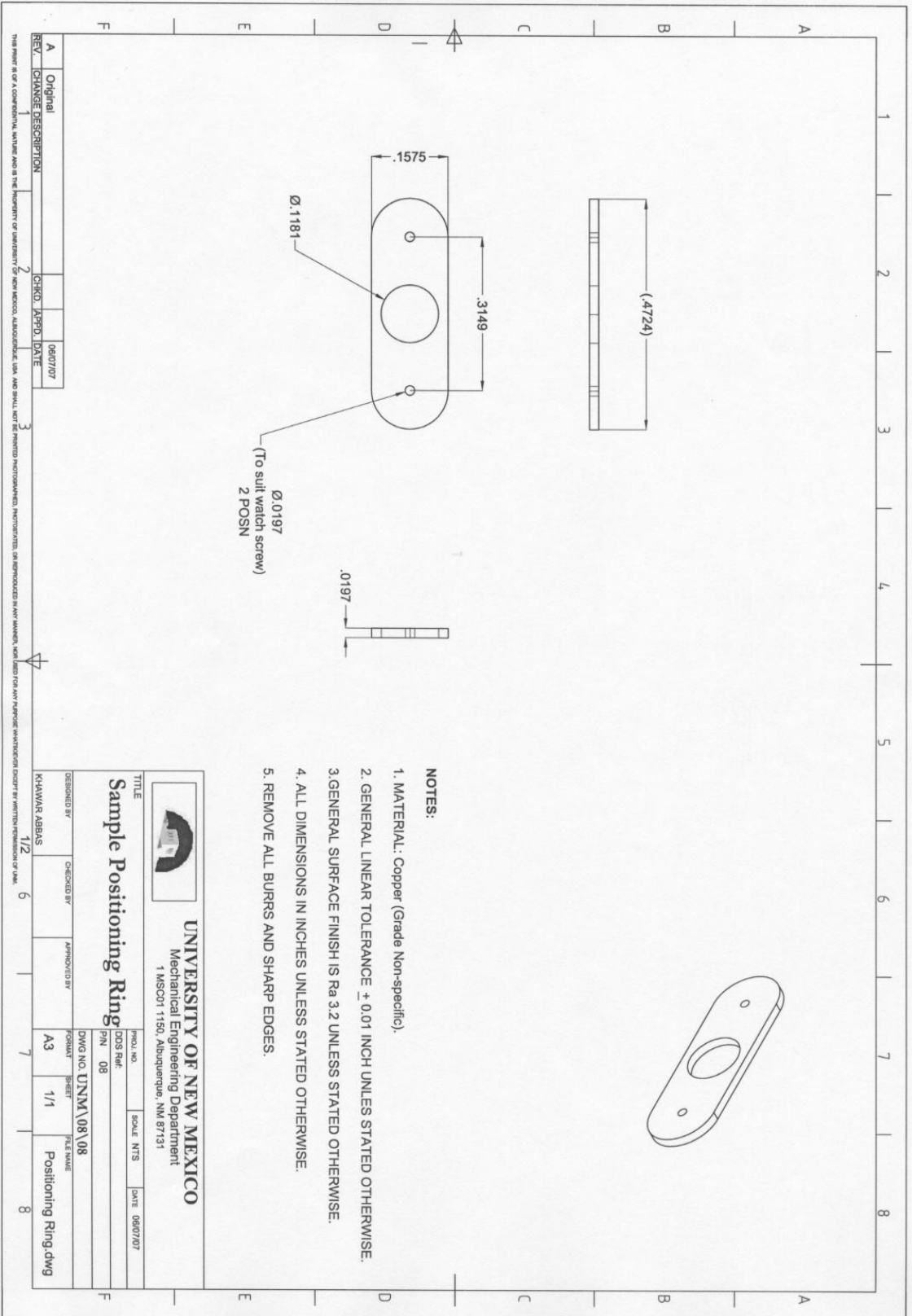
UNIVERSITY OF NEW MEXICO
Mechanical Engineering Department
1 MSC01 1150, Albuquerque, NM 87131

Locking Pin

DESIGNED BY KHAJAR ABRAH	CHECKED BY	APPROVED BY	PROJ. NO.	SCALE	NTS	DATE	08/07/07
1/2	6	7	CDIS RMR	PIN	07	DWG NO	UNM\07\07
1/2	6	7	A3	SHEET	1/1	FILE NAME	Pin2.dwg
8							

REV	CHANGE DESCRIPTION	CHKD.	APPR.	DATE
A	Original			08/07/07


THIS DRAWING IS A CONFIDENTIAL MATTER AND IS THE PROPERTY OF UNIVERSITY OF NEW MEXICO, ALBUQUERQUE, N.M. AND SHALL NOT BE REPRODUCED, PHOTOCOPIED, REPRODUCED IN ANY MANNER, NOR USED FOR ANY PURPOSES WHATSOEVER WITHOUT THE WRITTEN PERMISSION OF UNM.



Ø.1181
 (To suit watch screw)
 Ø.0197
 2 POSN

NOTES:

1. MATERIAL: Copper (Grade Non-specific).
2. GENERAL LINEAR TOLERANCE ± 0.01 INCH UNLESS STATED OTHERWISE.
3. GENERAL SURFACE FINISH IS Ra 3.2 UNLESS STATED OTHERWISE.
4. ALL DIMENSIONS IN INCHES UNLESS STATED OTHERWISE.
5. REMOVE ALL BURRS AND SHARP EDGES.

		UNIVERSITY OF NEW MEXICO Mechanical Engineering Department 1 MSC01 1150, Albuquerque, NM 87131	
TITLE Sample Positioning Ring			
DESIGNED BY	CHECKED BY	APPROVED BY	
KHAWAR ABBAS			
PROJ. NO.	SCALE	NTS	DATE
08/07/07			08/07/07
DWG NO.	FILE NAME		
UNM\08\08	Positioning Ring.dwg		
PIN	SHEET	DATE	
08	1/1		

REV.	CHANGE DESCRIPTION	CHECKED	APPROVED	DATE
A	Original			08/07/07

THIS DRAWING IS A CONFIDENTIAL, PRIVATE AND IS THE PROPERTY OF UNIVERSITY OF NEW MEXICO. ALIENATION, USA AND SHALL NOT BE PRINTED, REPRODUCED, PHOTOGRAPHED, REPRODUCED IN ANY MANNER, NOR USED FOR ANY PURPOSE WHATSOEVER EXCEPT BY WRITTEN PERMISSION OF UNM.